DOCTORAL THESIS

Electrical Phenomena Caused by Hypervelocity Impacts of Space Debris and Their Effects on Spacecraft

Author:
Yuki MANDO

Supervisor:
Associate Professor
Koji TANAKA

A thesis submitted in fulfillment of the requirements for the degree of Doctor of Philosophy

in the

The Graduate University for Advanced Studies, SOKENDAI
Department of Space and Astronautical Science, School of Physical Sciences

March 5, 2020

Abstract

The Graduate University for Advanced Studies, SOKENDAI
Department of Space and Astronautical Science, School of Physical Sciences

Doctor of Philosophy

Electrical Phenomena Caused by Hypervelocity Impacts of Space Debris and Their Effects on Spacecraft

by Yuki MANDO

Space debris (referred to as debris) moving at an extremely high speed can collide with spacecraft. In this case, electrical phenomena, such as plasma generation, radiofrequency (RF) emission, and potential variation of the impacted target, can occur in addition to serious mechanical phenomena such as spacecraft destruction and secondary debris generation. Significant research effort has been focused on the mechanical phenomena to develop the shields against micrometeoroids or debris i mpacts. However, the research on electrical phenomena caused by hypervelocity impact has gained lesser attention than that on mechanical phenomena.

Herein, the plasma density and propagation of impact plasma were investigated to understand and estimate the risk of electric discharge on the spacecraft. Several plasma diagnosis methods exist; in particular, plasma probe methods can locally examine the plasma density by using multiple probes. Herein, the double probe method with a fixed bias voltage, which is one of the plasma probe methods, was used for this plasma measurements.

The spectroscopic method is a plasma temperature measurement method. Using this method, attempts have been made to measure the plasma temperature from the intensity ratio at three emission wavelengths from the luminous vapor cloud. However, if the emission line spectra derived from projectile and target materials are superposed on the wavelengths, the temperature cannot be measured. Moreover, the plasma density was calculated considering the ion mass of either the target or the projectile material, when impacts between the different target and projectile materials.

Hence, the study proposes a method to accurately calculate the plasma temperature using a spectroscopy via a streak camera. The streak camera spectroscopy can measure the time-resolved spectra in the wavelength range of 547 nm - 872 nm. The advantages of this method are that (1) the temperature can be calculated using the time-resolved spectra with a wide wavelength band and a large number of sampling points, and (2) the wavelength of the profiled emission line spectrum can be excluded from the temperature calculation.

Furthermore, the composition of ions, comprising impact plasma, has not been specified in the case of collision between different materials. By comparing the temporal change of emission lines derived from the target and projectile materials, it can be concluded that the impact plasma, comprising the target and projectile materials, is simultaneously generated.

Therefore, a method can be proposed to accurately obtain the plasma temperature and density. The impact of spacecraft on solar cells and power harness systems can be accurately estimated by obtaining the precise parameters of the impact plasma.

Impact plasma induced by the hypervelocity impacts on solar cells can trigger electric discharge, which can cause a grounding fault in the spacecraft. Even though the power harness system behind the solar array paddle (SAP) and at the SAP boom is usually exposed to space, the electrical effects on the power harness system attributed to the hypervelocity impacts have received little attention. Previous studies have confirmed that grounding faults can occur because of the permanent sustained discharge (PSD) in debris collisions with a diameter of 0.2 mm or more. However, the frequency of these debris impacts on the power harness system of artificial satellites in a low Earth orbit simulated by a debris environment model is larger than the frequency of grounding faults in these satellites. Therefore, a deviation from the actual phenomenon is observed. Moreover, the effect of impact plasma on the power harness system is still unknown. Therefore, the PSD of the power harness system induced by the hypervelocity impacts is investigated herein.

In previous studies, the satellite load circuit was not simulated; thus, electric discharge can easily occur. Furthermore, multiple projectiles can simultaneously impact the power harness system because of the limitation of the impact test apparatus. When multiple projectiles impact, the impact plasma can interfere each other if the collision point is close. In this case, hypervelocity impact experiments must be conducted with single-particle impact to accurately evaluate the presence or absence of PSD occurrence.

Herein, experiments were conducted to re-verify the presence or absence of PSD occurrence by simulating a power harness system under conditions similar to those in the actual environment. In particular, the attention was focused on the circuit configuration and the multiple-particle impacts that can affect the occurrence of PSD. Two configurations cases with and without a load circuit were prepared and compared. Moreover, the array of double probes was set inside the measurement chamber to clarify the relationship between impact plasma and PSD.

Results indicated that the impact plasma can trigger the primary discharge and even a single-particle impact can easily result in PSD occurrence in the conventional configuration without a load circuit. The surface of the power harness system melted and carbonized near the impact points. However, a single impact does not result in PSD occurrence in the configuration with a load circuit with a resistance and a capacitance. Further, PSD never occurred even in the case of multiple-particle impacts. Therefore, the presence of a load circuit heavily affected the PSD occurrence by comparing previous studies. This result indicates that previous studies may have overestimated potential risks.

Regarding the microwave emission, it was confirmed that an RF signal with a wide frequency range of several kHz to several tens of GHz is emitted from hypervelocity impacts. RF emission arises from hypervelocity impacts on both metallic and non-metallic targets. However, the complete mechanism of microwave emission has not been investigated yet, although there are some

suggestions that the microwave emission is caused by the impact plasma or by material destruction. To elucidate the mechanism of microwave emission, experiments were conducted by simultaneously measuring microwave emissions, impact plasma, and flash phenomena.

The microwave emission phenomenon can be clarified by simultaneously measuring the flash and impact plasma phenomena. The experimental results indicated that the time scale between impact plasma including light emission during dozens of microseconds and microwave phenomena during several milliseconds are significantly different.

Frequency characteristics investigation of the microwave emission was possible for the first time using the microwave measurement. In this measurement, two types of broadband log-periodic antennas were used. It was found that microwaves radiate in a wide band, but microwave emissions are shielded by high-dense impact plasma generated immediately after the impact. This suggests that the source of microwave emission is generated near the crater site inside the plume of the impact plasma.

Furthermore, to investigate the mechanism of microwave emission, hypervelocity experiments using various types of aluminum materials were conducted. The experimental results showed that the harder the target materials corresponded to a higher intensity of microwave emission. Using numerical simulations, it was found that the target hardness has a correlation with the elastic wave repeatedly propagating in the target material, and it is considered that the intermittent microwave radiation is related to the propagation of the elastic wave.

Conclusively, the electrical phenomena of impact plasma and microwave emissions induced by hypervelocity impacts were investigated. The accurate determination of the impact plasma parameters will enable the accurate estimation of discharge risk caused by hypervelocity impacts on solar cells and power harness systems mounted on the spacecraft. The proposed method to obtain plasma parameters can also contribute to the reliability of the satellite power system because of debris impacts by re-examining hypervelocity impact experiments on power harness systems. The microwave emission phenomenon is expected to be applied to estimate the scale, position, and frequency of debris collisions in the future. This work has contributed to both the basic and applied space engineering knowledge regarding electrical phenomena generated by hypervelocity impacts.

Acknowledgements

During my Ph.D. program at SOKENDAI, there have been countless people who gave me support. First, to my supervisor, Assoc. Prof. Koji Tanaka, thank you for supporting me for 4 years and half since you accepted my offer of the JAXA internship when I was a master student at the first grade. Since I belonged at your laboratory, he taught me so many things about research activities including experiments about wireless power transmissionn, and interaction between intensity microwave and ionosphere plasma, and outreach activities to achieve solar power satellite. Thanks to him, I could learn how to going on research and experiments, and how important knowledge of our research activities share with people who are not involved with our research though our outreach activities. I am grateful for all of the opportunities you have given me.

Second, to my Ph.D. dissertation committee members, Prof. Susumu Sasaki, Assoc.Prof. Takahide Mizuno, Assis. Prof. Kenichiro Maki, Dr. Masumi Higashide, and Prof. Masatake Kawada, thank you for your precious feedback on my defense and my dissertation. I would like to thank to my advisor, Prof. Ichiro Shiota, who is an emeritus professor at Kogakuin University, Dr. Eriko Soma who is a researcher at ISAS/JAXA. They gave me precious technical advices at weekly meetings of our laboratory and experiments.

The experiments were selected and supported by the Space Plasma Laboratory, ISAS/JAXA. I thank Dr. Sunao Hasegawa who is in charge of the management of the experimental facilities installed at the two-light gas gun. He and other supporting staff operate the gun and the experimental devices safety and efficiently. I thank Mr. Amane and Mr. Hashimoto of Nippon Light Company gave me the different heat treated aluminum alloy samples. Moreover, I appreciate that Mr. Kitamoto and Dr. Joudoi of JAXA gave me the honeycomb panel.

Thank you for the all of the students and Assoc. Prof. Tanaka's secretary, Ms. Tomomi Ikeda in the laboratory. Especially, the students greatly help me to setup my experimental devices and the operations when my experiments had been conducted. Mr. Tatsuya Yamagami, Takaya Nakamura, Naoki Sekiya, Daichi Ota, Mudassir Raza, Soki Akutsu, and the former students are always amazing supporters.

My entire life of the Ph.D. program could not be accomplished without any financial support. To professors and staff of SOKENDAI, thank you for selecting me the granted-type special scholarship for department of space astronautical science for 3 years. I am also grateful to join the mission of the Epsilon Rocket No.3 and work at Uchinoura Space Center, Kagoshima for couple of weeks funded by my department when I was at the second grade. To JAXA, I would appreciate that I was hired as a research assistant and I involved with the cutting-edge technology and research in JAXA. Besides that, JAXA space education center had selected me as a JAXA dispatch student of the international student education board (ISEB) program twice. In ISEB program, I conducted the outreach activities to elementary/junior/high school students who commute to the local schools in Australia and Germany and delivered oral presentations at a technical session of the International Astronautical Congress

(IAC) which is the biggest conference related to space technology in the world. Throughout all of the opportunities of the ISEB program, I got a connection with students around the world who are eager to space technology or exploration as well as researchers and I motivated myself.

Finally, thank you to my parents and grandparents. They are supporting to pursue my dreams. I could not have done the Ph.D. program without their support.

Contents

List of Figures

List of Tables

List of Abbreviations

CCD	**C**harged-**C**coupled **D**evice
CFRP	**C**arbon **F**iber **R**ainforced **P**lastics
DHCP	**D**ynamic **H**ost **C**onfiguration **P**rotocol
EMI	Electro**m**agnetic **I**nterference
ESA	**E**uropean **S**pace **A**gency
FFT	**F**ast **F**ourier **T**ransform
FWHM	**F**ull **W**idth at **H**alf **M**aximum
GEO	**G**eostationary **E**arth **O**rbit
IADC	**I**nter-**A**gency Space **D**ebris **C**oordination Committee
IF	**I**ntermittent **F**requency
ISAS	**I**nstitute of **S**pace and **A**stronautical **S**cience
ISS	**I**nternational **S**pace **S**tation
JAXA	**J**apan **A**erospace **E**xploration **A**gency
LEO	**L**ow **E**arth **O**rbit
LGG	Two-stage **L**ight **G**as **G**un
LO	**L**ocal **F**requency
LP	**L**og-**p**eriodic
MASTER	**M**eteoroid **a**nd **S**pace debris **T**errestrial **E**nvironment **R**eference
MMOD	**M**icro**m**eteoroid and **O**rbital **D**ebris
NASA	**N**ational **A**eronautics and **S**pace **A**dministration
NIST	**N**ational **I**nstitute of **S**tandards and **T**echnology
MCP	**M**icro-**C**hannel **P**late
ODEM	**O**rbital **D**ebris **E**ngineering **M**odel
TURANDOT	**T**actical **U**tilitiy for **R**apid **AN**alysis of **D**ebris on **O**rbit **T**errestrial
PIN	**P**-**I**ntrinsic-**N** diode
PHS	**P**ersonal **H**andy-phone **S**ystem
PSD	**P**ermanent **S**ustained **D**ischarge
RF	**R**adio **F**requency
SAP	**S**olar **A**rray **P**addle
SAS	**S**olar **A**rray **S**imulator
SMA	**S**ub **M**iniature type **A**
SPS	**S**olar **P**ower **S**atellite
SSN	**S**pace **S**urveillance **N**etwork

Physical Constants

Boltzmann constant	$k = 1.380\,648\,52 \times 10^{-23}\,\mathrm{m^2 kg s^{-2} K^{-1}}$
Elementary charge	$e = 1.602\,176\,62 \times 10^{-19}\,\mathrm{C}$
Permittivity in vacuum	$\epsilon_0 = 8.854\,187\,82 \times 10^{-12}\,\mathrm{m^{-3} kg^{-1} s^4 A^2}$
Planck constant	$h = 6.626 \times 10^{-34}\,\mathrm{Js}$
Mass of electron	$m_e = 9.109\,383\,56 \times 10^{-31}\,\mathrm{kg}$
Speed of light	$c_0 = 2.997\,924\,58 \times 10^{8}\,\mathrm{m\,s^{-1}}$

List of Symbols

C	capacitance	F
C_t	sound velocity of the target material	km/s
d	diameter of projectile	cm
D	crater depth	mm
f_{th}	Cutoff frequency	Hz
H	Brinell hardness	
I_p	plasma current	A
i_p	ionization energy of the projectile	eV
i_t	ionization energy of the target	eV
λ	wavelength of light	m
$\overline{m_i}$	mean ion mass	kg
m_t	ion mass of target material	kg
m_p	ion mass of projectile material	kg
M_t	mass of crater of the target	g
M_p	mass of projectile	g
N_e	plasma density	cm^{-3}
R	resistance	Ω
S	area of plasma probes	m^2
T	Blackbody temperature	K
T_e	plasma temperature	K
V_{p-p}	peak-to-peak voltage	mV
V_{max}	maximum voltage	mV
V_{min}	minimum voltage	mV
V_n	impact velocity	km/s
α	ratio of weight	
β	ratio of ionization energy	
ρ_p	density of the projectile material	g/cm^3
ρ_t	density of the target material	g/cm^3

This dissertation is dedicated to space engineering regarding electrical phenomena generated by hypervelocity impacts…

Chapter 1

Introduction

1.1 Space Debris

Since human beings launched artificial satellites for the first time in the world in 1957, more than 5160 space missions have been done worldwide (Office, 2019). There are currently a lot of objects in orbits around the Earth. They are called space debris (referred as 'debris'). There are mainly four factors causing the sources of debris (Office, 2008).

Operational debris- Operational debris is composed of inactive payloads and objects released during satellite delivery or satellite operations. They indicate lens caps, separation and packing devices, spin-up mechanisms, empty propellant tanks, and intact rocket bodies, payload shrouds and a few objects thrown away or dropped during manned activities.

Fragmentation debris- Fragmentations generally result from either explosions or collisions. There are several explosive mechanisms: (1) the catastrophic failure of internal components such as batteries, (2) propellant-related explosion, (3) failure of pressurized tanks, and (4) intentional destruction.

Deterioration debris- Very small debris particles are created by the gradual disintegration of spacecraft surfaces as results of exposure to the space environment. This deterioration includes paint flaking, plastic and metal erosion. It has been hypothesized that paint flaking is caused by the erosion of organic binders in the paint due to exposure to atomic oxygen.

Solid rocket motor ejecta- Solid rocket motors typically are used to transfer objects from low Earth orbit (LEO), at an altitude of around 150 km to 600 km above the surface of the Earth, to geosynchronous orbit (GEO), at an altitude of about 36,000 km above the surface of Earth. They eject thousands of kilograms of aluminum oxide dust into the orbital environment. The ejected dust is very small, with characteristic sizes believed to be less than 0.01 cm. However, long-term exposure of payloads to such particles is likely to cause erosion of exterior surfaces, chemical contamination, and may degrade operations of vulnerable components such as optical windows and solar panels.

Debris decays naturally (Science Technology Policy, 1995). When debris reentry the atmosphere, the atmosphere drag shows them down, and causes them to burn up and fall into the Earth. The lifetime of debris depends on altitudes. At altitudes of 200 km to 400 km, debris reentry the atmosphere with a few months. But, the lifetime of debris at altitudes of 400 km to 900 km takes from years to hundreds of years. Moreover, the lifetime of debris in GEO has million years.

In addition, debris decays by helping high solar activity. When the solar activity heats the Earth's upper atmosphere, it will expand to higher altitudes. With the heating, the upper atmosphere density increases and debris decays. However, the cycle of solar activity occurs every 11 years, so it takes much time to decay population of debris. The decay of the natural process cannot offset the present rate of debris generation.

Currently, over 40,000 objects which are more than 5 cm in diameter (commonly referred to as large objects) are routinely detected, tracked, and cataloged by the U.S. Space Surveillance Network (SSN). Fig.1.1 shows the monthly number of objects in Earth orbit by object type (Science Technology Policy, 1995). Since space exploration has begun for the first time in the world since October 1957, more than 5160 space missions have been conducted worldwide (Office, 2019). However, only 10 missions now account for approximately one-third of all cataloged objects in orbits. For instance, the source of the greatest amount of debris was an anti-satellite test by China in January 2007. The Fengyun-1C spacecraft was used as a target. It now accounts for 3428 cataloged fragments (almost 20 percent of the entire population of cataloged man-made objects). The second and fourth most significant satellite breakups are Cosmos 2251 and Iridium 33 spacecraft, which were involved in the first ever accidental hypervelocity impact of intact objects in February 2009. Over 68 percent of the Cosmos debris cloud and 58 percent of the Iridium could be still in orbits and present a hazard for decades to come because of their relatively high altitude.

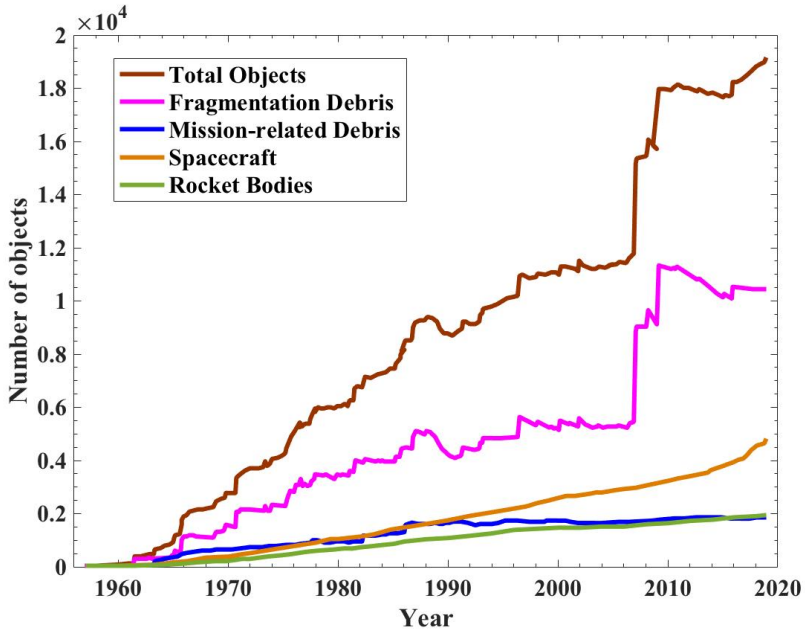

FIGURE 1.1: Monthly number of objects in Earth orbit by object type

Most of debris particles exist in LEO and GEO. The density of debris corresponds to that of materials used for spacecraft. It is between 1.8 g/cm^3 and 8.9 g/cm^3. About 50 to 60 percents of the debris particle have a density of 2.8 g/cm^3 (aluminum alloys and glass)(Ley, Wittmann, and Hallmann, 2009; Kessler, Reynolds, and Anz-Meador, 1994).

There are much more debris particles with less than 5 cm in a diameter, which cannot be tracked by SSN. It is commonly referred to as small objects and it is said that over 10 million objects are in orbits (Science Technology Policy, 1995). Spacecraft orbiting around the Earth has the possibility to collide with small debris with less than millimeter in a diameter once a year. Especially, the International Space Station (ISS), orbiting at approximately 400 km in an altitude is a manned spacecraft that carries astronauts, and when it collides with debris, there is a risk of not only the bodies of spacecraft but also human life. The measures against collisions with debris particles at the ISS has been made by distinguishing three debris sized ranges: sizes below 0.01 cm, sizes 0.01 cm to 1cm, and objects larger than 1 cm.

For larger sizes of debris, a collision avoidance system is working. NASA usually gets a warning that something might come too close to the ISS several days in advance, and then the ISS escapes by firing thrusters. That has happened 21 times from 1999 to 2014 (Office, 2015; Office, 2012). Meter-sized objects have a hazard to be a source of debris by collision. These days, various active debris removal systems have been considered (Kawamoto et al., 2018; Liou, 2011; Bonnal, Ruault, and Desjean, 2013). Also, the debris environment model were developed to simulate how frequently spacecraft will collide with debris. The National Aeronautics and Space Administration (NASA) offers the Orbital Debris Engineering Model (ODEM) (Liou, 2002), European Space Agency (ESA) offers the Meteoroid and Space Debris Terrestrial Environment Reference (MASTER)(Oswald, 2005), and Japan Aerospace Exploration Agency (JAXA) offers Tactical Utility for Rapid ANalysis of Debris on Orbit Terrestrial (TURANDOT) of the space debris collision damage analysis tool(Kim et al., 2013). The surface area flux as a function of particle diameter as computed with ORDEM2000 for the year 2010 is shown in Fig. 1.2 (Ley, Wittmann, and Hallmann, 2009). For smaller sizes of debris, the bodies of the ISS can be shielded by the bumper against debris particles up to 1 cm in a diameter (Whipple, 1947) even though the solar array paddle cannot be protected by micrometeoroids and orbital debris (MMOD) collisions. The collision probability of a 1 mm-diameter sized debris in LEO would collide with solar panel with a surface area of 25 mm^2 is once every five years. In addition to ISS, the collisions with MMOD are unavoidable in large-scale spacecrafts. Especially, one of the typical examples of the future large-scale structure is the solar power satellite (SPS) (Glaser, 1968; S. Sasaki, 2013b). The SPS mainly consists of thin film solar arrays and thin planar antennas in km-scale and will be orbited in GEO. In the GEO, the impact probability of the MMOD collisions larger than 1mm in size is approximately 2400 times/year$\times$ km ^{2} (S. Sasaki, 2013a).

To prevent from creating more debris, a guideline of mitigation measures was enacted. The Inter-Agency Space Debris Coordination Committee (IADC) published the guideline of mitigation measures in 2007 (IADC-08-03, 2007). According to the guideline, spacecraft and orbital stages should be designed

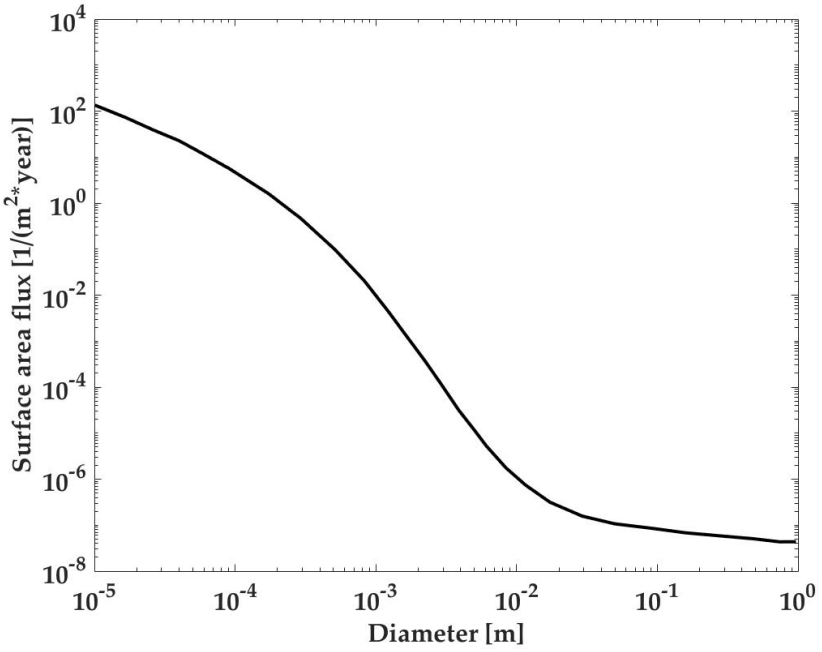

FIGURE 1.2: Accumulated surface area flux as a function of particle diameter in the year of 2010 (height: 400km, inclination: 51.6 deg.)

not to release inactive payloads and objects released during satellite deliveries or satellite operations. To prevent the breakup of stored energy of spacecraft or orbital stage, equipment such as residual propellants, batteries, and high-pressure vessels should be depleted. Intentional destruction of a spacecraft should be avoided. When a spacecraft is no longer required for mission operations, it should be left operational orbits such as LEO or GEO regions. In the process of developing the design of a spacecraft, the probability of accidental collision should be estimated.

1.2 Mechanical Phenomena Subjected to Hypervelocity Impacts

The velocity of debris depends on orbits. The velocity at LEO is approximately 7 - 8 km/s and one at GEO is approximately 3 km/s. Debris commonly collides with spacecraft at approximately 10 km/s in LEO although it depends on an inclement angle (Kessler and Cour-Palais, 1978). The velocity is called 'hypervelocity'. The term "hypervelocity impact" is used to mean impacts in excess of the sound speed in the material of interest in this thesis.

Hypervelocity impact on spacecraft induces mechanical phenomena such as destruction and small fragments (i.e. secondary debris). To understand impact effects on spacecraft, the ground-based experiments using accelerators such as rail gun or gas gun have been conducted (Kawai et al., 2010; Friichtenicht, 1962). Rail gun is an electromagnetic launcher, which generates powerful electrical pulses that in turn produce strong electromagnetic forces that accelerate projectiles to extremely high velocities. Gas gun is also a launcher that is a specialized gun designed to generate very high velocities, and the principle is described in Chapter 2.

An empirical understanding of the size of craters or holes produced by hypervelocity impacts on surfaces over a range of materials properties and impact speeds (Ley, Wittmann, and Hallmann, 2009; Burchell and Mackay, 1998; Piekutowski, 1993; Piekutowski, 1995). The protective design for the important components of the spacecraft is required. Hypervelocity ballistic properties of honeycomb structures representative of satellites structural bodies were investigated (Sibeaud, Thamie, and Puillet, 2008). Based on experimental results, the numerical simulations were developed (M. S. Cowler and Obata, 1987; Mechanical Engineers, 2007). The response of an aluminum honeycomb structure to hypervelocity impacts of 6 km/s is investigated(Nitta et al., 2013). They compared with the experimental results and numerical results of the AUTODYN-2D hydro code. Carbon fiber reinforced plastic (CFRP) is also well known as a high-strength and light-weight material. Higashide et al. evaluated availability of CFRP bumper shields (Higashide et al., 2009; Higashide et al., 2015). They investigated hypervelocity impact phenomena of CFRP-AL honeycomb sandwich structure (Higashide et al., 2010). Therefore, much research have been done to protect against MMOD collisions.

1.3 Electrical Phenomena Caused by Hypervelocity Impacts and Their Effects on Spacecraft

Hypervelocity impacts cause not only mechanical phenomena, but also electrical phenomena such as generation of luminous vapor cloud including neutral gas and plasma, radio frequency (RF) emissions, and potential variation of an impacted target. Yet, electrical phenomena have not been gained attentions comparing to mechanical phenomena. Also, the electrical anomalies of spacecraft are difficult to clarify and diagnosis because of limited data. Some spacecrafts may have occurred during MMOD cause. Figure 1.3 shows causes of spacecraft anomalies(McKnight, 2016). Half of the anomalies are of known

cause. The 25 percent design category includes hardware, software, and operator error. Electrostatic discharge is largely correlated to solar array failures while single event upsets are highly correlated to computer anomalies.

So far, electrical anomalies of several spacecraft were reported. The Olympus spacecraft lost attitude control because of a gyro anomaly by the meteoroid shower in 1993 (Caswell, McBride, and Taylor, 1995). Though control of the spacecraft was restored, the unforeseen fuel expenditure resulted in a premature termination of the mission. The ADEOS-2 and ALOS satellites experienced power system failures during the 2003 Orionids and the 2011 Lyrids, respectively, resulting in total loss of mission (S. Hosoda, 2006). In 2009, a gyro anomaly occurred on the Landsat 5 spacecraft during the meteoroid shower (*Historic Landsat 5 Mission Ends*). The Jason-1 satellite experienced a confirmed impact that changed its orbital axis by 30 cm and subsequently reported anomalous solar array currents lasting for five hours after the impact. Bedingfield et al. list many spacecraft that have experienced electrostatic discharge (ESD)-related anomalies (e.g., Fengyun-1, AusSat-A3, Intelsat 511, Telecom 1B, Intelsat 510, Arabsat 1-A, and Anik-D2) (Bedingfield, Leach, and Alexander, 1996). The triggers of these ESD events are not identified, but many are likely a result of solar activity or some other factors that may have been caused by MMOD impacts. Therefore, it is necessary to clarify electrical phenomena caused by hypervelocity impact and their effects on spacecraft by conducting the ground-based experiments.

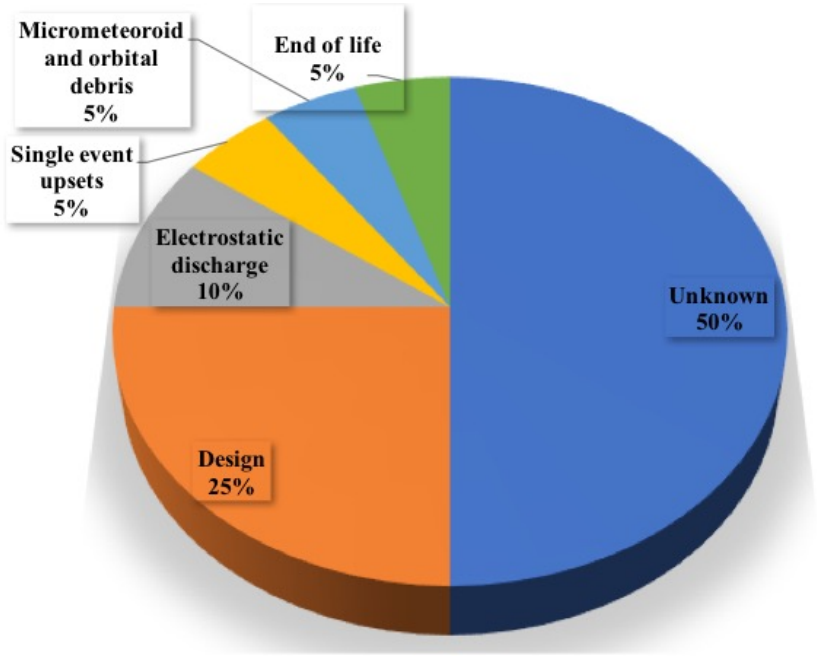

FIGURE 1.3: Half of the anomalies are of unknown cause

1.4 Motivation

There are five chapters in my dissertation in Fig. 1.4. In Chapter 1, the introduction of my research field was described. Debris impact with spacecraft, causing mechanical phenomena as well as electrical phenomena. Research on electrical phenomena caused by hypervelocity impact has gained less attention than research on mechanical phenomena. Therefore, I focused on electrical phenomena from hypervelocity impacts and hypervelocity impact experiments using a two-stage light gas gun were conducted.

In Chapter 2, the plasma density and propagation of impact plasma are important to estimate the risk of discharge to a spacecraft. I conducted the hypervelocity impact experiments to accurately determine plasma density and temperature of impact plasma.

In Chapter 3, the solar panels and power harnesses are affected by not only mechanical failure but electrical one. The electrical failure means that impact plasma including a high-density plasma density may trigger to discharge, but the effects on power harnesses has not been clarified. I carried out the hypervelocity experiments on power harnesses and the relationship between impact plasma and discharge was investigated based on the achievement of Chapter 2.

Microwave emission phenomenon was investigated in Chapter 4. The mechanisms of microwave emissions have been proposed, but a complete explanation has not been reached. I measured electrical phenomena of impact plasma, microwave emission simultaneously and the relationship between microwave emissions and impact plasma phenomena was clarified. Also, the mechanism of microwave emissions was clarified by conducting hypervelocity impacts experiments on various kinds of aluminum targets.

Lastly, summaries of each chapter and the contributions are described in Chapter 5.

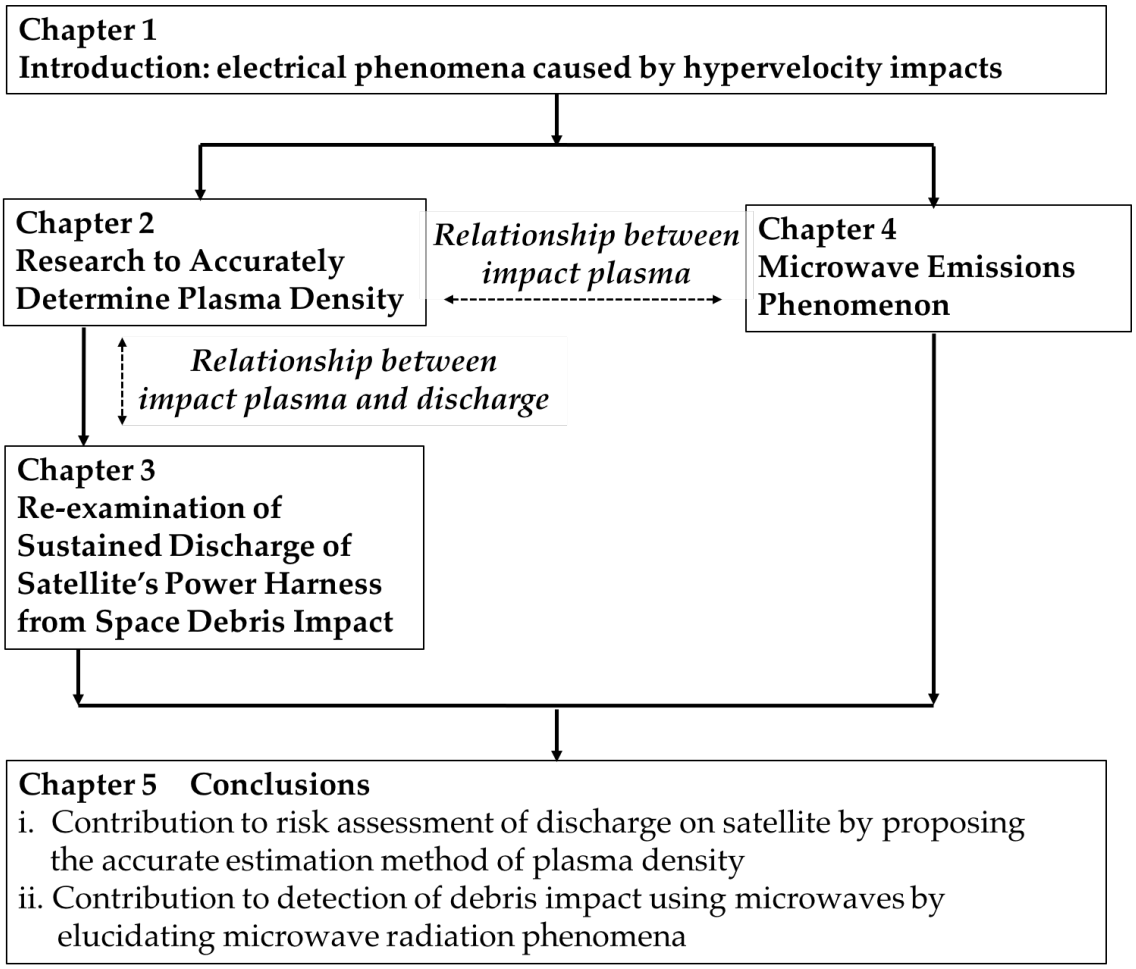

FIGURE 1.4: The flow of my dissertation

Chapter 2

Research to Accurately Determine Plasma Density

2.1 Introduction

When debris collides with spacecrafts at hypervelocity, ejecta is generated. The ejecta includes not only secondary debris, but the luminous vapor cloud with high-temperature gas and impact plasma because the collision site between the projectile and the target is highly pressurized (Friichtenicht and Slattery, 1963; Eichhorn, 1976). Sugita et al. investigated intensities of atomic lines from the impact-induced luminous cloud using a spectroscopy (S. Sugita and Hasegawa, 2003).

Regarding of impact plasma generated by hypervelocity impact, plasma charge and the measurements of plasma parameters have been researched. Much of the research on plasma charge have been done to calibrate the small particle collision detectors on-board spacecraft. Based on the empirical formula obtained from the calibration experiment of the on-board detector, the data obtained by the detector were analyzed. Also, the knowledge about the characteristics of the collision object and the micrometeoroid distribution was obtained (Friichtenicht and Slattery, 1963; H. Iglseder, 1987). Electrodes with positive and negative bias voltages applied in the vicinity of the collision part and the collision part are installed. The positive and negative charges of the plasma generated by the collision were measured using a charge amplification type amplifier (H. Dietzel, 1973; N. McBride, 1999). It was clarified that the total plasma charge is proportional to the collision mass and velocity.

Measurements of plasma density and temperature are important to estimate the risk of discharge to a spacecraft (Stevens, 1986). There are some plasma diagnosis methods. They can examine plasma parameters locally by placing multiple probes. There are three kinds of probe methods: single probe, double probe, and triple probe methods (Mott-Smith and Langmuir, 1926; Johnson and Malter, 1950; S. Chen, 1965). The density of impact plasma has been measured by a single probe method (D. A. Crawfield, 1991). In the single probe method, the plasma temperature and density can be obtained by sweeping the bias voltage to one electrode. They measured plasma temperature and density of impact plasma generated by hypervelocity impact from an aluminum particle on an aluminum plate. The bias voltage of sinusoidal wave at 5 kHz (the periodic time: 200 μs) in frequency is applied to the electrode, but

it is considered that the measurement is not appropriate, because the applied frequency was low compared with the phenomenon of the impact plasma.

The impact plasma was measured from hypervelocity impacts on solar array with power supply by using a triple probe method (E. Tang, 2018). The triple probe was set nearby the impact site. They found that the plasma temperature and density are several eV and the order of 10^8 cm^{-3} during milliseconds, respectively. However, it is considered that the measurement of plasma temperature and density may be inappropriate because impact plasma disappears within the order of microseconds. The triple probe method is usually a method in which the plasma density and temperature can be obtained instantaneously using three electrodes. Yet, it is difficult to determine the circuit conditions such as an appropriate bias voltage or resistance according to the impact plasma.

Nagaoka et al. have investigated the propagation of impact plasma using the double probe method (Nagaoka, Tanaka, and Sasaki, 2012). It is difficult to measure plasma density and temperature by the conventional double probe method (Johnson and Malter, 1950), because the propagation of the impact plasma is a short-time phenomenon. Herein, they measured the plasma current from double probes applied to a constant bias voltage of 9.6 V, which is enough to get the ion saturation current. The plasma temperature to calculate plasma density was assumed to be the same temperature as the luminous vapor cloud which was derived by using a spectroscopic method under the black-body radiation.

The spectroscopic method is one of the plasma temperature methods. Attempts have been made to measure the plasma temperature using the spectroscopic method applied the specific several wavelengths of emission from the luminous vapor cloud (Kadono, 1996; Nagaoka, 2013; K. Zhang and Ju, 2016). They estimated the temperature of luminous vapor cloud by fitting the equation of the Blackbody radiation from the intensity ratios at 500, 700, and 900 nm. However, there is a possibility that an error may occur in the temperature calculation if emission line spectra derived from projectile and target materials are observed at the wavelengths.

Besides that, plasma density has been obtained by using plasma temperature and ion mass constituting impact plasma. With respect to ion mass, the plasma density has been calculated assuming the ion mass of either target or projectile material when impacts between the different target and projectile materials.

In Chapter 2, the hypervelocity impact experiments using a two-stage light gas gun (LGG) were conducted. I used the streak camera spectroscopy, high-speed video camera, and double probes to measure and observe the ejecta generated by hypervelocity impacts. First, the temperature of the luminous cloud was calculated from the time-resolved spectrum acquired with the streak camera spectroscopy. The temperature change of the luminous cloud was compared with the photos taken by the high-speed video camera. Secondly, the composition of the ejecta was examined by comparing the emission line spectra, which are originated by the projectile and target materials, measured with a streak camera spectroscopy. Third, plasma density is calculated by the above

results in the case of the impacts between different projectile and target materials.

2.2 My Experimental Facilities

The hypervelocity impact experiments were conducted using the LGG of JAXA/ Institute of Space and Astronautical Science (ISAS). Figure 2.1 shows a photo of the experimental facility. The LGG is connected to a launch tube and vacuum chambers. The diagram is shown in Fig. 2.2. A piston is pushed by exploding gun powder in a combustion chamber at the first stage. At the second stage, a projectile is pushed by hydrogen and helium gas, which are compressed from the pushed piston. By using light gas, the projectile can be accelerated many times more than in the air.

The projectile with a mass of approximately 0.2 g at the maximum can be accelerated up to approximately 7 km/s. The diameter of a projectile is up to 7 mm, because it is limited by the diameter of the launch tube. In the experimental facility, various kinds of projectile materials, which are usually orbiting on space, are used as shown in Fig. 2.3. For metal balls, the diameter of projectiles is restricted up to 3.2 mm, because metal balls are heavier than nylon ball. A container called a sabot that holds the metal ball is used as shown in Fig. 2.4.

Figure 2.5 shows lasers and photomultipliers. Three sets of the lasers and the photomultipliers were used for measuring a velocity of the projectile. The velocity of the projectile is calculated from the distance and the time difference from the three sets of photomultipliers installed between the launch tube and the metal vacuum chamber. The signal detected from photomultipliers is also used for a trigger and all experimental devices are synchronized. On the downstream side of the LGG, a sabot separator, a metal vacuum chamber, vacuum devices such as a rotary pump or a refrigerator and an acrylic vacuum chamber are arranged. A target was placed in the acrylic vacuum chamber. The degree of vacuum was measured with an ionization vacuum gauge.

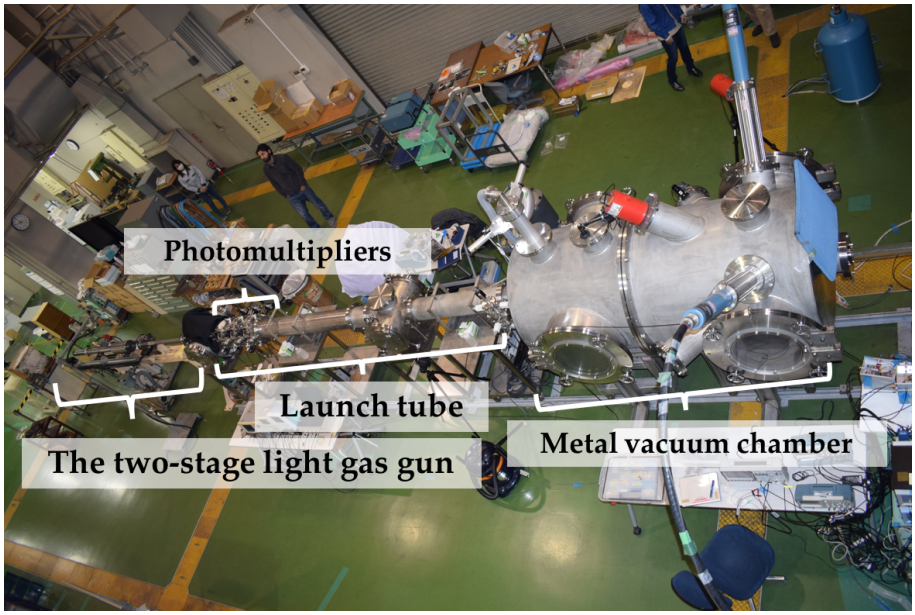

FIGURE 2.1: The photo of the experimental facility

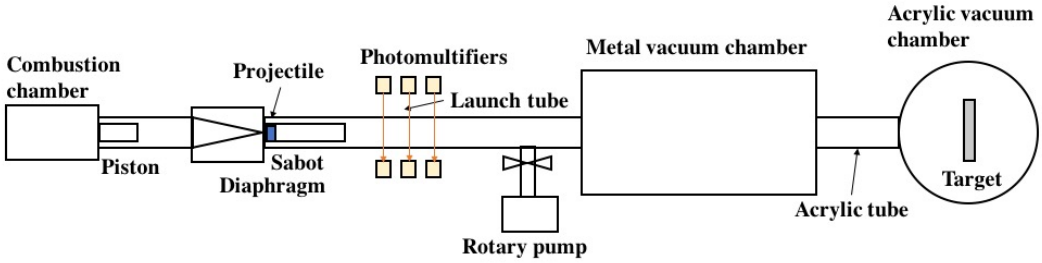

FIGURE 2.2: The diagram of the two-stage light gas gun

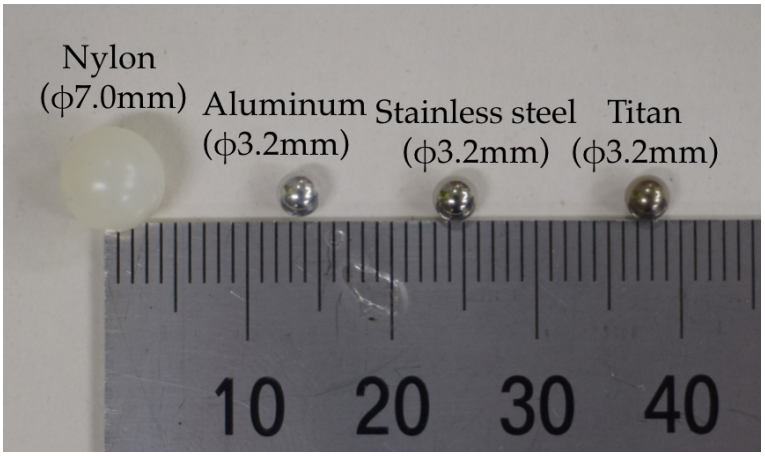

FIGURE 2.3: The photo of projectiles

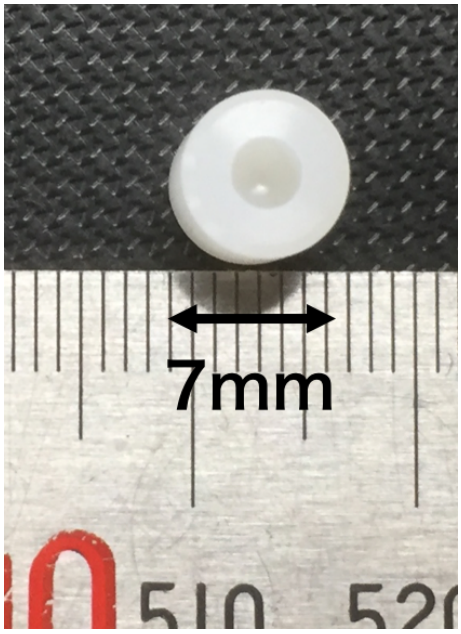

FIGURE 2.4: The photo of the sabot

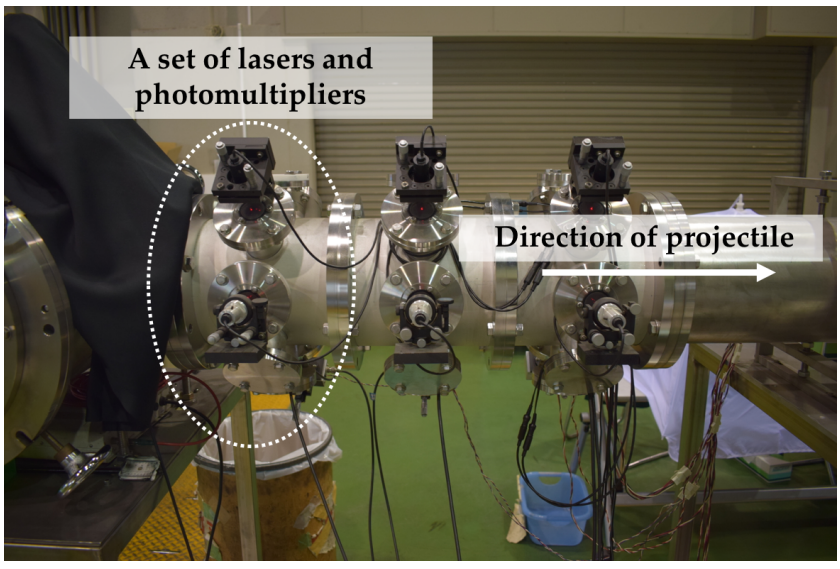

FIGURE 2.5: The picture of three sets of photomultipliers

2.3 Experimental Setups for Measuring Luminous Vapor Cloud and Plasma

To measure ejecta from hypervelocity impacts, I used a high-speed video camera, double probes, and a streak camera spectroscopy. The experimental setups for measuring the ejecta is shown in Fig. 2.6. It is possible to measure and observe an optical phenomenon by using the 'acrylic' vacuum chamber. Each measuring device will be described later.

The high-speed video camera is located at the perpendicular to the target to observe the luminous cloud two-dimensionally. The streak camera spectroscopy is connected to an optical fiber. The field of view of optical fiber focuses on the surface of the target. Arrays of plasma probes are used for investigating the expansion of the plasma in the chamber.

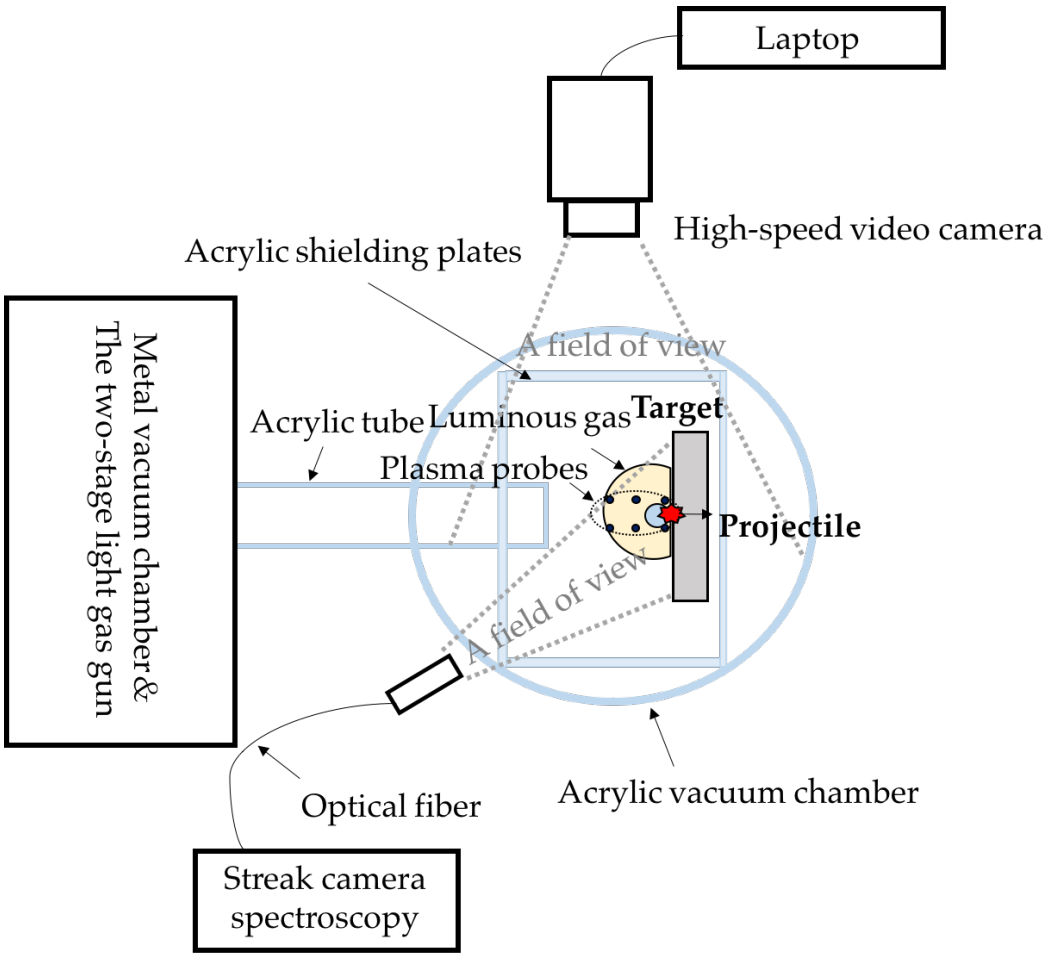

FIGURE 2.6: The configurations of experimental setups for measuring the ejecta

2.3.1 The Streak Camera Spectroscopy

The streak camera spectroscopy measurement was mainly used for two purposes: an acquisition of temperature and an investigation of plasma composition. The streak camera spectroscopy constitutes of a spectroscopy, a streak tube, and a charge-coupled device (CCD) imaging. It is a device that can capture the light emission phenomenon that occurs within a very short time, and not only the temporal change but also the spatial change at the same time. The output is called "time-resolved spectrum". The wavelength range with 547 nm to 872 nm was selected so that the light is able to penetrate the acrylic vacuum chamber. Also, the observation time of 100 μs was selected to be enough to observe the flash. The time resolution is 1 μs.

The principle of the streak camera spectroscopy is shown in Fig. 2.8 (*Streak Camera Handbook*). It is imaged as a slit image on the photocathode of the tube. The photocathode converts incident light into a number of electrons corresponding to its intensity. It is accelerated by the accelerating electrode and jumps out toward the phosphor screen. The electron is swept at high speed by the high voltage applied to the sweep electrode, and the electron is deflected and incident the microchannel plate (MCP) that electron is amplified. The amplified electron collides with the fluorescent screen and is converted to light again. The intensity of the incident light is detected by the brightness of the fluorescent image, and the time and space are detected from the position. The emission line spectrum was measured so as not to saturate the number of photons. A color bar indicates an intensity of the time-resolved spectrum.

Before the experiments, preliminary tests were performed. A halogen lamp with a color temperature of 3,170 K was set near the impact point of the target. The spectrum emitted from the halogen lamp were measured. The model spectrum of the halogen lamp was divided by the spectrum measured in the calibration experiment of the halogen lamp, and the spectrum measured by multiplying the spectrum measured in impact experiments were confirmed. The wavelength resolution of the streak camera spectroscopy using a mercury lamp was investigated. The emission lines of the mercury compared with the mercury emission lines published by the National Institute of Standards and Technology (NIST) (*National Institution of Standard Technology (NIST)*). The wavelength resolution of full width at half maximum (FWHM) is approximately 5.7 nm.

Figure 2.9 shows the flow chart of analyzing the time-resolved emission spectra. From the time-resolved spectrum, the continuous spectrum radiated from the luminous vapor cloud and the emission line spectrum originated from the target and the projectile material are observed. First, the spectrum of each time is integrated from the obtained time-resolved spectrum. Elements are identified according to the NIST database.

The temperature of the luminous vapor cloud is calculated from the intensity ratio of spectrum at the observed wavelengths assuming blackbody radiation. Temperature of luminous vapor cloud is calculated excluding the emission line spectrum.

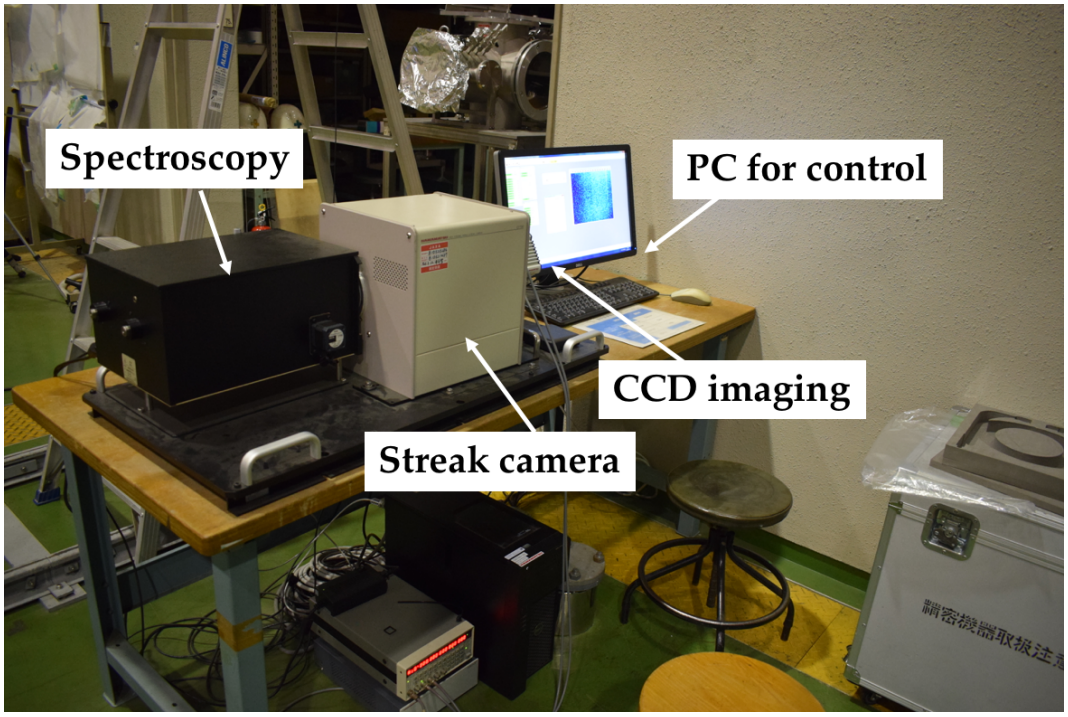

FIGURE 2.7: The photo of streak camera spectroscopy

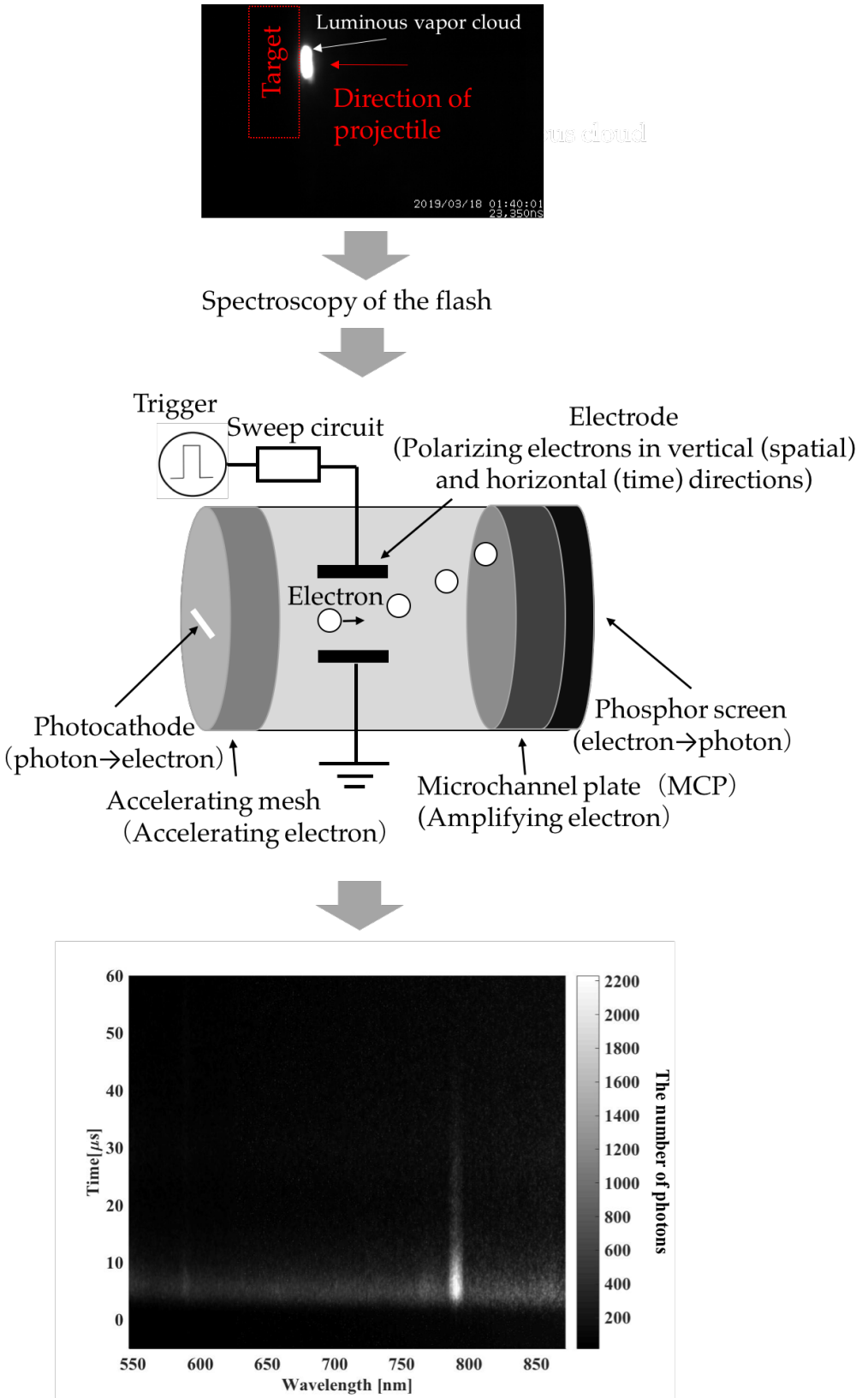

Recording the light on phosphor screen with CCD imaging and "the time-resolved spectrum" is obtained

FIGURE 2.8: The principle of the streak camera spectroscopy

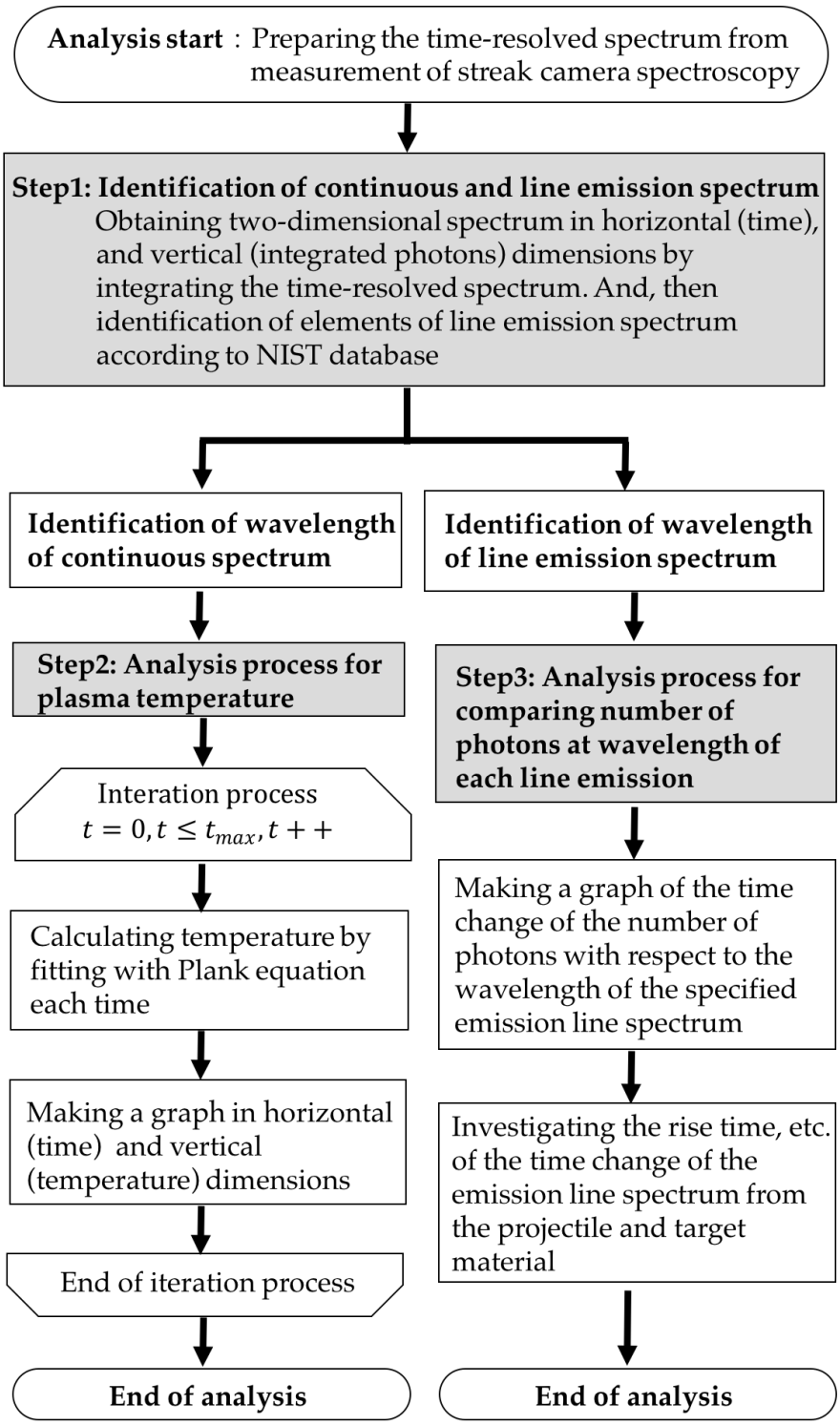

FIGURE 2.9: The flow chart of analyzing the time-resolved spectrogram

2.3.2 High-speed Video Camera

To capture the expansion of the luminous vapor cloud, the high-speed video camera was used. An expansion of the luminous vapor cloud is a short-time phenomenon. In Fig. 2.10, the high-speed video camera of the Hyper Vision HPV-X (Shimadzu Corporation) was used. The flame rate of 2 μs and the number of flames of 128 photos are set to be satisfied to observe the optical phenomenon. The camera is connected to a laptop for control.

FIGURE 2.10: The picture of a high-speed video camera

2.3.3 Double Probe Measurements

An expansion of plasma was investigated by setting arrays of double probe inside the chamber. Figure 2.11 shows the circuit diagram of double probe measurements. Normally, in plasma measurement, plasma density is calculated from the relationship between the applied voltage and the current to the plasma electrode by sweeping the voltage applied to the probe electrode, but a constant voltage of 9.6 V is applied between electrodes, which is considered sufficient for measuring the ion saturation current (i.e. plasma current). The capacitor is inserted to suppress fluctuations in power supply voltage due to sudden current surge due to impact plasma. The probe electrode has a cylindrical shape with a diameter of 2 mm and a length of 10 mm. The distance between electrodes is 10 mm. The distance was decided so as not to be affected by the sheath. Plasma current I_p is given by the following Eq. 2.1

$$I_p = 0.61 N_e e S \left(\frac{kT_e}{m_i} \right)^{1/2} \tag{2.1}$$

with, m_i, k, e, and S are the ion mass, Boltzmann constant, elementary charge, and probe surface area, respectively. I_p through the resistance R of 100 - 300 Ω was recorded with a data logger (8 channels isolated input, SL1000, Yokogawa). The data logger has a frequency range from DC to 20 MHz, and a sampling frequency of 100 MS/s. The input impedance is 1 MΩ . I_p and T_e obtained from the spectroscopic measurement were used for calculating N_e .

The configuration of probe electrodes are shown in Fig. 2.12. The array of plasma electrodes arranged 85 mm (Ch.1), 115 mm (Ch.2), and 180 mm (Ch.3) apart from the impact point.

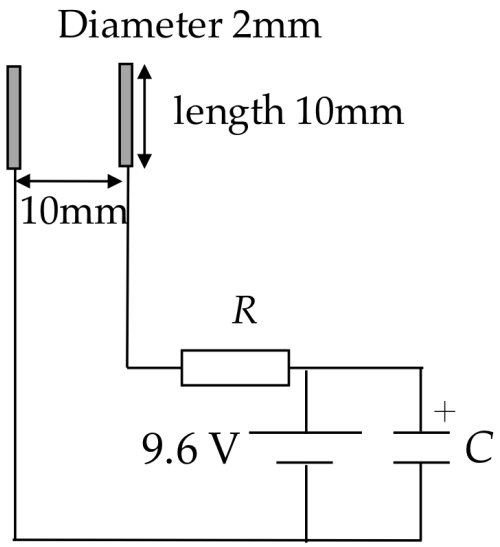

FIGURE 2.11: The circuit diagram of double probes

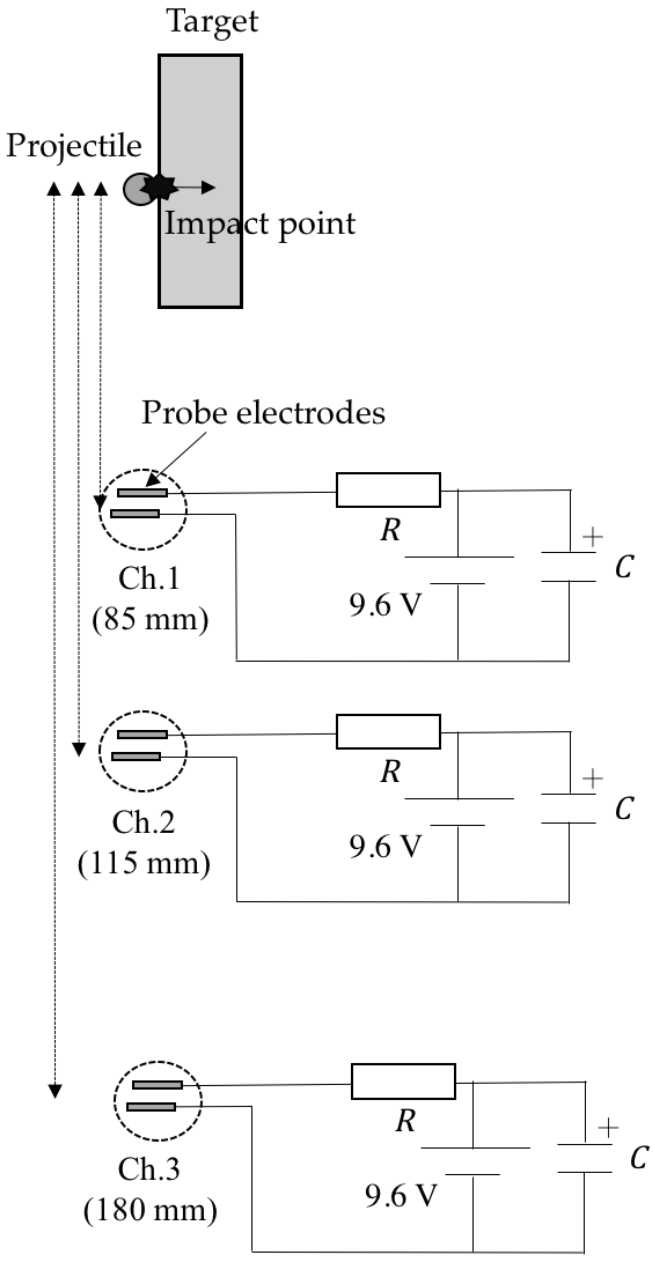

FIGURE 2.12: The position of each electrode

2.4 Experimental Condition

The experimental condition is shown in Tab.2.1. The main purpose of the experiments is to obtain the temperature of the luminous vapor cloud and investigate line spectrum derived from the different target and projectile materials. Some impact experiment between the same projectile and target materials were carried out to identify the line spectrum of aluminum or carbon. Basically, an aluminum and a copper plates are used for a target. An aluminum (A5052 (Al-Mg)), a nylon (nylon 66), and a titan sphere were used for a projectile. The various kinds of aluminum plates are selected to investigate line spectrum derived by the impurities of aluminum alloy. Herein, the compositional components contained in each aluminum alloy are shown in Tab. 2.2 (Japan, 2001).

TABLE 2.1: The experimental condition.

Shot ID	Target	Size [mmxmm]	Thickness[mm]	Projectile	Diameter[mm]	Velocity[km/s]	Pressure[Pa]
#190702	A5052(Al-Mg)	110x110	40	Aluminum	3.2	6.8	0.1
#180905	A5052(Al-Mg)	110x110	40	Aluminum	3.2	6.8	1.0
#190303	Nylon	110x110	40	Nylon	7.0	7.1	0.5
#180903	Pure aluminum	110x110	40	Nylon	7.0	6.0	1.0
#180901	A5052(Al-Mg)	110x110	40	Nylon	7.0	7.1	1.0
#180902	A7075(Al-Zn-Mg)	110x110	40	Nylon	7.0	7.1	1.0
#190301	Aluminum(6061)	110x110	40	Nylon	7.0	7.1	1.0
#190707	A5052(Al-Mg)	110x110	40	Titan	3.2	6.8	2.0
#180909	A5052(Al-Mg)	110x110	40	Titan	3.2	6.8	1.0
#190703	Copper	110x110	40	Aluminum)	3.2	6.7	0.1
#190305	Copper	110x110	40	Aluminum	3.2	7.0	1.0
#190306	Copper	110x110	25	Titan	3.2	6.8	1.0
#190705	Copper	110x110	50	Titan	3.2	7.2	0.5

TABLE 2.2: The chemical composition of various aluminum targets.

Composition	A1050 [%]	A5052 [%]	A6061 [%]	A7075 [%]
Al	> 99.50	remain	remain	remain
Si	0.25	0.25	0.40 - 0.80	0.40
Fe	0.40	0.40	0.7	0.50
Cu	0.05	0.10	0.15 - 0.40	1.2 - 2.0
Mn	0.05	0.10	0.15	0.30
Mg	0.05	2.2 - 2.8	0.8 - 1.2	2.1 - 2.9
Cr	-	0.15 - 0.35	0.40 - 0.35	0.18 - 0.28
Zn	0.05	0.10	0.25	5.1 - 6.1
Ti	0.03	-	0.15	0.20

2.5 Temperature Estimation of Luminous Vapor Cloud

Fig. 2.13 shows a photo of crater on the surface of the 6061 aluminum alloy target from the impact of the nylon projectile. The diameter and volume of the crater is 27 mm and 2290 mm^3, respectivity. It is also confirmed that the surface condition of the crater is melted and the rim is raised.

Figure 2.14 shows the expansion of luminous vapor cloud from impacts. A luminous vapor cloud is generated from the collision point and the expands in the surrounding space in vacuum. The impact flash originates from radiation from the hot gas, and the emission line of state transition from the gas with the excited state. Also, it is clear from the surface condition of the crater in Fig. 2.13 that the collision interface is in an ultra-high pressure state and phase transition occurs.

The intensity increases up to 10 μs, and then it can be seen that the intensity gradually decreases. This is because the luminous vapor cloud spreads into the surrounding space in vacuum. It is suggested that this is an apparent phenomenon due to the weakening of the emission intensity per volume. In addition, the expansion velocities were calculated by tracking the edges of luminous vapor cloud. The expansion velocity at a speed of 8 km/s in the horizontal direction, and 19 km/s in the perpendicular direction. The expansion velocity tends to increase with a closer to the surface of the target. After 14 μs, it can be seen that secondary light emission from other areas except for the collision point. There are frames for putting target, acrylic tube, and acrylic shielding plates in approximately 30 cm away from the impact point. Taking account in the expansion velocity of 8 km/s to 19 km/s, the luminous vapor cloud including the secondary debris hits them in 15.8 μs to 37.5 μs. Therefore, it is considered that the secondary debris impact on them and light emission generated again.

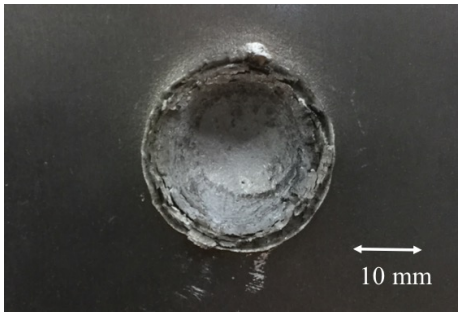

FIGURE 2.13: The crater created on the surface of the 6061 aluminum alloy plate

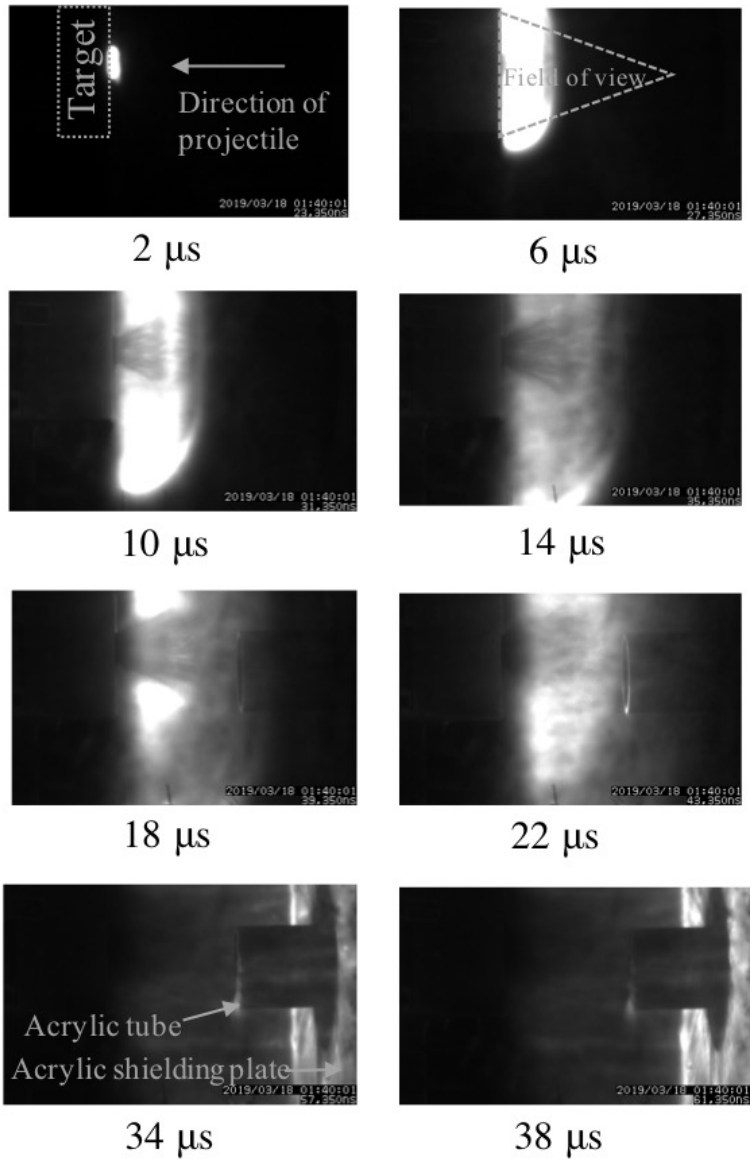

FIGURE 2.14: The photos of the expansion of the luminous cloud

Figure 2.15 shows the time-resolved spectrum. The horizontal axis indicates the wavelength and the vertical axis indicates the time. The color bar indicates the intensity. Until 5 μs after the impact, it was confirmed that the number of photons increases rapidly at all wavelengths and then decreases. Herein, the temperature of the luminous vapor cloud was calculated according to the procedure which is described in Fig. 2.9.

Figure 2.16 shows the spectrum obtained by integrating the time-resolved spectrum. The emission line spectrum derived from the aluminum element was observed at three wavelengths of 586.8 nm, 766.0 nm, and 788.3 nm. Also, an impact experiment between the target and the projectile material of nylon was conducted to investigate the emission line derived from carbon which is nylon constituting the main element. Yet, there is no emission line spectrum derived from carbon.

Also, impact experiments using various aluminum alloys and pure aluminum were carried out. However, there is no emission line spectrum derived from the impurity elements as shown in Tab. 2.2 in all cases. It is suggested that the emission line derived from the impurity elements could not be confirmed because ratio of impurity elements is too small comparing to the ratio of aluminum element.

Based on the above, the temporal temperature is calculated by using intensity ratio of continuous spectrum excluding the three wavelength emission line spectrum and the spectrum below 566 nm, which is a possible emission line spectrum.

An example of the temperature calculation process is shown in Fig. 2.17. By excluding the entire part of the observed emission line spectrum, the temperature can be calculated from the intensity ratio assuming the Blackbody radiation. Thus, the temperature can be calculated with a wider bandwidth and higher sampling rate.

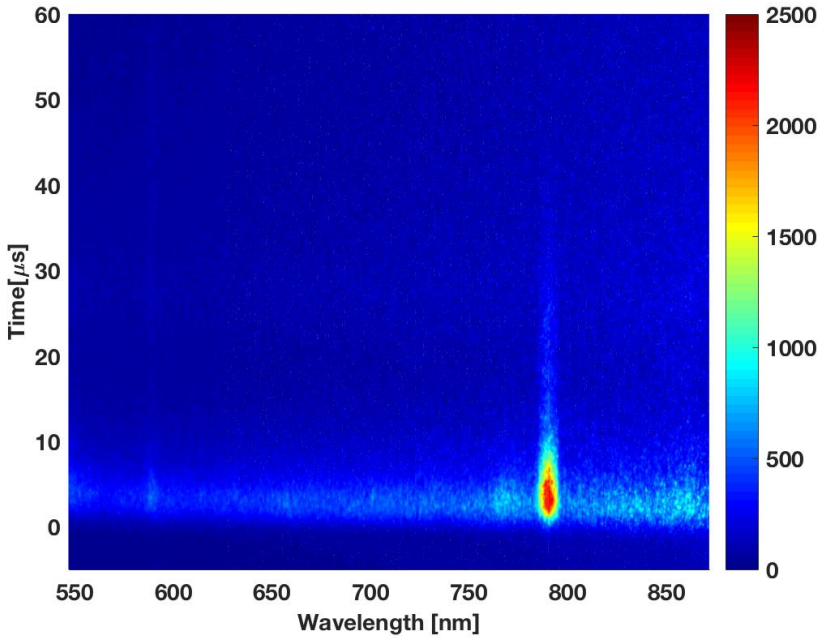

FIGURE 2.15: The time-resolved emission spectra (6061 aluminum alloy plate vs nylon projectile

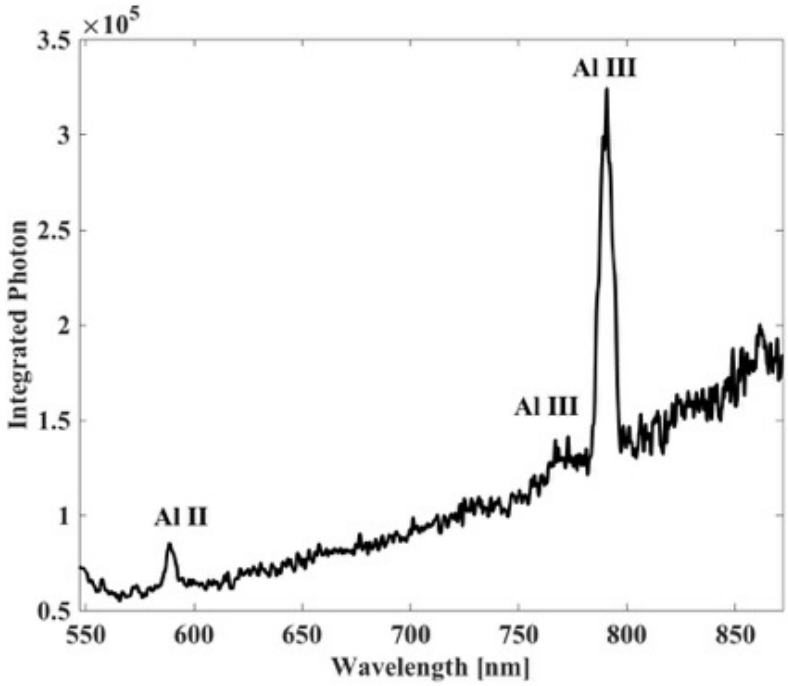

FIGURE 2.16: The integration of the time-resolved emission spectra (6061 aluminum alloy plate vs nylon projectile

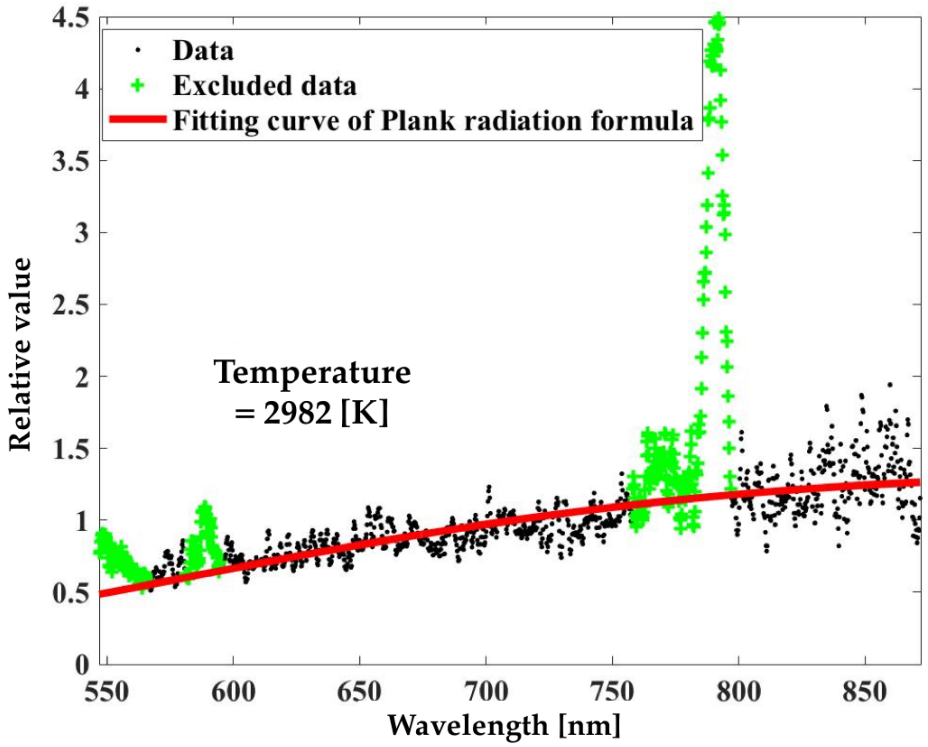

FIGURE 2.17: The typical example of estimating the temperature

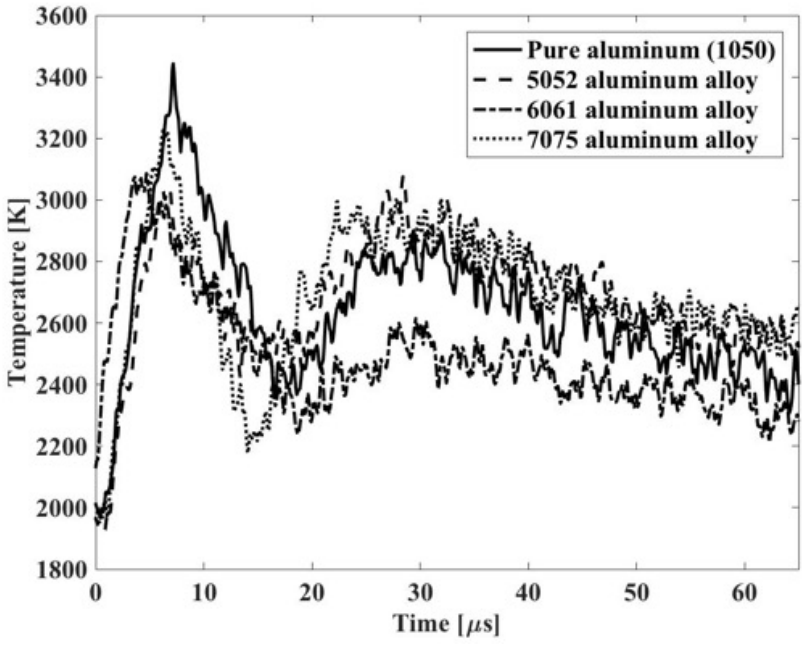

FIGURE 2.18: The temperature of the luminous cloud with time

Figure 2.18 shows the results of temperature calculation. The maximum temperatures of the luminous vapor cloud rises 6 μs to 7 μs and reach from 3,084 K to 3,444 K. The temperature indicates the average temperature within the field of view. The radius of the observation field is 55 mm and the expansion velocity of the luminou vapor cloud is 8 km/s, the cloud expands within the observation field within 7 μs. Therefore, the temperature rises because flash from luminous vapor cloud expands within the field view of the optical fiber until 7 μs. After that, it is considered that about 1.6 to 16 collisions with residual gas per particle occur, and it is dominent that the energy is lost due to the collision because the mean free path of 6.7 mm to 67 mm in vacuum is smaller than the observation field. Hence, it is suggested that the temperature decreased because the energy loss became dominant.

In addition, after approximately 20 μs to 30 μs after the collision, the temperature increased again due to the secondary light emission. The light emitted from the vacuum chamber wall is thought to have been measured by the streak camera spectroscopy.

The results of temperature are described in the case of the impacts on the different conbinations of target and projectile materials. Figure 2.19a compares the temporal change of temperature with the aluminum and the titanium sphere projectiles on the A5052 (Al-Mg) aluminum target. It was found that the temperature of the maximum temperature of aluminum and titanium projectile is 3,959 K after 4 μs and 3,798 K after 4 μs, respectivity. Figure 2.19b shows the temporal changes of temperatures due to the impact on the copper plate. it was found that the temperature of the maximum temperature of aluminum and titanium projectile is 4,377 K after 6 μs and 2,660 K after 6 μs, respectivity.

In this way, the luminous vapor cloud was analyzed by comparing the calculated temperature and the expansion of the emission cloud taken by the high-speed video camera. In the conventional method (Kadono, 1996)(Nagaoka, 2013), the temperature was estimated by fitting intensity ratio at three wavelengths. However, the temperature cannot be estimated when the emission line spectrum is superposed within the observed wavelength. The additional experiment to verify it was conducted. The details are described in Appendix B.

The comparison between the conventional method and my proposed method is summarized in Tab. 2.3. The wavelength resolution of 40 nm is restricted to the wavelength of the BPF and the wavelength resolution of my propose method is mainly limited to the diffraction glazing. Hence, my proposed method is 7 times better than the conventional method. The emission line derived from target and projectile materials is able to be identified in my proposed method. In the conventional method, it is not possible to estimate the temperature when the emission line spectrum is superposed. It means that plasma density cannot be obtained.

Compared to the conventional method, it has higher wavelength resolution and higher number of sampling points, so it was possible to properly identify the emission line spectrum. My proposed method is verified to be a more accurate temperature measurement.

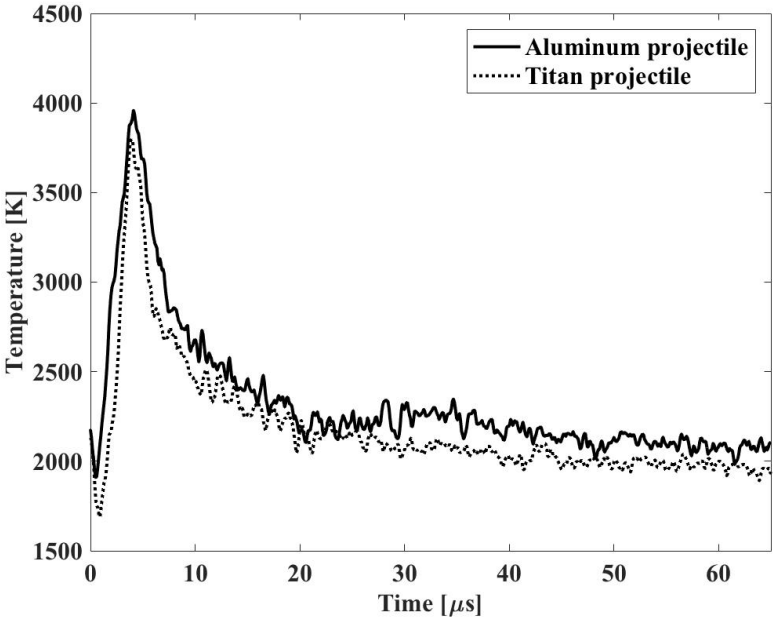

(A) In case of the aluminum target

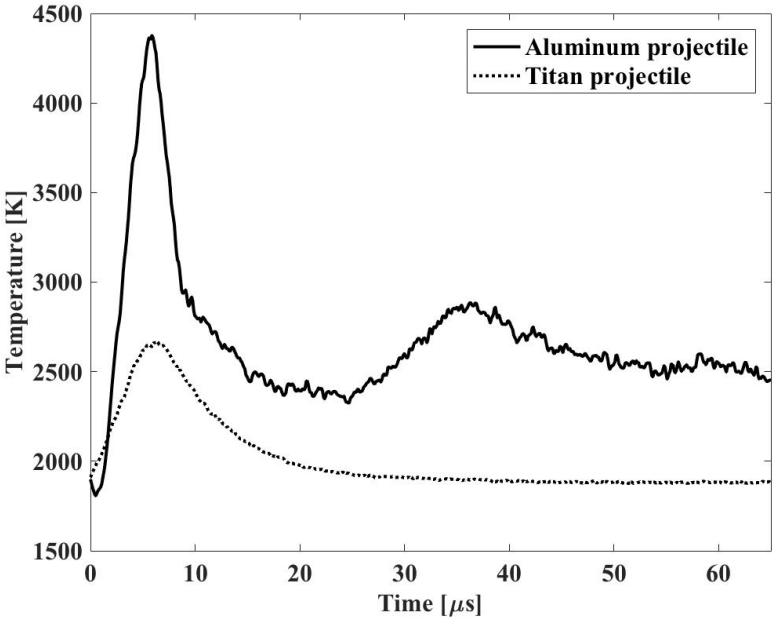

(B) In case of the copper target

FIGURE 2.19: Comparison of temperature in case of the different target

TABLE 2.3: The comparison between the conventional method and my proposed method.

Item	The conventional method	My proposed method
Wavelength resolution	40nm	5.7nm
Sampling points	3	1344
Identification of emission line	Not possible	Possible

2.6 Comparison of Temporal Change of Photon Number in Emission Line Spectrum

2.6.1 Identification of Emission Line Spectrum by Collision of Projectile and Target with Same Material

Before comparing the line spetrum derived from different target and projectile materials, the impact experiment between the same aluminum target and projectile material was conducted.

Figure 2.20 shows a photo of the crater after impact. The crater with 16 mm in diameter and 639 mm^3 in volume is created on the surface of the target. Because the impact energy of aluminum projectile is smaller than that of nylon projectile by five times, it results in a difference in the size of the crater.

Figure 2.21 shows the time-resolved spectrum. The horizontal axis indicates the observed wavelength, and the vertical axis indicates the time. The color bar indicates the number of photons. Until 3 μs, the number of photons rapidly increases, and then it decreases.

In Fig. 2.22, the spectrum of each time was integrated to identify the emission line spectrum according to the procedure of Fig. 2.9. Three wavelengths of 586.8 nm (AlII), 766.0 nm (AlIII), and 788.3 nm (AlIII) were observed and identified as emission line spectra derived from aluminum elements.

Thus, it was possible to identify the emission line spectrum of aluminum element by conducting an impact experiment with the same aluminum target and the projectile material.

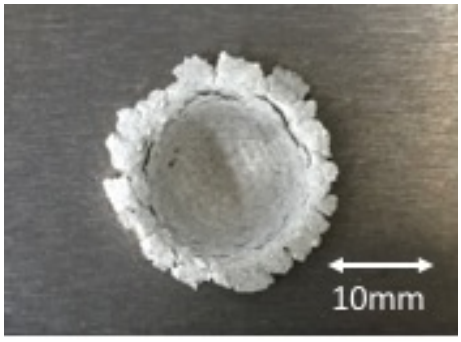

FIGURE 2.20: A photo of the crater on the aluminum target from an impact of aluminum projectile.

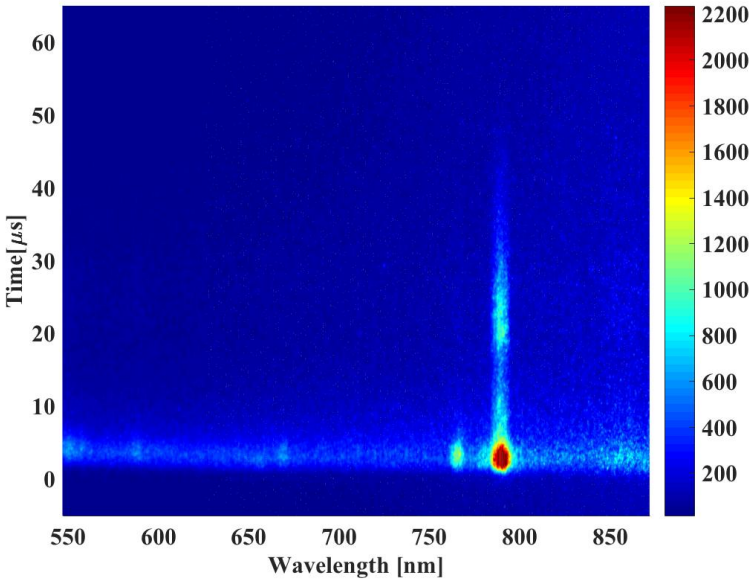

FIGURE 2.21: The time-resolved spectrum from an impact between the same aluminum target and projectile.

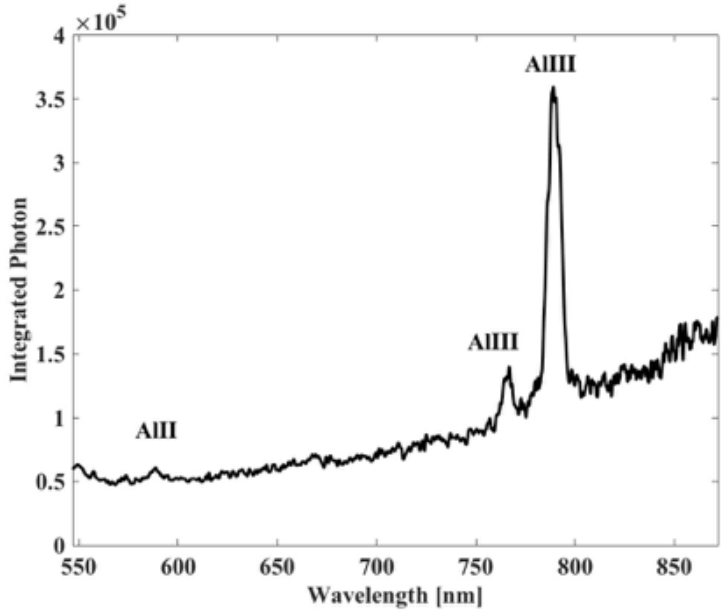

FIGURE 2.22: The integration of time-resolved spectrum from an impact between the same aluminum target and projectile.

2.6.2 Comparison of Temporal Change of Emission Line Spectrum from Impacts of Different Targets and Projectile Materials

By comparing line spectrum derived from different target and projectile materials, the composition of the plasma was investigated. First of all, I conducted the impact experiment between the aluminum target and titanium projectile. In addition to the three wavelengths of aluminum of 586.8 nm, 766.0 nm, and 788.3 nm specified in previous subsection, titanium element at two wavelengths of 625.1 nm (Ti II) and 862.3 nm (Ti I) were identified.

Figure 2.23 shows the temporal change of the number of photons observed at each wavelength. The rise time of the photons at 586.8 nm, 766.0 nm, and 788.3 nm derived from aluminum is 2 μs. The rise time of the photon numbers at 625.1 nm and 862.3 nm, which are derived from the titanium element, is also 2 μs. When the rise times of the line spectrum derived from the aluminum and the titanium elements were compared, the rise time of aluminum element and titanium element is the same of 2 μs. It is clear that the luminous vapor cloud generates immediately after the collision and includes a mixed gas with aluminum and titanium elements.

Comparing the intensity derived from aluminum and titanium, the FWHM for aluminum is 6 μs at 788.3 nm, and the FWHM for titanium is 3 μs at 625.1 nm. It was found that the line spectrum derived from the aluminum element has a longer observation time. This is because the crater volume (1655 mm^3) of the target surface generated by the impact is larger than the volume of the projectile (17.2 mm^3). Therefore, I suggest that it was observed for a relatively long time because the amount of vaporization from the target material in the observation field was larger than that from the projectile material.

Sencond, I conducted the impact experiment between copper target and aluminum projectile. I identidied that the three line spectrum of aluminum element identified in previous subsection and six line spectrum derived from copper elements at 573.2 nm (Cu I), 585.9 nm (Cu II), 622.4 nm (CuII), 655.5 nm (CuII), 703.7 nm (CuII), and 809.9 nm (CuII).

Figure 2.24 shows the temporal change of the number of photons in the observed emission line spectrum. Here, line spectrum at 586.8 nm of aluminum element and 589.0 nm of copper element are too close to be distinguished due to the wavelength resolution. In the case of 622.4 nm, 655.6 nm, and 703.7 nm, the intensities of the emission line spectrum are smaller than ones of the continuous spectrum, so the temporal change at their wavelengths are excluded. The rise time of the intensity of aluminum element are 4 μs and 5 μs, respectively. The rise time of copper element are 4 μs and 5 μs, respectively. When the rise time of aluminum and copper elements was compared, it was the same rise time. It was found that the mixed gas of the projectile material from the target has occurred.

In this way, it was clarified that a mix gas derived from the target and projectile materials is generated by comparing the temporal change of the emission line spectrum derived from the projectile and the target materials.

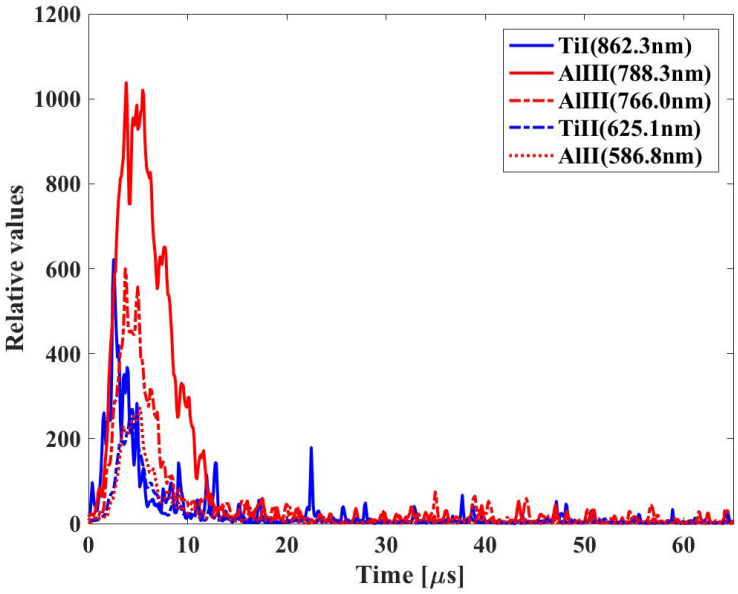

FIGURE 2.23: The comparison of temporal change of emission line derived from an impact between aluminum target and titan projectile

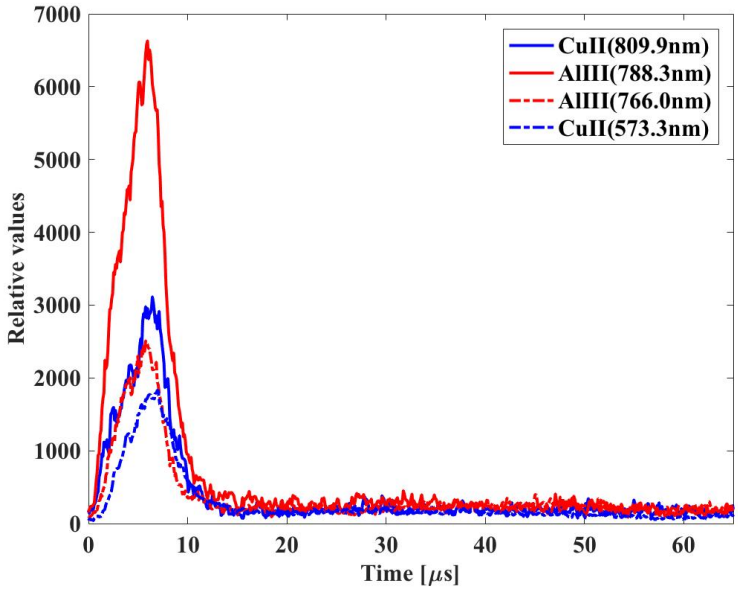

FIGURE 2.24: The comparison of temporal change of emission line derived from an impact between copper target and aluminum projectile.

2.7 Estimation of Plasma Density Caused by Impacts between Different Projectiles and Target Materials

Using the achievements obtained in Sections 2.5 and 2.6, plasma density caused by impacts between different projectiles and target materials is calculated. Plasma density N_e is expressed by the Equ. 2.2

$$N_e = \left(\frac{I_p}{0.61eS\left(\frac{kT_e}{\overline{m_i}}\right)^{1/2}} \right) \tag{2.2}$$

with $\overline{m_i}$, k, e, and S are the mean ion mass, Boltzmann constant, elementary charge, and probe surface area, respectively (Johnson and Malter, 1950). Temperature of luminous vapor cloud which is described in Section 2.5, is equivalent to T_e when it is assumed that the luminous vapor cloud is in thermal equivalent. The maximum I_p and the time is summarized in Tab. 2.4. The distance at each channel is between the electrodes and the impact point. Because impact plasma diffuses spatially, plasma current is smaller as the distance is further.

Regarding ion mass, it is necessary to determine the ion mass taking into account both the target and the projectile material, since both materials are generated in a composed state. Therefore, the mean ion mass $\overline{m_i}$ was calculated by weighting the ratio of the mass of the projectile M_p and the mass of the crater portion of the target material M_t, assuming that all the crater portion of the projectile and target material was vaporized. Also, the target material and the projectile material have different ionization energies. In addition to the ratio of ion mass, $\overline{m_i}$ was calculated considering the ratio of ionization energy. The equations are given by the following equations,

$$\overline{m_i} = m_t \times \alpha \times \beta + m_p \times (1 - \alpha \times \beta) \tag{2.3}$$

$$\alpha = \frac{M_t}{M_t + M_p} \tag{2.4}$$

$$\beta = \frac{i_p}{i_t + i_p} \tag{2.5}$$

where, m_t, m_p, M_t, M_p, i_t, i_p, α, and β are the ion mass of target material, the ion mass of projectile material, the mass of crater of the target, the mass of projectile, the ionization energy of the target material, the ionization energy of the projectile material, the ratio of weight, and the ratio of ionization energy, respectively. $\overline{m_i}$ of 6.14×10^{-26}kg was obtained by substituting the parameters in Tab. 2.5,.

Substituting the above parameters into the Equ. 2.2, plasma density N_e at each electrodes of 3.04×10^{11} cm^{-3} (Ch. 1), 6.18×10^{10} cm^{-3} (Ch. 2), and 3.14×10^{10} cm^{-3} (Ch. 3) could be obtained. The relationship between plasma density and the distance is plotted in Fig. 2.25. The approximation curve was

TABLE 2.4: Plasma current at each electrode

Channel	**Time [μs]**	I_p **[mA]**
Ch.1 (85 mm)	6.70	3.39
Ch.2 (115 mm)	8.61	0.69
Ch.4 (180 mm)	19.8	0.35

TABLE 2.5: Parameters for caluclating the mean ion mass

Parameters	**Aluminum (target)**	**Titan (projectile)**
Ion mass [kg]	4.48×10^{-26}	7.95×10^{-26}
Density [g/cm^3]	2.70	4.51
Volume [mm^3]	1655.4 (crater)	17.2 (projectile)
Mass [g]	4.47	0.07
Ionization energy [eV]	5.99	6.82

calculated by the least square method. It was found that plasma density decays as the cube of distance. The plasma density of the impact plasma could be calculated from the plasma current and plasma temperature obtained by double probe measurement and the ion mass constituting the impact plasma.

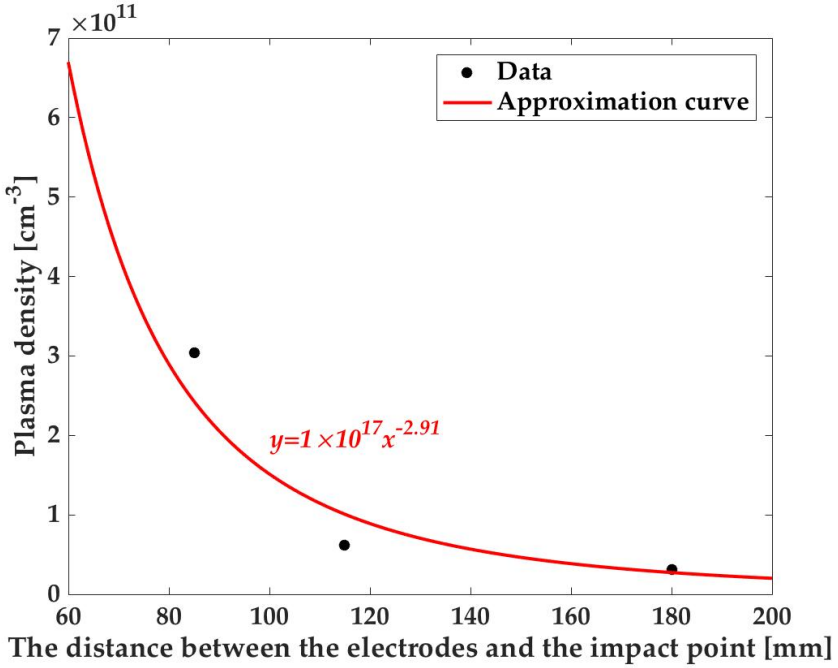

FIGURE 2.25: The relationship between plasma density and the distance

2.8 Summary

Hypervlelocity impact experiments were performed using the LGG, and the generation of the ejector related to high-temperature gas and impact plasma was investigated.

Spectroscopy is used to calculate the plasma temperature. In past studies, the method for calculating the temperature of plasma temperature was calculated from the intensity ratio measured by a photodiode with an interference filter at several specific points (Kadono, 1996)(Nagaoka, 2013). In addition, there was a problem that the temperature could not be calculated when the emission line spectra from the projectile and the target material were observed at those wavelengths.

However, by using the streak camera spectroscopy (wavelength Range: 547 to 872 nm, the number of measurement points is 1344 points), the emission line spectrum and the continuous spectrum can be distinguished by the high wavelength resolution and the high sampling points, and the method to obtain a more accurate plasma temperature could be proposed.

In addition, by examining the change in the number of photons in the emission line spectrum when different materials collided, it was clarified that plasma was generated in which both the target and the projectile materials were formed. Using the weighted average ion mass of both the mass ratio and ionization ratio, it was possible to determine the ion mass considering both projectile and target materials.

From the above, this study showed a method for calculating the plasma density of the impact plasma generated during the collision of different materials. It is expected that the plasma density of the impact plasma can be measured, and the risk of discharge on the spacecraft can be more accurately evaluated.

Chapter 3

Re-examination of Sustained Discharge of Satellite's Power Harness from Space Debris Impact

3.1 Introduction

The damage effects that typical susbsystems of spacecraft might experience are investigated (IADC-08-03, 2013). Although some subsystems such as honeycomb panels, pressure vessels or tanks may be affected by mechanical failure, subsystems of solar panels and power harness are affected by not only mechanical failure but electrical one. The mechanical failure and the effects of solar panel and power harness is described (A. Moussi, 2005; Nahra, 1989; Thomas W. Kerslake, 2003; Joel E. Willianmsen, 2015).

The effect of electrical damage on solar arrays has been well-studied given their large area (Akahoshi et al., 2008; Fukushige et al., 2008; S. Tagami, 2017),. The impact-induced plasma leads to arcing between the solar cells or between a cell and substrate on the solar array. At worst, Joule heating from the discharge carbonizes an insulation layer and creates a permanent short-circuit path. This is called permanent sustained discharge (PSD). Past studies have suggested that the risk resulting in PSD would occur due to impacts of a projectile less than a few millimeters in diameter.

The effect of electrical damage on the bundle of an artificial satellite's wire harness from a debris particle also has a risk. The sustained arc between the primary power cables of a satellite was investigated by Kawakita et al. (Kawakita et al., 2009; Kawakita et al., 2004). (R. Putzar, 2008)

Kawakita et al. have examined this phenomenon in the past, and confirmed that a ground fault can occur due to discharge via collision-excited plasma in a debris collision with a diameter of 0.2 mm or less. In response, the JAXA spacecraft design standard recommends protection measures against debris impacts with a diameter of 0.2 mm or more for the power harness (Requirement, 2014). However, the frequency of debris impact with 0.2 mm or more in diameter on power harnesses of the artificial satellites in a low Earth orbit by the simulation of debris environment model is larger than the frequency of ground faults of the actual artificial satellites. There is a deviation from the actual phenomenon.

In experiments conducted in the past, impact experiments were performed on the power harness while the power is supplying, and the discharge was

easily sustained because the internal resistance of the satellite may not be simulated. Moreover, multiple projectiles were impacted at the same time, and impact-excited plasmas interfered with each other if the impact points are close because the equipment of the gun could not inject a single particle in those times. This may be a factor that could not be evaluated accurately.

Therefore, my purpose is to re-examine the PSD of satellite's power harness from hypervelocity impacts in Chapter 4. Hypervelocity impact experiments were carried out and I verified two points: effects on single and multiple collisions, and effect on presence or absence of the load circuit.

3.2 Experimental Setups

Hypervelocity impact experiments were conducted using the LGG. Figure 3.1 shows the experimental setups. The gun is connected to a metal chamber and the specimen is set inside the chamber. Stainless steel and aluminum oxide projectiles measuring less than 1mm in diameter were accelerated up to 7.16 km/s. Aluminum oxide is thought to be typical materials of small space debris particles ejected by solid roket motors. The air pressure of a target chamber was evacuated to 1-10 Pa (mean free path: 0.7-6.7 mm). Outside the chamber, there are experimental devices such as power sources, a load circuit, an oscilloscope, and a data logger. The specification of experimental devices are shown in Appendix A. Figure 3.2 shows a photo of the power harness specimen. The specimen consists of the power harness and an A2024 substrate plate with 3 mm in thickness to simulate the single line of the power harness behind the SAP and three-layered power harness at the boom of the SAP. For the power harness, we selected the SPEC 55 ® wire of TE connectivity (single wall, AWG22) that is commonly used for Japanese spacecraft.

The double probe was used to measure plasma density. The plasma current was measured by five arrays of double probes positioned by 1 cm in range of 1 - 5 cm from the impact site. The distance between the plasma electrode and the harness face is approximately 1 cm. The applied voltage is 9.6 V and the detection resistance of 10 kΩ except for 1.5 kΩ of the probe where is the closest to the impact site.

Figure 3.3 shows two kinds of circuit configurations used for different purposes. For both types, a three-layered power harness is connected and the voltage and current are supplied by two solar array simulators. In the the solar array simulator of SAS1, the rated power output, the rated voltage, and the rated current are 600 W, 120V, and 5A, respectively. In the the solar array simulator of SAS2, the rated power output, the rated voltage, and the rated current are 480 W, 80V, and 6A, respectively. The applied voltage and current values were simulated in the spacecraft configuration in LEO and GEO. The current was adjusted by the variable resistance. For type 1, SAS1 is connected to the power harness bundle between the first and second layers with the circuit open. SAS2 is connected to the power harness bundle and the aluminum plate through bleeder resistance with the circuit also opened. For type 2, the load circuit with variable resistance and capacitance were added to simulate load resistance of the satellite bus power. The experimental condition is shown

in Tab. 3.1 and Tab. 3.2. Table 3.1 shows the experimental condition without a load cirucuit of Type 1 which is described in Fig. 3.3a. Table 3.2 shows the experimental condition with a load circuit which is described in Fig. 3.3b.

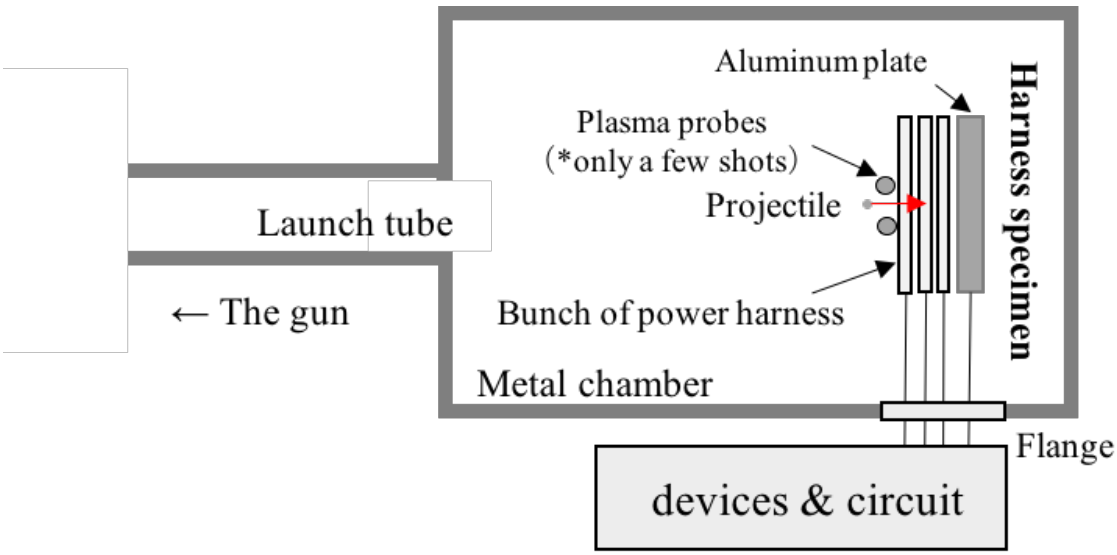

FIGURE 3.1: Experimental setups.

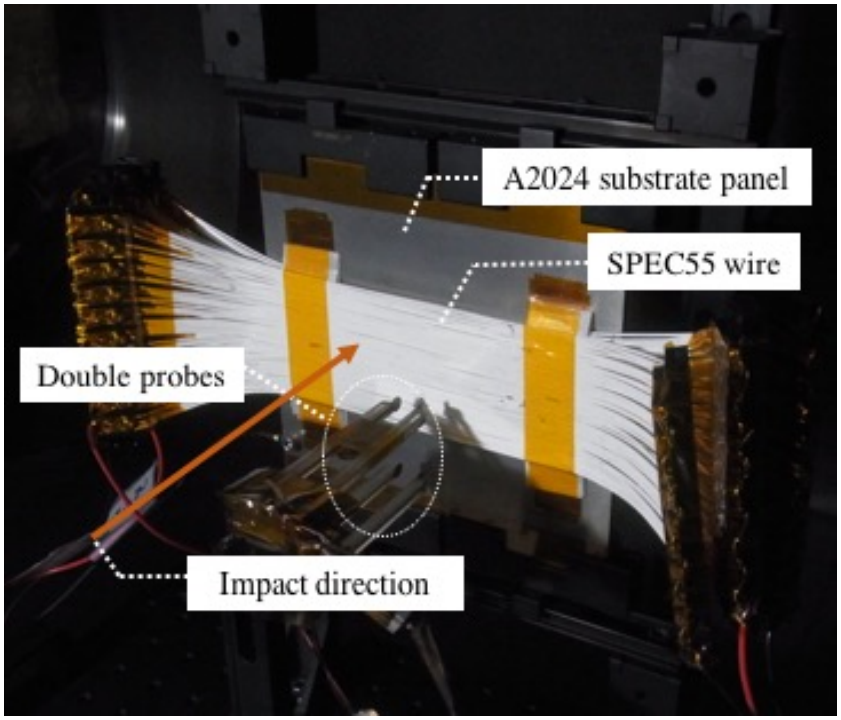

FIGURE 3.2: Picture of harness specimen.

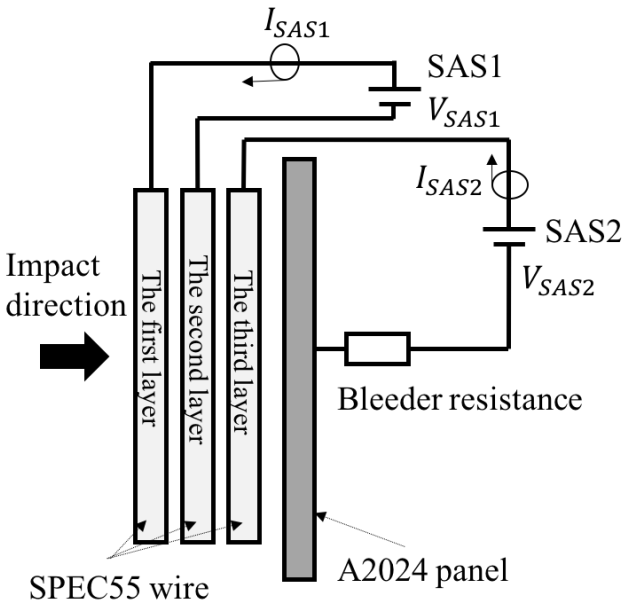

(A) The conventional circuit configuration

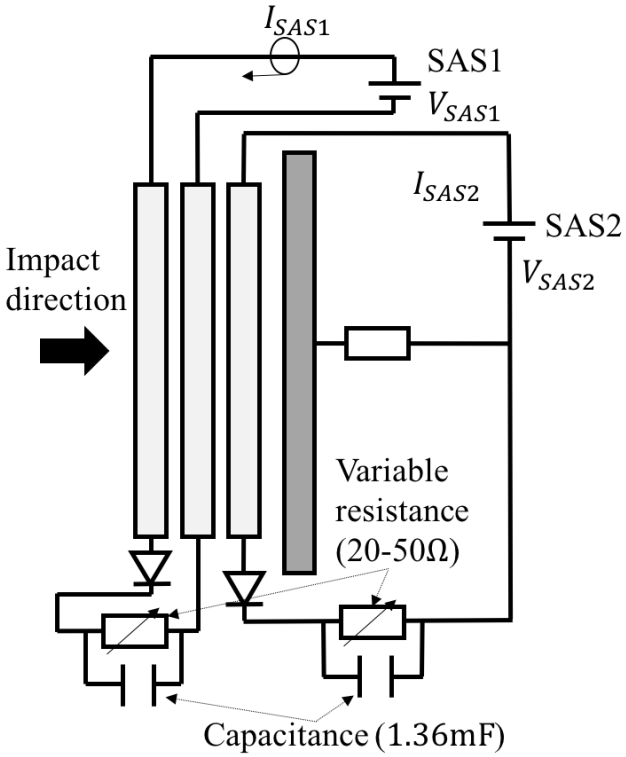

(B) The circuit configuration with a load circuit

FIGURE 3.3: The two kinds of circuit configurations

TABLE 3.1: The experimental condition of Type1.

Shot ID	Projectile	Diameter[mm]	Impact number	Velocity [km/s]	Source current [A]	Source voltage [V]
#170905-7	SUS304	0.3	15	3.85	3.0/3.0	100/80
#170906-2	SUS304	0.3	6	3.82	3.0/3.0	100/80
#170906-1	SUS304	0.3	3	3.88	3.0/3.0	100/80
#171017-1	SUS304	1.0	3	4.12	3.0/3.0	100/80
#170906-3	SUS304	0.3	1	4.16	3.0/3.0	100/80
#170907-1	SUS304	0.5	1	4.25	3.0/3.0	100/80
#171016-3	SUS304	0.3	1	6.87	3.0/3.0	100/80
#171016-2	SUS304	0.8	1	6.95	3.0/3.0	100/80
#171016-1	SUS304	1.0	1	7.03	3.0/3.0	100/80
#171016-4	SUS304	0.5	1	7.07	3.0/3.0	100/80
#170906-5	SUS304	0.3	1	7.07	3.0/3.0	100/80
#171016-6	Alumina	0.3	1	7.16	3.0/3.0	100/80
#171013-1	SUS304	0.5	1	7.17	3.0/3.0	100/80
#171017-2	SUS304	0.5	1	7.10	5.5/5.5	50/50

TABLE 3.2: The experimental condition of Type2.

Shot ID	Projectile	Diameter[mm]	Impact number	Velocity [km/s]	Source current [A]	Source voltage [V]
#160628-1	Alumina	1.2	1	6.94	2.0	50
#160627-3	Alumina	0.5	1	6.70	2.0	50
#160627-4	Alumina	0.3	1	6.89	2.0	50
#170627-4	SUS304	0.3	6	4.01	3.0/3.0	100/80
#170627-3	SUS304	0.3	1	4.11	3.0/3.0	100/80
#170627-1	SUS304	0.3	1	4.12	3.0/3.0	100/80
#170907-5	SUS304	0.3	20	6.80	3.0/3.0	100/80
#170907-4	SUS304	0.3	1	6.84	3.0/3.0	100/80
#171017-4	SUS304	0.3	1	7.16	3.0/3.0	100/80
#171017-5	SUS304	0.3	1	7.17	3.0/3.0	100/80
#170626-5	SUS304	0.3	1	4.06	5.5/5.5	50/50
#170626-7	SUS304	0.5	1	4.05	5.5/5.5	50/50
#170626-1	SUS304	0.3	1	4.09	5.5/5.5	50/50
#170626-4	SUS304	0.3	12	4.11	5.5/5.5	50/50
#170622-1	SUS304	0.3	1	4.11	5.5/5.5	50/50
#170623-1	SUS304	0.3	1	4.12	5.5/5.5	50/50
#171017-3	SUS304	0.5	1	7.17	5.5/5.5	50/50

3.3 The Difference between Impacts from a Single Particle and Multiple Particles

I compared with multiple particles impacts and single-particle impact with almost the same collision velocity. First, the experimental results by impacts of multiple particles are shown in Fig. 3.4. A large number of collision scars were confirmed on the surface of the power harness in Fig. 3.4a. It was confirmed that one of impact scar was a trace of carbonization and melting is seen on the surface of the power harness at a few of them. On the all layers, it was confirmed that the trace of carbonized and melted power harnesses.

Figure 3.4b shows the voltage and current waveforms before and after the collision of the power harness. It can be seen that, after the collision, the voltage suddenly decreases and the current rapidly increases. This is thought to be caused by a short circuit due to the start of discharge through the plasma between the collision marks due to particle collision with the power harness, and the film portion of the power harness being carbonized and melted. I found that the impedance between the discharge gap is approximately 11 Ω from the current and voltage. In this way, it was confirmed that when multiple particles of 15 particles with a diameter of 0.3 mm collide, the power harness is carbonized and melted as in the past research, causing a PSD as the same in the past studies.

Figure 3.5a shows the appearance of the power harness when particles with a diameter of 0.3 mm collide at a speed of 4.2 km/s. It has collided with the center part of the power harness, and it can be confirmed that the power harness is carbonized and melted. Figure 3.5b shows the waveforms of voltage and current. In the case of this shot, it is considered that the short circuit was formed by the voltage drop and the current rise due to the connection of the SUS1 circuit from the open state to the power harness.

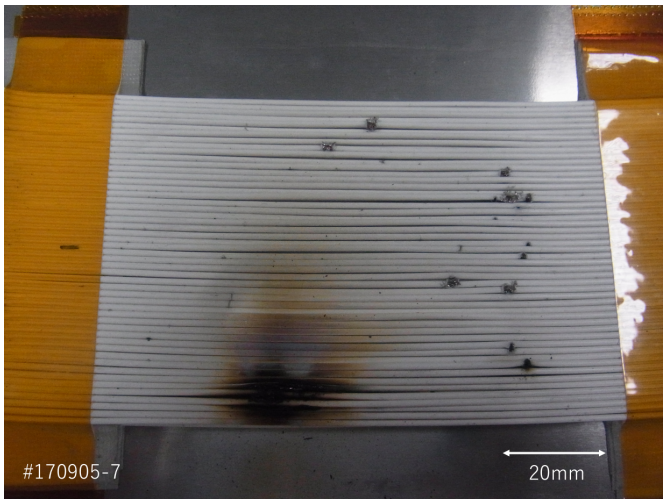

(A) On the surface of the layer

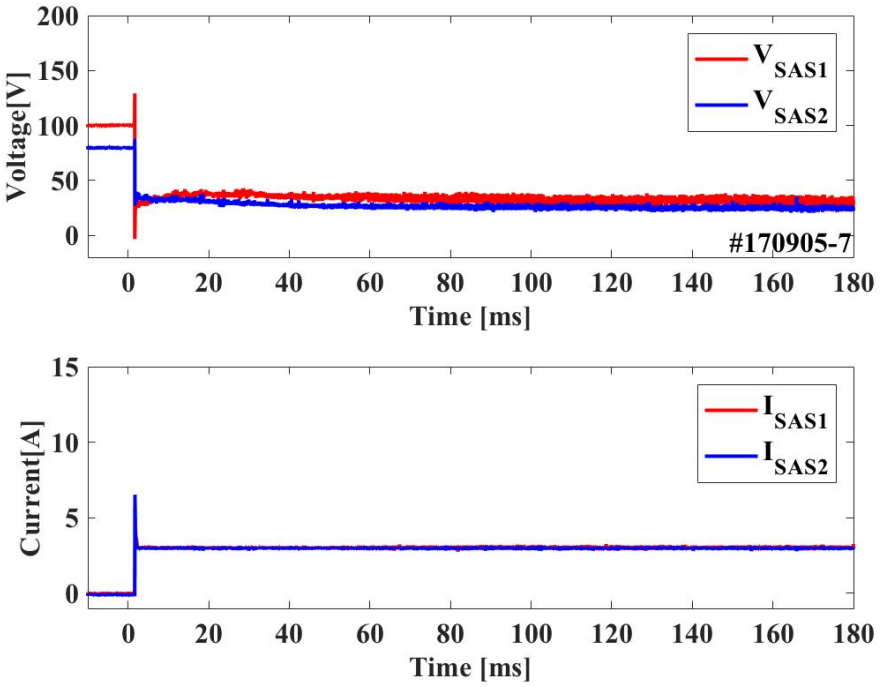

(B) Results of simltaneous measurements.

FIGURE 3.4: Photos of power harness appearance

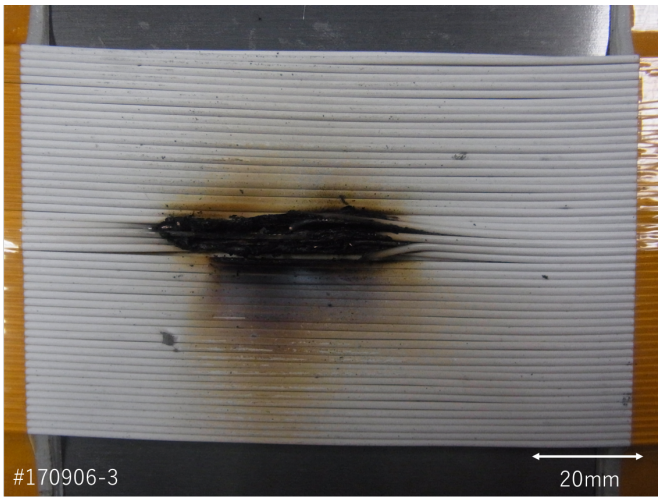

(A) A photo of a power harness specimen

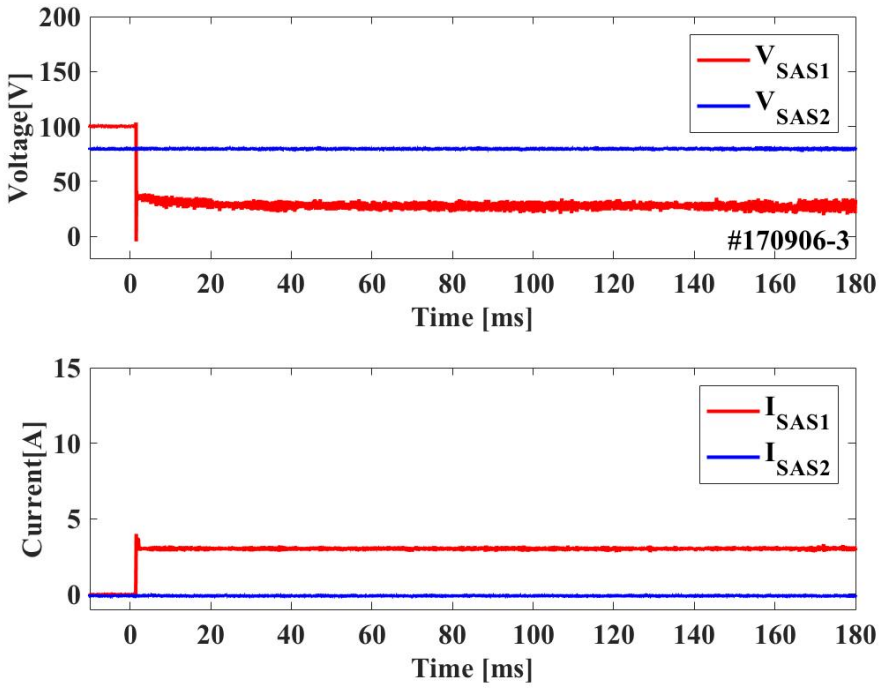

(B) Waveforms of voltage and current before and after impacts

FIGURE 3.5: Waveforms of voltage and current before and after impacts

3.4 Effect on Circuit Configuration with a Load Circuit

The effects of the presence or not with the load circuit were investigated. Figure 3.6a shows the appearance of the power harness when a single particle with a diameter of 0.3 mm is collided at a velocity of 6.84 km/s. The carbonized and melted power harnesses could not be confirmed.

Figure 3.6b shows the current and voltage waveforms before and after the impact. Instantaneous changes were seen during 6 μs, but no sustained voltage and current increases.

The influence of the PSD was investigated even when the power supply voltage and current of the satellite were 50V/5.5A of power condition. Figure 3.7a shows the appearance of the power harness when a single particle with a diameter of 0.3 mm is collided at a velocity of 7.16 km/s. The carbonized and melted power harnesses could not be confirmed.

Figure 3.6b shows the current and voltage waveforms before and after the impact. The changes in voltage and current value before and after impact could not be confirmed.

The impedance between the discharge gap and the load resistance are 11 Ω and 33 Ω respectively. In this case, it is suggested that the the PSD does not happen due to low impedance of the load resistance.

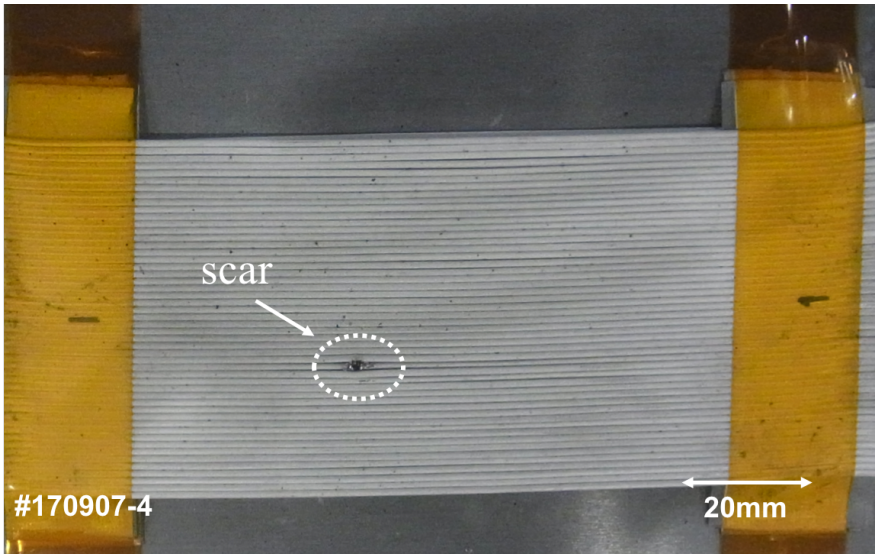

(A) A Photo of the harness specimen with a load circuit

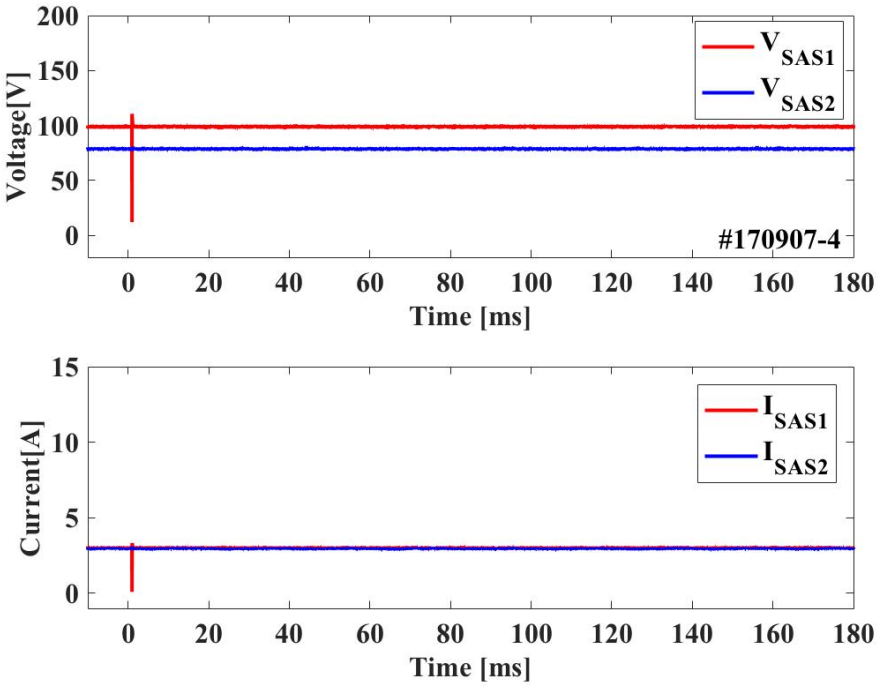

(B) Waveforms of voltage and current before and after a single particle impact

FIGURE 3.6: Results of impacts from single particle with a load circuit

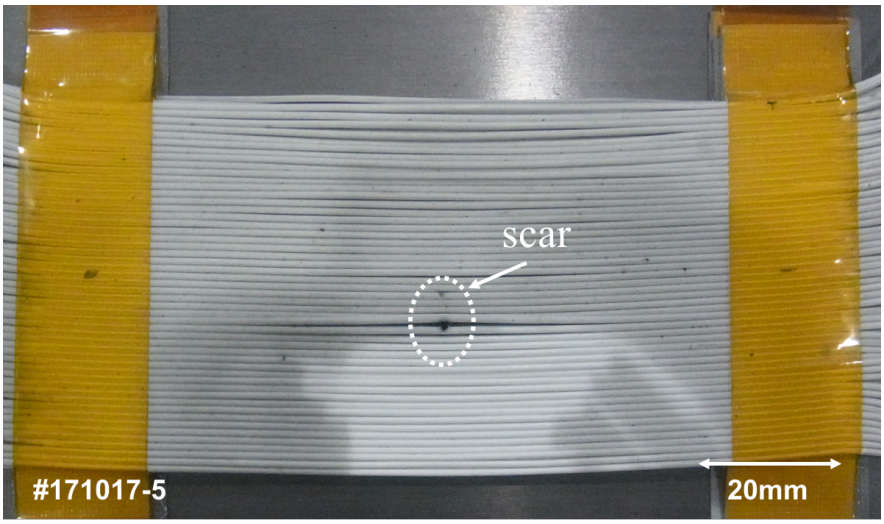

(A) A Photo of the harness specimen

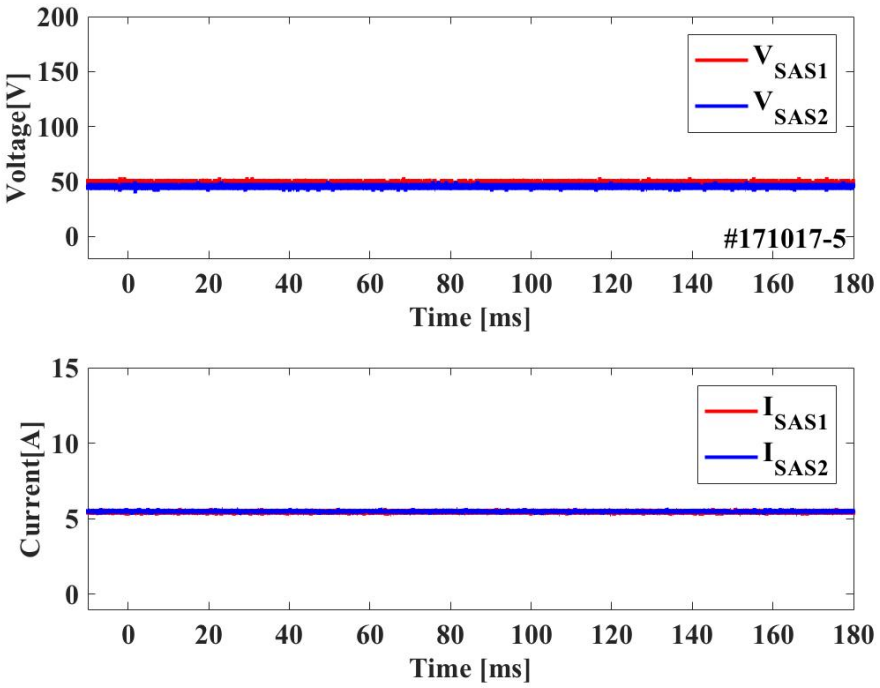

(B) Waveforms of voltage and current before and after impacts

FIGURE 3.7: Results of impacts from multiple particles

3.5 Interaction between Plasma Density and Discharge

The relationship between dishcarge and impact plasma was investigated. For the specimen, the load circuit of spacecraft was simulated. The projectile made of aluminum oxide with a diameter of 0.3, 0.5, and 1.2 mm was impacted on the specimen at approximately 7 km/s. Figure 3.8 shows plasma current from a single perticle impact on the specimen with a load circuit. The plasma current at the nearer electrodes from a impact site usually indicates the higher plasma current.

Table 3.3 shows the summary of the impact condition and the measurement results. The plasma density is estimated by the current of double probes with an assumption of ion mass and electron temperature based on achievements of Chapter 2. According to the observation of the damaged area, I assume that the ion mass are calculated by the material of projectile (aluminum), and harness core (copper). The electron temperare is assumed to be 3000 K. It was found that plasma density depends on impact energy. The high dense of impact plasma has dozens of microseconds, and the duration of impact plasma is much shorter than the duration of PSD. Thus, it is suggested that impact plasma triggers the PSD.

TABLE 3.3: Impact condition and measurement results.

Diameter [mm]	Velocity [km/s]	Discharge duration [ms]	N_e [cm^{-3}]
1.2	6.94	0.11	3.2×10^{12}
0.5	6.70	1.00	1.9×10^{12}
0.3	6.89	3.63	2.1×10^{11}

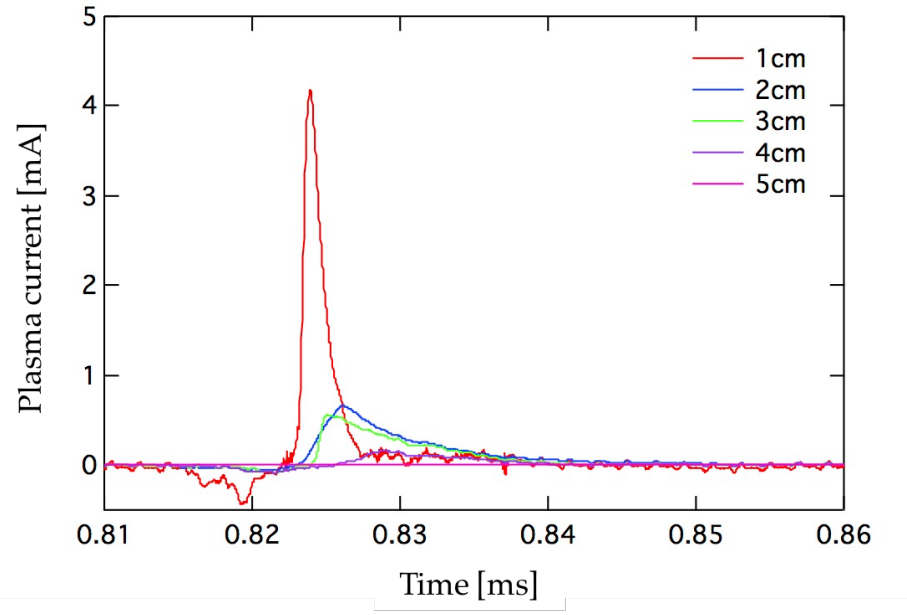

FIGURE 3.8: Plasma current from a single particle impact on specimen with a load circuit

3.6 Summary

We conducted the hypervelocity impact experiments using the LGG to clarify the past issues. First, the effects of multiple particles impacts and a single particle impact are investigated. The reproducibility with past research in multiple collisions was confirmed, and the power harness was carbonized and PSD lead even when a single particle impacts. Also, it is found that impact plasma may trigger primary discharge between power harness, because the impact plasma was totally dissipated within 0.1 ms, which is much shorter than the recorded discharge duration.

Second, the two kinds of circuit configurations were compared to investigate whether a load circuit affects the occurrence of PSD. In the case of the circuit configuration with the load circuit, the carbonized power harness could not be confirmed. Also, even when instantaneous changes were seen, but no sustained voltage and current increases. I suggested that it was considered that the current flows through the circuit with the load resistance and the carbonization and PSD of the harness did not occur, because the load resistance was smaller than the resistance between the harnesses.

Finally, previous studies have proposed that sustained discharge occurs when particles of 0.2 mm or more collide, but this was a condition that was likely to occur because the load circuit was not simulated. The results were applied to the current satellite design standards. However, it may be overly risk-assessed. I suggest that there is a possibility that excessive risk assessment is underway, and it is necessary to review it. Also, in order to prevent sustained discharge from the viewpoint of materials, it is also required to develop a cable that does not contain a carbon component.

Chapter 4

Microwave Emissions Phenomenon

4.1 Introduction

RF emission has been confirmed in laboratory studies. Reports on the detection of electrical vibrations of several hundred kHz from less than 1 g aluminum particles at a velocity of 10 km/s into hard materials in a vacuum chamber for the first time. (Bianchi et al., 1984). Crawford and Shultz detected magnetic fields generated due to impact plasma by using magnetic search coils from hypervelocity impact from aluminum sphere of 0.16 - 0.37 g in masses (David A. Crawford, 1993; David A. Crawford, 1999). Close et. al investigated the radiation from impact plasma generated by hypervelocity impacts (S. Close, 2010; S. Close, 2013). They conducted experiments using a Van de Graaff dust accelerator from micro particle sizes with masses between 10^{-16} and 10^{-11} g. Microwaves were measured by using patch antennas tuned to 315 MHz and 916 MHz and sensors of retarding potential analyzer or Faraday plate arrays were instrumented to measure the net current associated with the expanding impact plasma. They suggested that the plasma is ejected in lateral direction from the impact site. Due to their much lower mass, the electrons are ejected at much higher velocities than the ions. Thus, effectively a charge separation takes place. Ions and electrons can be seen as electric dipoles, oscillating with a frequency, the plasma frequency. Yet, microwave emission from micro particle impacts has not been detected, even though microwave phenomenon continues to radiate after impact plasma phenomenon.

Microwave emits in the GHz range (Takano et al., 2002). They conducted hypervelocity experiments using a LGG and a rail gun from a nylon cylinder with metal screw of 0.21 g at a velocity of 4 km/s. They detected microwave signals at 22 GHz using a heterodyne receiver, which generates intermittent frequency (IF) by mixing two signals of the lower frequency and the higher frequency. Also, microwave emissions emit intermittently for more than microseconds. The dependence of microwave emission on target materials and impact velocity was reported (K. Maki, 2005). They investigated how the target materials influence the microwave emissions using aluminum, alumina ceramic, red brick, and polyurethane rubber. Microwave signals were detected at 22 GHz and 2 GHz using heterodyne receivers from hypervelocity impacts on aluminum, copper, iron, niobium, and nickel plates (H. Ohnishi, 2007; H. Ohnishi, 2005). They suggested that electron excitation occurs due to thermal effects or bond dissociation on the target.

Although the microwave emissions from various kinds of target materials

were confirmed, it is difficult to discuss what physical parameters contribute to the radiation of electromagnetic waves. Also, it is required to compare with microwave emissions as well as other phenomena to clarify the characteristics or mechanism microwave emissions.

In the field of material engineering, RF emission from fracture of rock and other brittle materials was modeled (G. Martelli, 1985; Steven G. O'Keefe, 1995). However, they did not give a complete explanation, even though microwaves emit intermittently during milliseconds.

In this paper, hypervelocity impact experiments were conducted to clarify the mechanism of microwave emissions. The microwave emissions were investigated by measuring flash and impact plasma, in addition to microwave emissions simultaneously. Also, experiments were conducted by reducing the physical parameters as much as possible by using pure aluminum or an aluminum alloy with the target material as an aluminum material.

4.2 Experimental Setups for Measuring Simultaneous Measurements: Microwave, Plasma, and Luminous Vapor Cloud

In addition to the optical measurement described in Chapter 2, microwave emission was measured by placing a target in the acrylic vacuum chamber. Antennas were installed around the chamber and aimed at the collision point. The microwave signals received by antennas were recorded with an oscilloscope. The experimental setups for measuring the ejecta cloud are shown in Fig.4.1. In order to minimize the influence of microwave reflected from metal objects and an external noise as much as possible, radiofrequency absorbers were installed around the acrylic vacuum chamber.

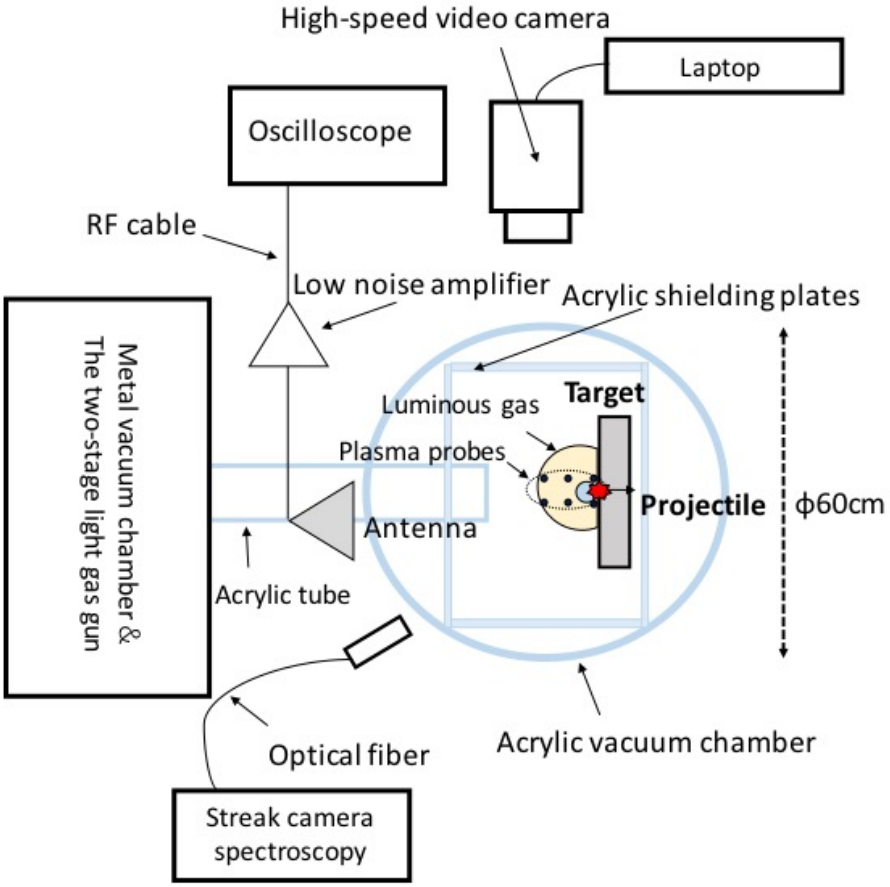

FIGURE 4.1: The configurations of experimental setups

4.3 Microwave Measurements

4.3.1 Microwave Receivers

Since the microwave signals include the broadband frequency components, it is suitable to use an antenna with a broadband frequency. Figure 4.2 shows photos of two kinds of log-periodic (LP) antennas in the experiments. The LP antenna is a member of a general class of frequency-independent antennas that rely on repetitive dimensions of their structures (Paul, 2006). The structural dimensions increase in proportion to the distance from the origin of the stracture. This results in the input impedance and radiation properties repeating periodically as the logarithm of frequency. Thus, they are said to be the broadband antennas. Of the two LP antennas, one is the photograph of the LP antenna with higher frequency bands with 850 - 6500 MHz as shown in Fig. 4.2a. The other is the photograph of the LP antenna with lower frequency bands with 400 - 1000 MHz as shown in Fig. 4.2b. The characteristics of LP antennas were measured and described in Appendix C.

The diagram of the microwave receiver is shown in Fig. 4.3. Because amplitudes of microwave signals are small, the low noise amplifiers (LNA) of 45 dB for the LP antenna with higher frequency bands and 46 dB for the LP antenna with lower frequency bands are inserted after the LP antennas. The oscilloscope with analog frequency bands from DC to 8000 MHz was selected in order to measure microwave signals directly. The specifications of experimental devices are shown in Appendix A.

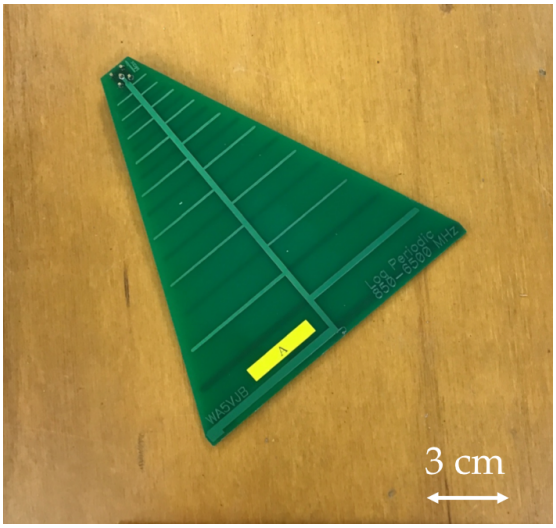

(A) The log-periodic antenna with higher frequency bands

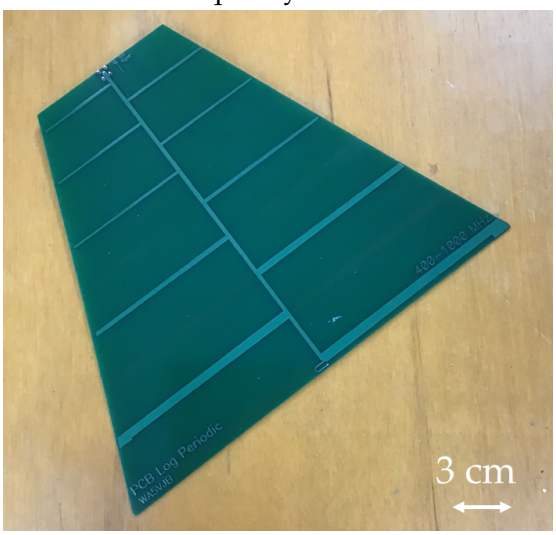

(B) The log-periodic antenna with lower frequency bands

FIGURE 4.2: Photos of two kinds of log-periodic antennas used in the experiments

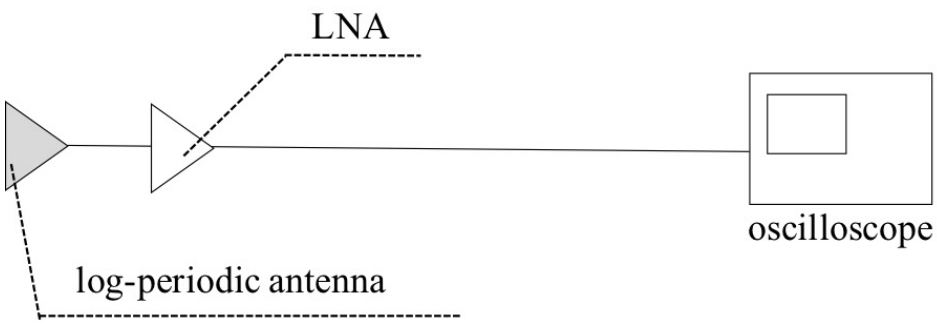

FIGURE 4.3: The block diagram of the microwave receiver

4.3.2 Characteristics of Receivers with Log-periodic Antenna

Figure 4.4 shows the block diagram for calibration. The LP antennas were replaced with a signal generator (SG). By sweeping the level of input power with a single frequency, the waveform was recorded on the oscilloscope. Figure 4.5 shows the typical waveform displayed on the oscilloscope. I define maximum voltage, minimum voltage, and the peak-to-peak voltage between maximum and minimum voltage of the sine waves as V_{max} , V_{min}, and V_{p-p}.

There are two types of receivers. One is the receiver with the LP antenna with higher frequency bands. Figure 4.6 indicates characteristics of the receiver. In the signal generator, characteristics of the receivers were measured when signals applied with three frequencies of 1500 MHz and 6000 MHz. Figure 4.6a indicates the dynamic range of the receiver. The horizontal axis indicates the input power of the SG and the vertical axis indicates the V_{p-p} recorded on the oscilloscope. It can be seen that the input signal is too small to be amplified when the input signal is below 10^{-6} mW. It can also be seen that the output voltage is saturated when the input signal exceeds 10^{-3} mW. Therefore, it was found that this receiver is a region that linearly changes in the region of approximately 10^{-6} mW to 10^{-3} mW, and corresponds to the dynamic range of the receiver.

Figure 4.6b shows the polarity characteristics of the receiver with higher frequency bands. The output voltage V_{o-p} means the absolute voltage of V_{max} as positive polarity and V_{min} as negative polarity. When the input signal with 6000 MHz is applied, the positive and negative polarity are almost equal. Yet, the positive and negative polarity seem to be different when the input signal with 1500 MHz is applied. Therefore, it has found that the polarity characteristics of the receiver at lower frequency range has an asymmetry characteristics.

The other is the receiver with the LP antenna with lower frequency bands. Figure 4.7 shows characteristics of the receiver with the lower frequency bands. In the signal generator, characteristics of the receivers were measured when signals applied with three frequencies of 400 MHz, 700 MHz, and 1000 MHz. Figure 4.7a shows the dynamic range of the receiver. It can be seen that the input signal is too small to be amplified when the input signal is below 10^{-4} mW. It can also be seen that the input signal exceeds 1 mW is too large to amplify. Also, the amplitude at 1000 MHz is lower than one at 400 MHz and 700 MHz because of the frequency response of the LNA. Therefore, it was found that this receiver is a region that linearly changes in the region of approximately 10^{-4} mW to 1 mW, and corresponds to the dynamic range of the receiver.

Figure 4.7b shows the polarity characteristics of the receiver with higher frequency bands. When the input signals with 700 MHz and 1000 MHz are applied, the positive and negative polarities are almost equal. Yet, the positive and negative polarities seem to be different when the input signal with 400 MHz is applied. Therefore, it has found that the polarity characteristics of the receiver at lower frequency range have an asymmetry characteristics.

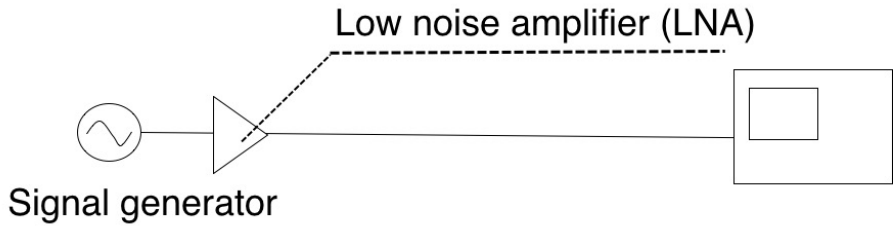

FIGURE 4.4: The block diagram for Calibration

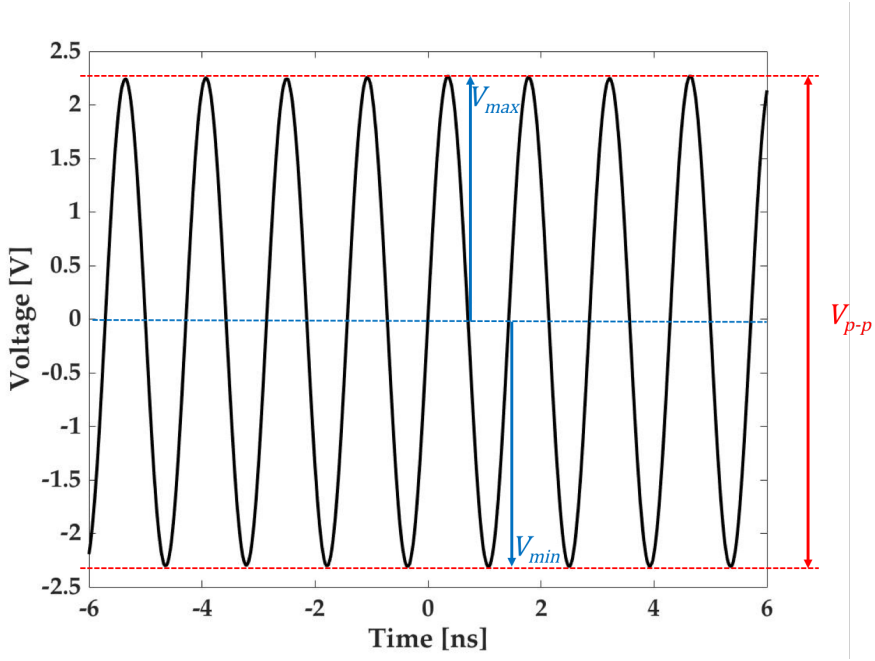

FIGURE 4.5: The typical waveform shown on the oscilloscope

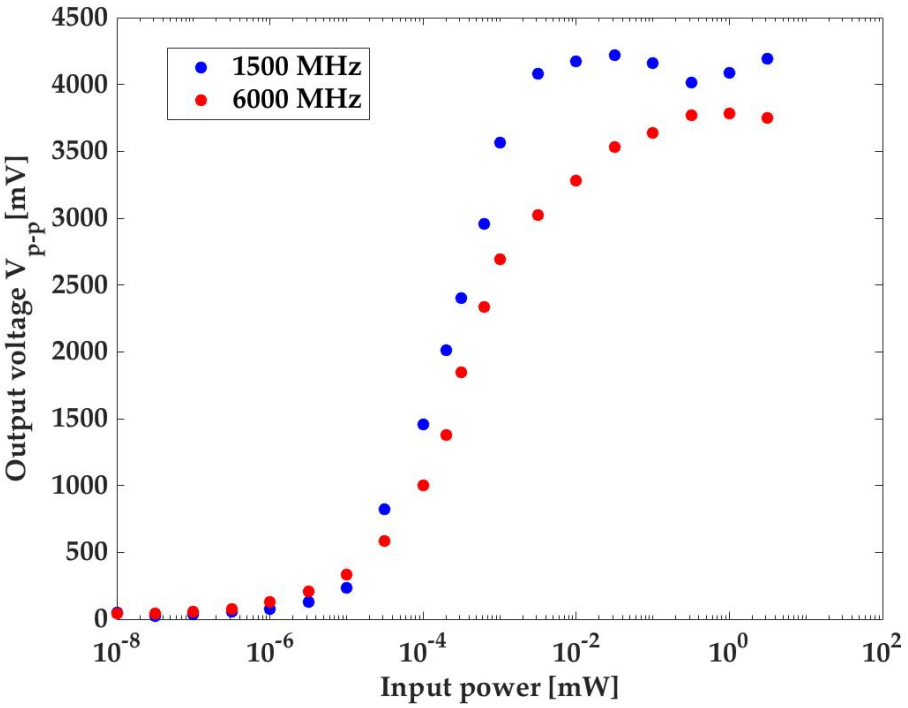

(A) The dynamic range of the receiver with higher frequency bands

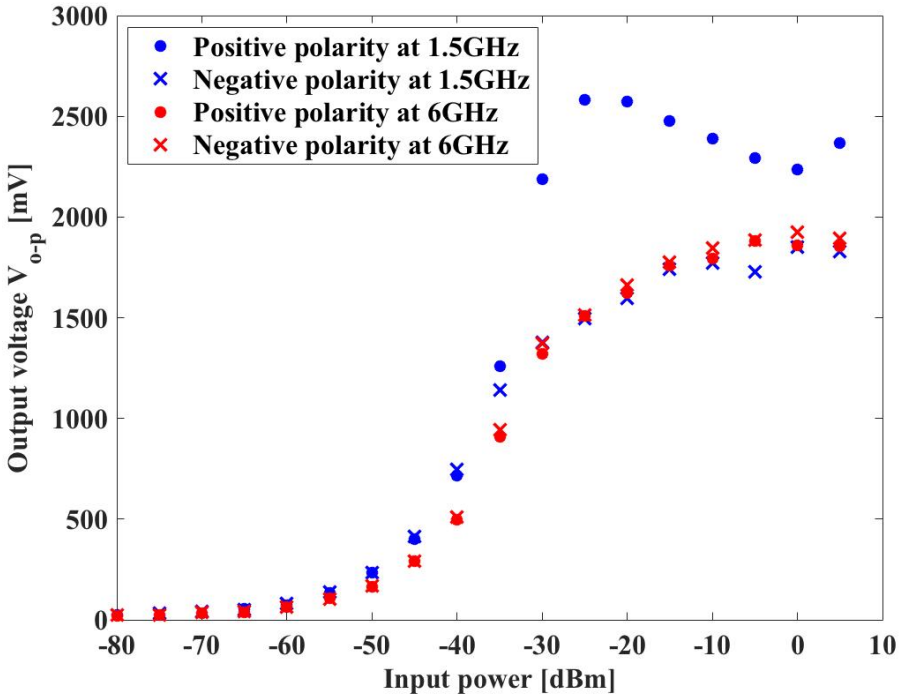

(B) The polarity characteristcs of the receiver with higher frequency bands

FIGURE 4.6: Characteristics of the receiver with the LP antenna with higher frequency bands

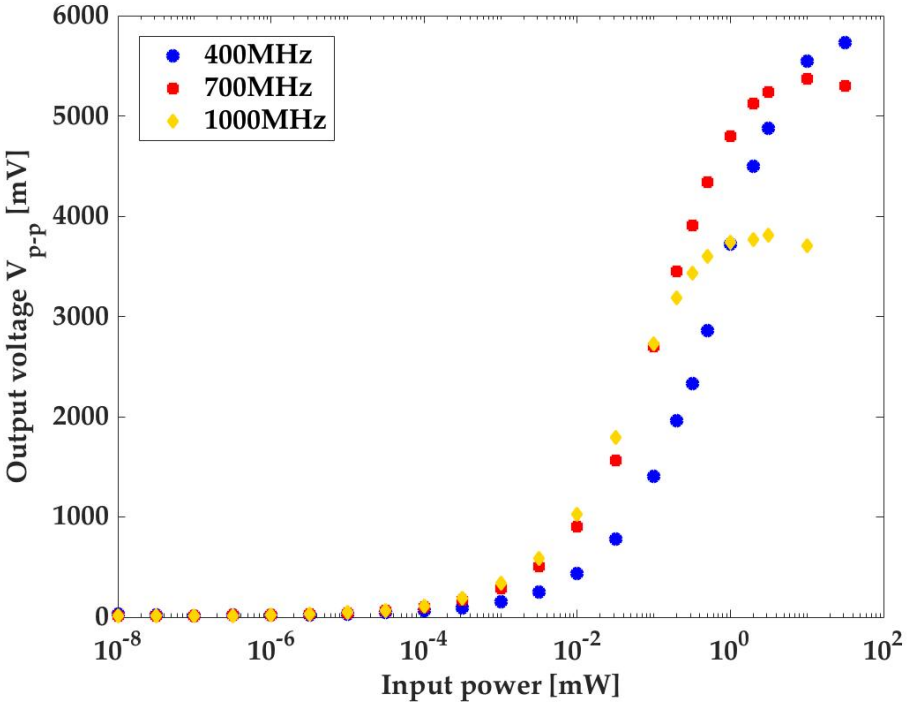

(A) The dynamic range of the receiver with the lower frequency bands

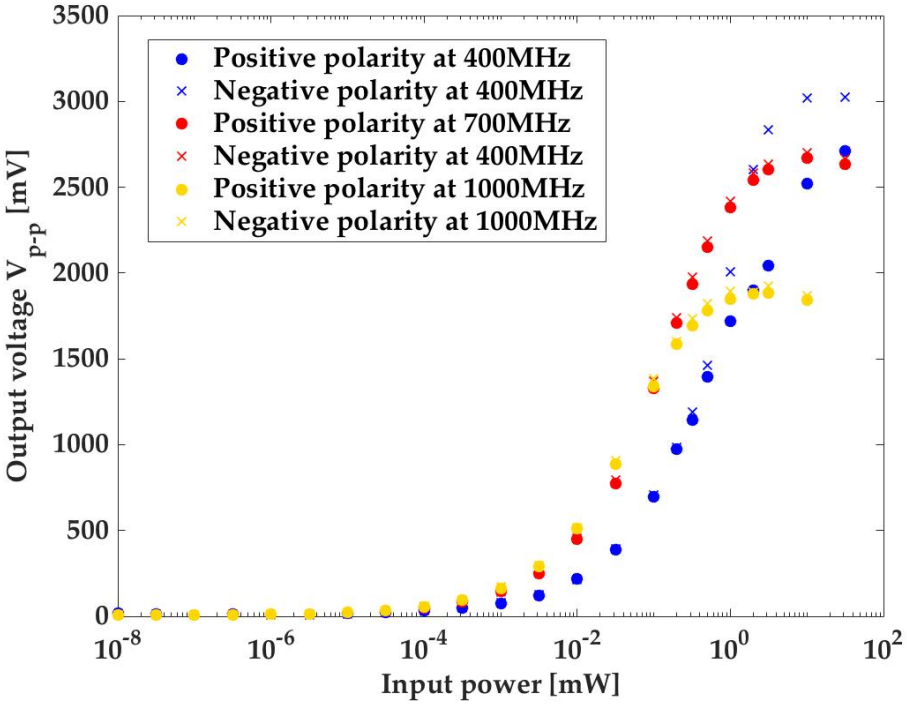

(B) The polarity characteristcs of the receiver with the lower frequency bands

FIGURE 4.7: Characteristics of the receiver with the lower frequency bands

4.4 Electromagnetic Interference at Experimental Environment

It is important to understand the electromagnetic interference (EMI) environment in RF measurement. The experiments are performed by using the LGG, so it is difficult to perform an experiment without a noisy environment such as an anechoic chamber. Therefore, I investigated the external noise. The typical waveform of noise is shown in Fig. 4.8. The maximum and minimum voltages are -214.1 mV and 217.7 mV, respectively.

First, regarding the LGG devices, an igniter is used to ignite gunpowder in the first-stage gunpowder chamber. There is a considerable time difference from the ignition until the projectile collides with the target. Moreover, although measurement has been started with an oscilloscope from several hundreds of microseconds before the impact, microwave emission has not been observed so far. Hence, it is considered that there is no microwave emission due to the LGG devices.

Next, in the experiment, plasma and spectroscopic measurements were performed simultaneously, in addition to microwave measurement. In spectroscopic measurement, a streak camera spectroscopy is used. When the streak camera spectroscopy works, a high voltage is applied for a sweep voltage. A streak camera spectroscopy was measured in the same measurement environment for the presence or absence of microwave emission from a high voltage. Yet, there is no microwave emission. Thus, there is no microwave emission from any device in the experimental facility.

Finally, microwave band is widely used in communication devices such as mobile phones, smartphones, PHS, Wi-Fi, and etc. There is a possibility of receiving microwave (communication noise) transmitted from them. Communication noise was received in a measurement environment. Figure 4.9a shows the communication noise measured by the receiver with the LP antenna. In general, microwaves from communication noise are different from microwave generated by impact in a carrier wave that has been modulated with a considerably long period compared to microwave emission generated by impacts. Also, the frequency components of external noise is shown in Fig. 4.9b. The frequency component is calculated by using the fast Fourier transform (J. W. Cooley, 1965). The frequency component at 1.9 GHz is much stronger than the other frequency components. I identified the signals from dynamic host configuration protocol (DHCP) system of wireless phone. Thus, the microwave emission could be easily recognized.

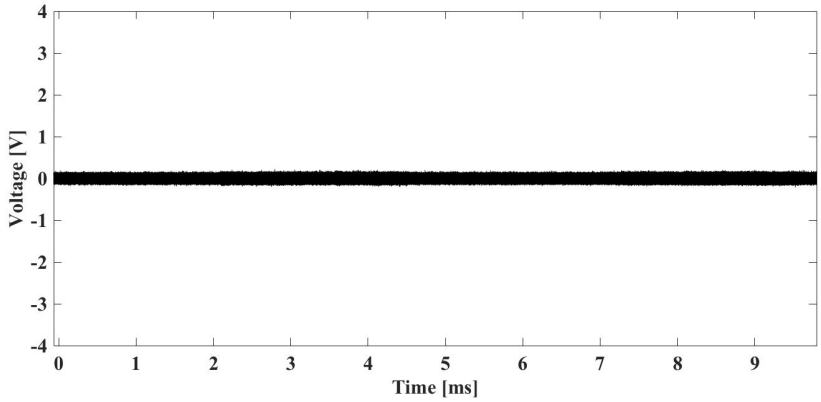

FIGURE 4.8: The typical noise waveform observed at the LP antenna

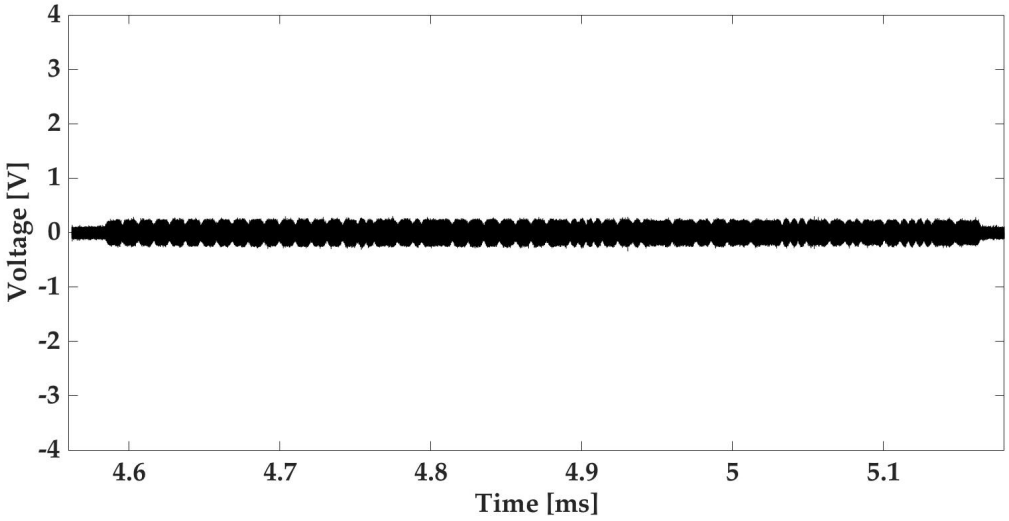

(A) Waveforms of the communication noise

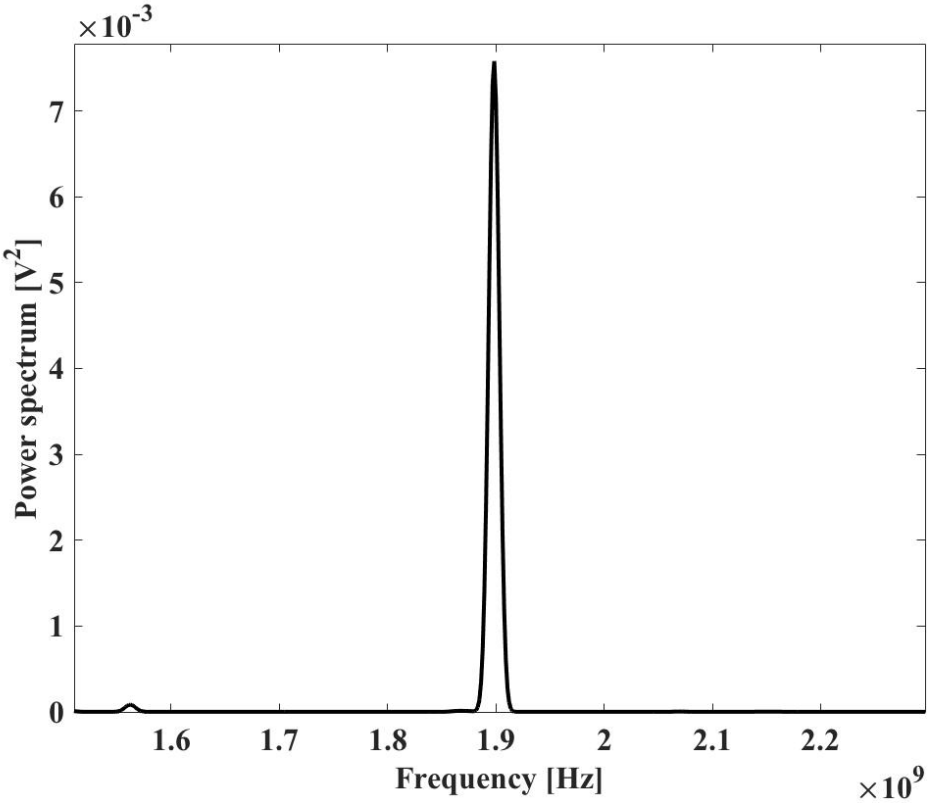

(B) Frequency components of the waveforms

FIGURE 4.9: Communication noise observed with microwave receivers

4.5 Experimental Condition

The experimental condition is shown in Tab.4.1. The target material dependence was examined by selecting the target material under the condition that the physical property value does not change as much as possible. Pure aluminum and aluminum alloy plates were used for the target materials. The 7mm-diameter nylon sphere projectile was selected. The velocity of projectile ranges from 6.8 km/s to 7.4 km/s, i.e. 7 km/s. The vacuum degree is evacuated to around several pascals.

TABLE 4.1: The experimental condition using various kinds of aluminum targets.

Shot ID	Target material	Size [mmxmm]	Thickness[mm]	Projectile materials	Diameter[mm]	Velocity[km/sec]
#180202	Aluminum(7075)	110x110	40	Nylon	7.0	7.4
#180203	Aluminum(1050)	110x110	40	Nylon	7.0	7.1
#180207	Aluminum(6061)	110x110	40	Nylon	7.0	7.0
#190901	Aluminum(1050)	110x110	40	Nylon	7.0	7.0
#190906	Aluminum(1050)	110x110	40	Nylon	7.0	7.0
#190904	Aluminum(7075)	110x110	40	Nylon	7.0	6.8
#190905	Aluminum(7075)	110x110	40	Nylon	7.0	6.7
#190908	Aluminum(6061)	110x110	40	Nylon	7.0	7.0
#191201	Aluminum(7075)	110x110	40	Nylon	7.0	7.06
#191202	Aluminum(1050)	110x110	40	Nylon	7.0	7.14
#191203	Aluminum(6061)	110x110	40	Nylon	7.0	7.08
#191204	Aluminum(2017(T6))	110x110	40	Nylon	7.0	7.00
#191205	Aluminum(2017(O))	110x110	40	Nylon	7.0	7.00
#191206	Aluminum(2017(T3))	110x110	40	Nylon	7.0	7.10
#191207	Honeycomb	90x90	25	Nylon	7.0	7.03
#191208	Honeycomb	90x90	25	Nylon	7.0	7.14

4.6 Comparison of Microwave Emission and Other Phenomena

The simultaneous measurements of electrical phenomena were performed. When a nylon sphere projectile impacts on the 7075 aluminum alloy target, the crater created on the surface of the aluminum target is shown in Fig. 4.10. The expansion of the luminous vapor cloud is observed from the hypervelocity impact by the high-speed video camera in Fig. 4.11. The cloud expands with the velocity of km/s in the surrounding space in vacuum and the edge of the cloud reaches at the edge of the vacuum chamber at μs after the impact. The maximum temperature of the luminous vapor cloud is 3228 K from results of the streak camera spectroscopy measurement.

The waveforms of plasma current at each plasma probe are shown in Fig. 4.12. Plasma current flows according to plasma density and plasma temperature when plasma passes between electrodes. It is confirmed that the plasma current decreases with the distance from the impact point because the plasma expands from the impact point spatially. Plasma reaches at the edge of the vacuum chamber at μs after the impact. After arriving at the edge of the chamber, the plasma disappears due to loss of energy.

The microwave signals are shown in Fig. 4.13. The waveform shows microwave emission until 100 μs after the impact to compare with luminous vapor and plasma phenomena. Figure 4.13a shows microwave signals at higher frequency bands.

Figure 4.14 indicates the comparison with microwave signals measured from two LP antennas. The expanded waveforms measured from the two LP antennas are shown in Fig. 4.14a. The microwaves received from the two LP antennas were observed at the same time. The duration of the microwave emission is dozens of nanoseconds. The frequency spectra of the expanded waveforms are shown in Fig. 4.14b. It was confirmed that the frequency components of microwave emission include a broadband frequency.

Thus, it is clarified that microwave signals have a periodic time of several or dozens of microseconds intermittently and last over a longer time unlike other phenomena. It is suggested that microwave emission is unlikely to be emitted by plasma or luminous gas phenomena.

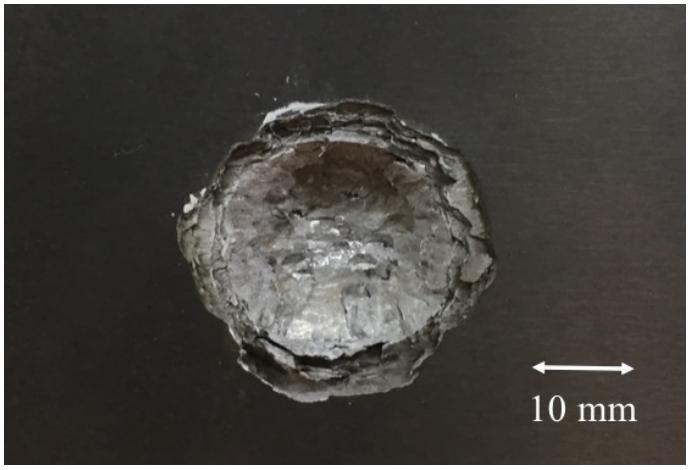

FIGURE 4.10: A photo of the crater on the surface of the 7075 aluminum alloy target

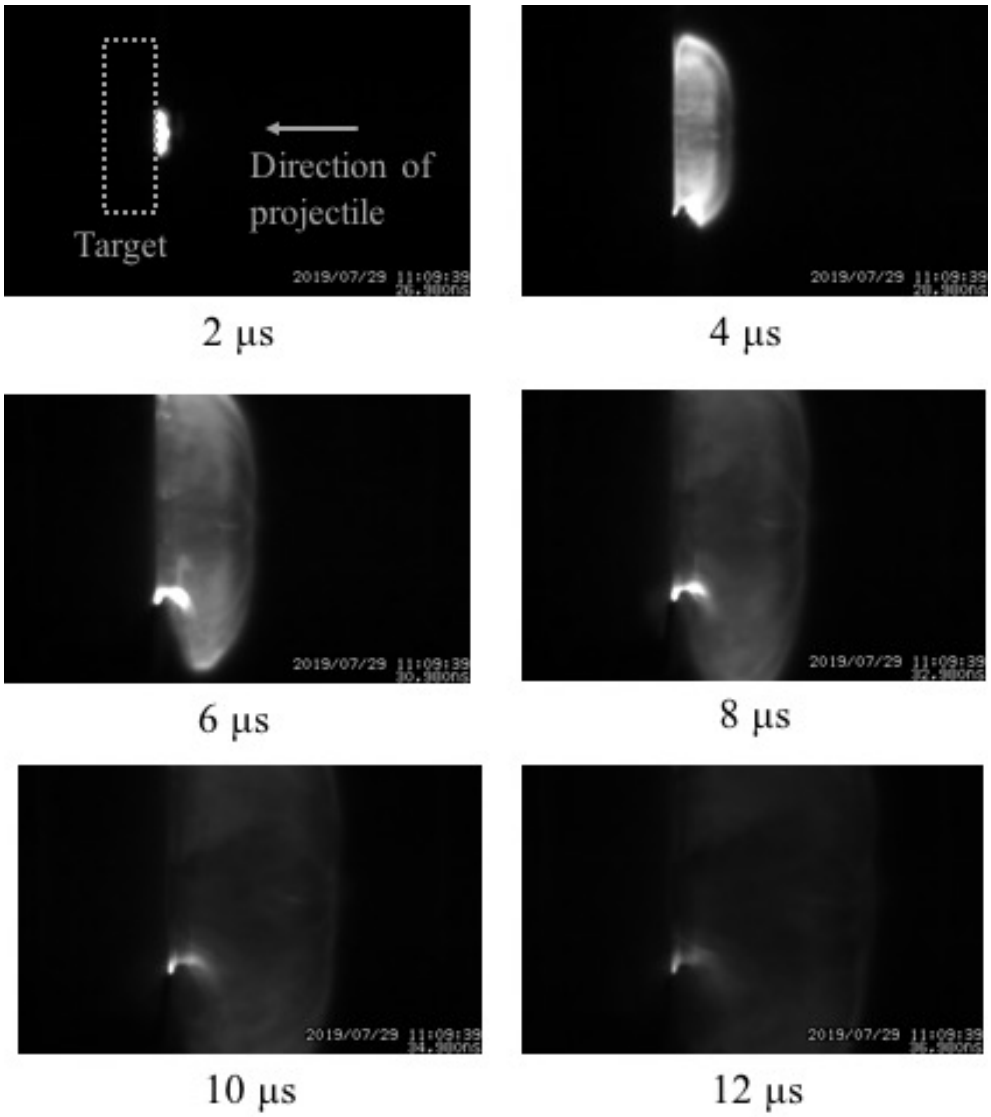

FIGURE 4.11: Photos of luminous vapor cloud from 7075 aluminum alloy target

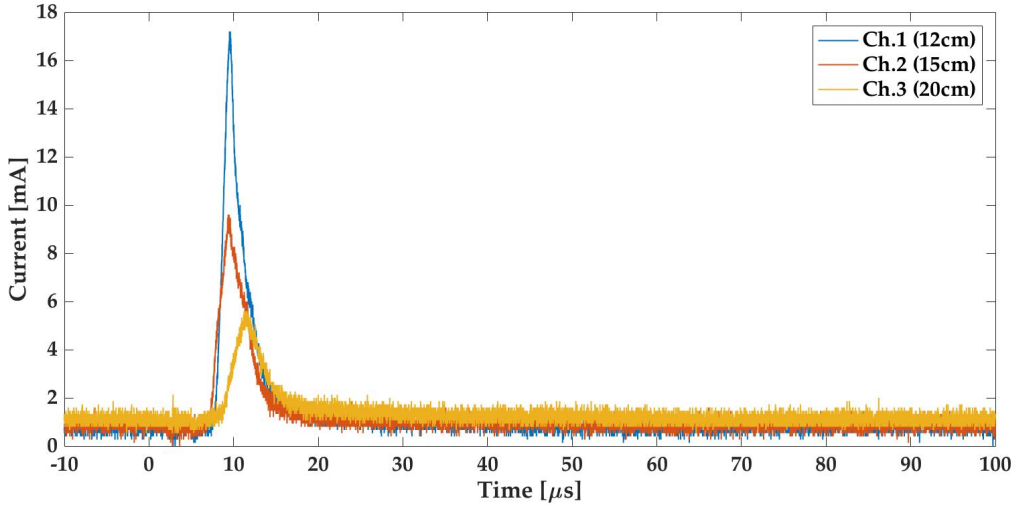

FIGURE 4.12: Waveforms of plasma currents from 7075 aluminum alloy target

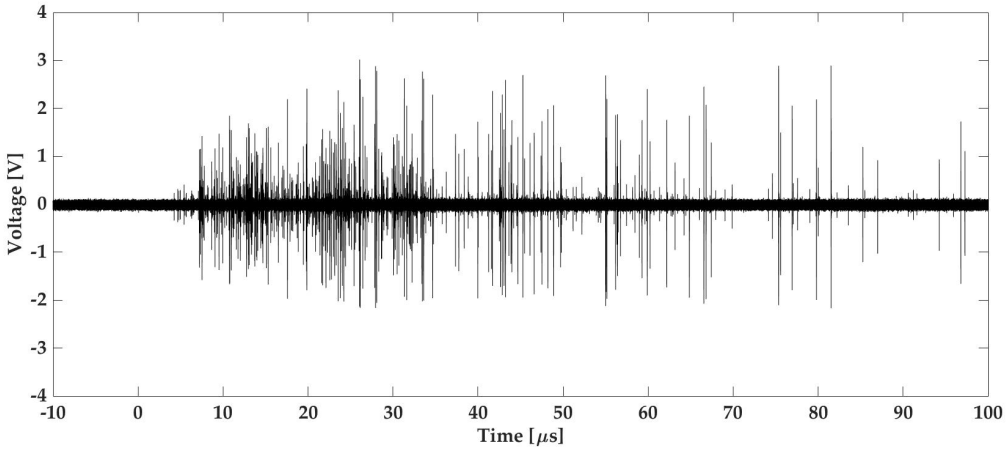

(A) The Waveform of microwave emissions at higher frequency bands

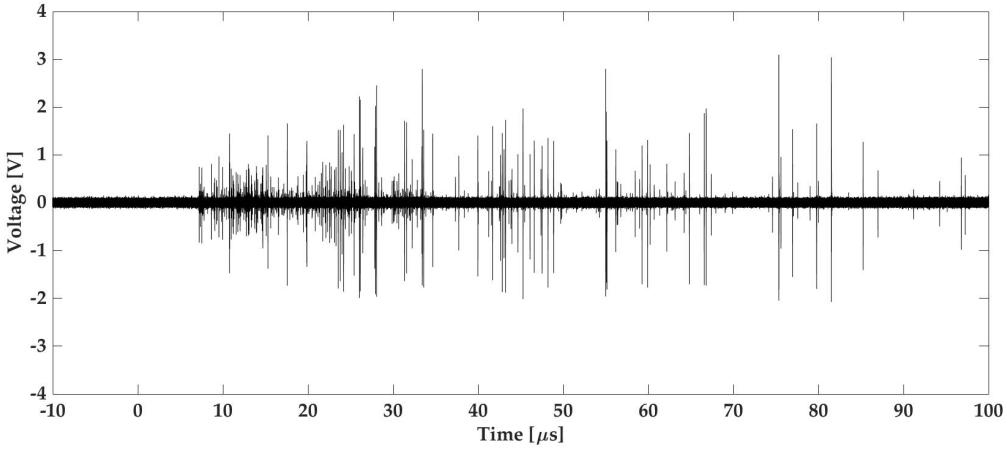

(B) The Waveform of microwave emissions at lower frequency bands

FIGURE 4.13: Waveforms of microwave emission from 7075 aluminum alloy target.

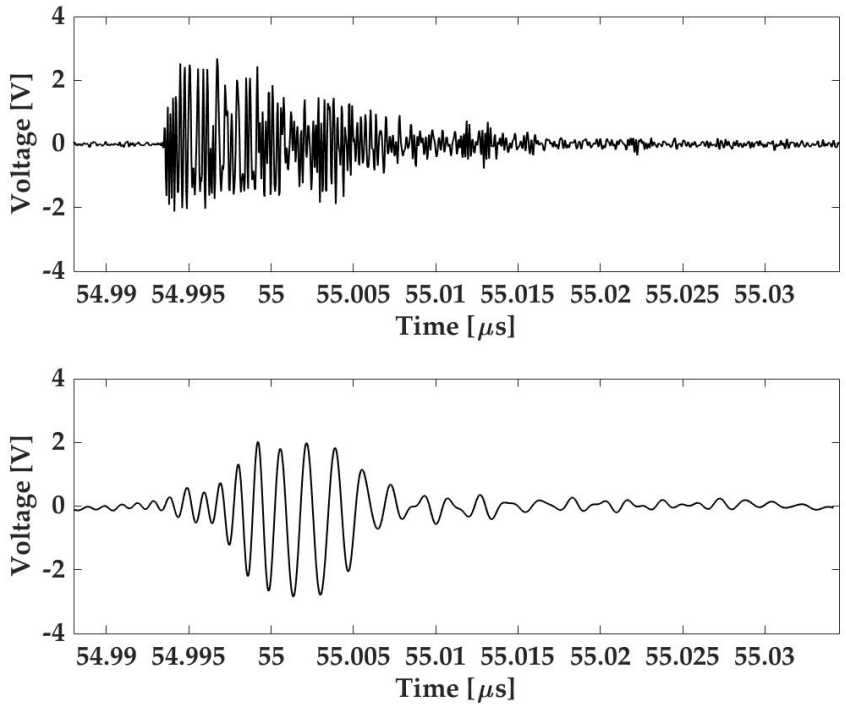

(A) The expanded waveforms measured from the LP antennas with higher frequency bands (upper side) and the LP antennas with lower frequency bands (lower side)

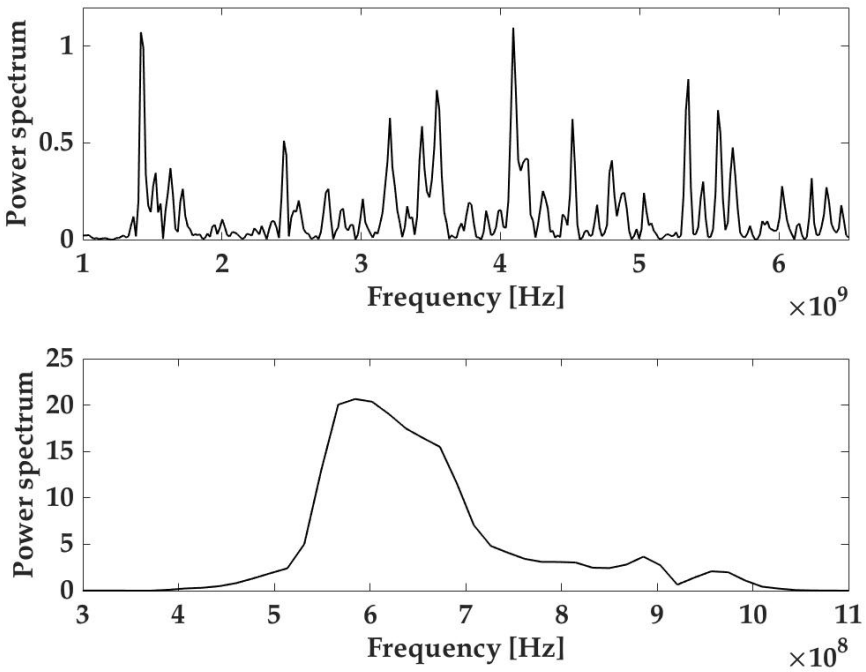

(B) The frequency spectra of expanded waveforms measured from the LP antennas with higher frequency bands (upper side) and the LP antennas with lower frequency bands (lower side)

FIGURE 4.14: Comparison with waveforms measured from LP antennas.

4.7 Relationship between Impact Plasma and Microwave Emission

Figure 4.15 shows the expanded waveform of microwave emission from LP antennas during 40 μs. Figure 4.15a indicates the expanded waveforms measured from LP antenna at higher frequency bands. At point a, the microwave signal was firstly detected at 4.23 μs from hypervelocity impact. Figure 4.15b indicates the expanded waveforms measured from LP antenna at lower frequency bands. At point b, the microwave signal was firstly detected at 25.41 μs from hypervelocity impact. Comparing with the both waveforms, the difference of the receiving time is 21.19 μs. It was found that microwave with higher frequency bands can be detected earlier than one with lower frequency bands.

Next, the groups of microwave pulses were analyzed in detail. Figure 4.16 shows the expanded waveform at point c at the top of the figures and the power spectrum of the waveform at the bottom of the figures. The power spectrum was obtained by using FFT analysis. The duration of the waveforms is 80.96 ns (sampling points: 2048 (=2^{11}), sampling frequency: 25 GHz, frequency resolution: 12.4 MHz, Window function: Hanning). The power spectrum of the waveform above 3800 MHz was detected as the red line is shown. Figure 4.17 shows the expanded waveform at point d at the top of the figures and the power spectrum of the waveform at the bottom of the figures. The power spectrum of the waveform above 3000 MHz was detected as the red line is shown. Figure 4.18 shows the expanded waveform at point e at the top of the figures and the power spectrum of the waveform at the bottom of the figures. The power spectrum of the waveform above 1500 MHz was detected as the red line is shown. Figure 4.19 shows the expanded waveform at point f at the top of the figures and the power spectrum of the waveform at the bottom of the figures. The power spectrum of the waveform above 1000 MHz which is the lower limit frequency of the LP antenna was detected as the red line is shown. The microwave observed at LP antenna with lower frequency bands is also detected at 28.06 μs of point f. Comparing the frequency spectra of the microwaves from hypervelocity impact, it was found that power spectra with low frequencies began to be observed over time.

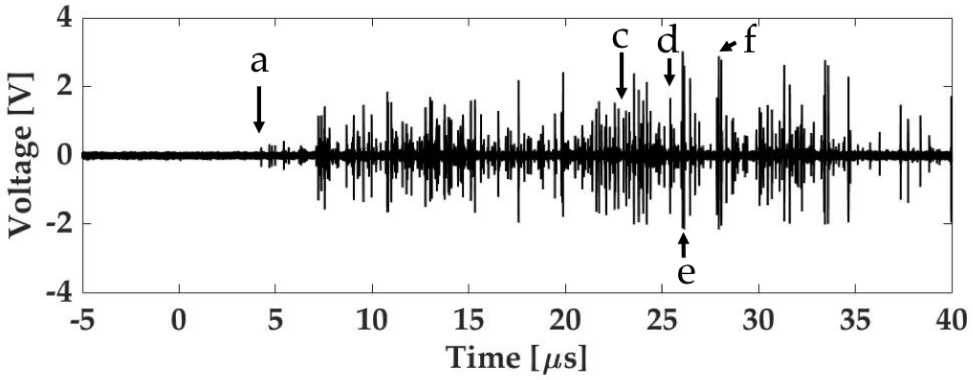

(A) The expanded waveforms measured from LP antenna at high frequency bands during 40 microseconds

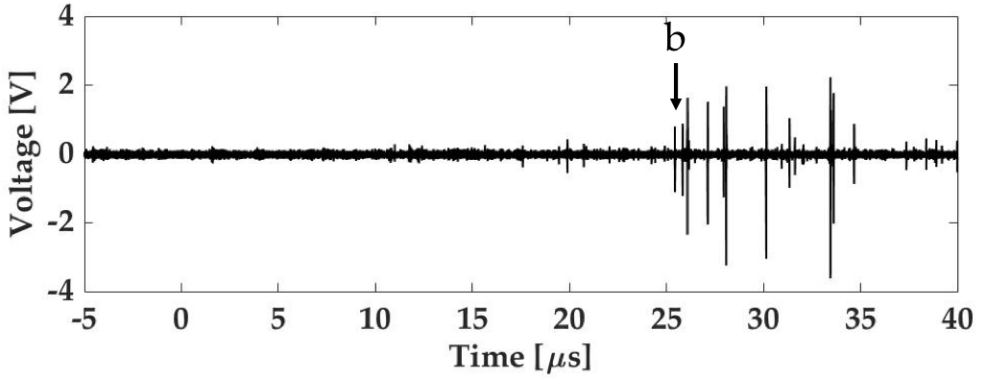

(B) The expanded waveforms measured from LP antenna at low frequency bands during 40 microseconds

FIGURE 4.15: Comparison with waveoforms measured from LP antennas during 40 microseconds.

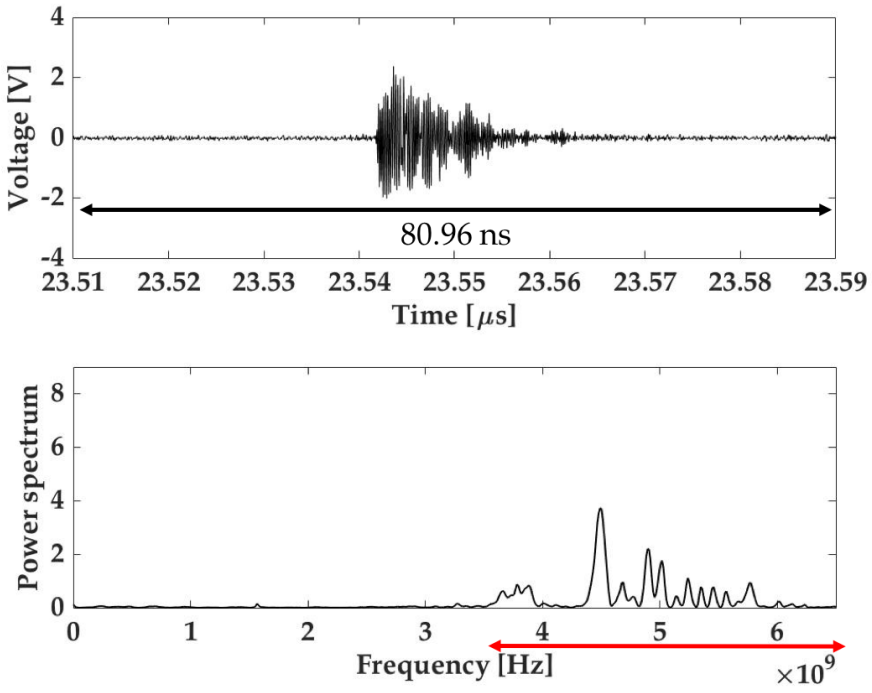

FIGURE 4.16: The expanded waveform at point c and the power spectrum

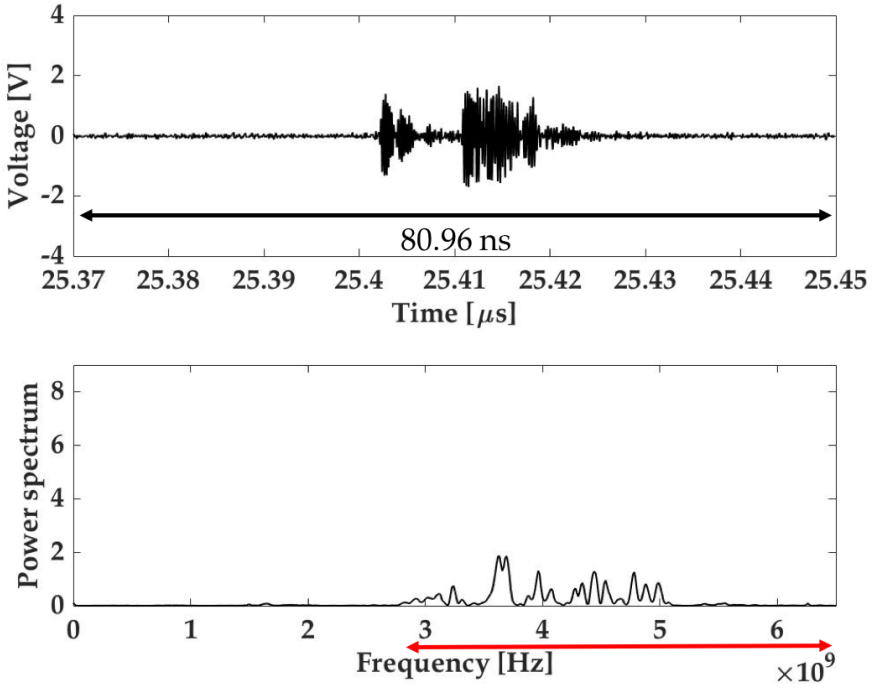

FIGURE 4.17: The expanded waveform at point d and the power spectrum

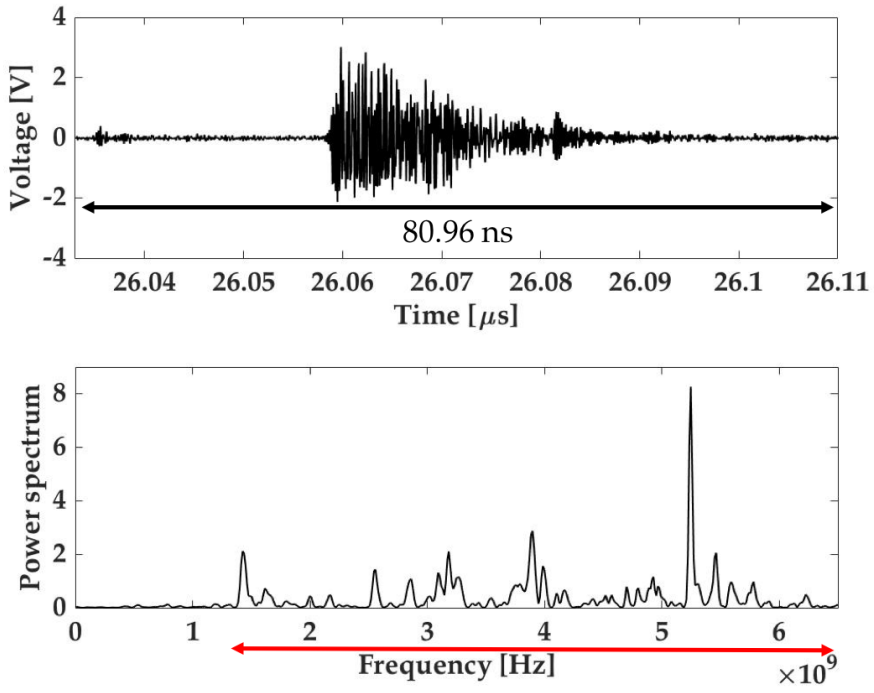

FIGURE 4.18: The expanded waveform at point e and the power spectrum

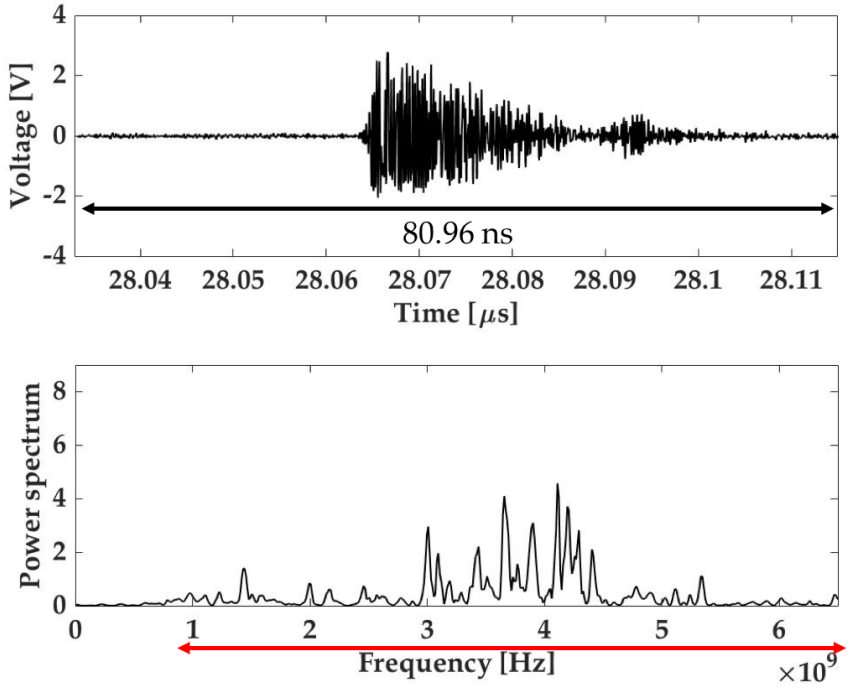

FIGURE 4.19: The expanded waveform at point f and the power spectrum

TABLE 4.2: The plasma density at each plasma probe.

Channel	**Plasma current I_p [mA]**	**Plasma density N_e [cm^{-3}]**
12cm	17.2	1.36×10^{12}
15cm	9.6	7.58×10^{11}
20cm	5.6	4.42×10^{11}

Herein, the relationship between impact plasma and microwave emission is investigated. The plasma currents at each probe are measured in Fig. 4.12. Each plasma probe is located at 12cm (Ch.1), 15cm (Ch.2), and 20cm (Ch.3) from the impact points. The maximum currents at each plasma probe are 17.2 mA, 9.6 mA, and 5.6 mA, respectively. In Chapter 2, the temperature of the luminous cloud was obtained. By using the maximum plasma current and the maximum temperature of 3228 K, the maximum plasma density N_e is calculated.

It is confirmed that the plasma density N_e is highly dense comparing with ionosphere plasma (Tribble, 2003). To investigate the interaction between plasma and microwave emission, plasma cutoff frequency f_{th} is calculated. The equation is given by

$$f_{th} = \frac{1}{2\pi}\sqrt{\frac{N_e e^2}{m_e \epsilon_o}} \tag{4.1}$$

with ϵ_o is permittivity of vacuum, m_e is mass of electron, and e is elementary charge (Tonks and Langmuir, 1929). Plasma cutoff frequency f_{th} depends on plasma density N_e, and the higher plasma density is, the higher plasma cutoff frequency f_{th} is. The relationship between plasma cutoff frequency f_{th} and time is shown in Fig. 4.20. The red and blue lines indicate the upper limit frequency of the LP antenna with higher frequency bands and with lower frequency bands, respectively. The difference time between upper limit frequencies with LP antennas induces approximately 20 μs. Therefore, it means that the microwave emission is shielded by high-dense plasma of impact plasma during dozens of microseconds. Also, it is suggested that microwave emission happens inside the impact plasma.

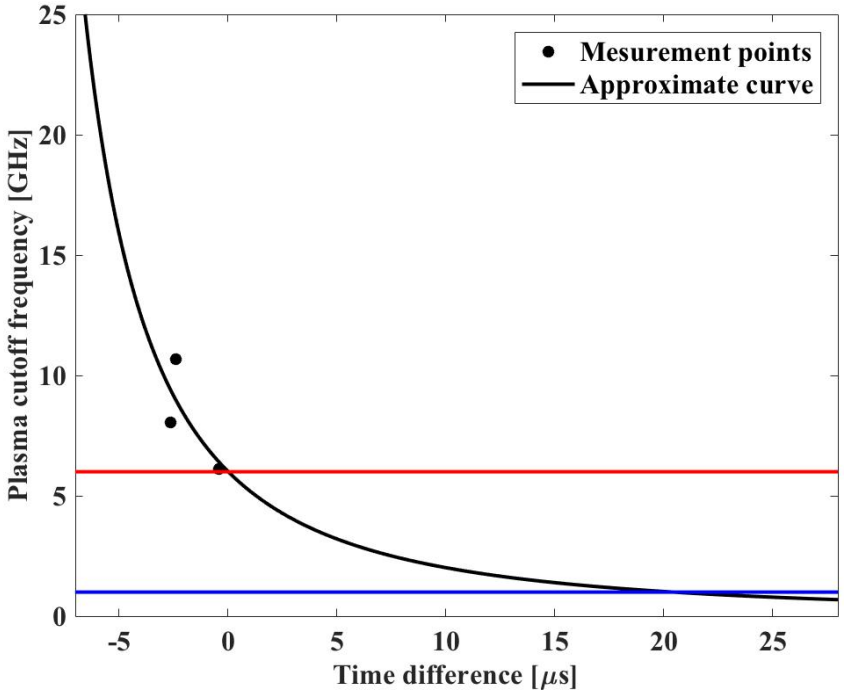

FIGURE 4.20: The temporal change of plasma cutoff frequency

TABLE 4.3: The crater parameters depending on hardness of target materials.

Aluminum	Brinell hardness	Crater depth [mm]	Crater volume [mm^3]
A1050	23	15	5461.69
A6061	95	9	2289.95
A7075	150	8	1733.28

4.8 Microwave Emissions from Various Kinds of Aluminum Targets

4.8.1 Microwave Emissions from Various Kinds of Aluminum Alloy Targets

The target material dependence was examined by selecting the target material under the condition that the physical property value does not change as much as possible. Pure aluminum and aluminum alloy plates were used for the target materials to examine the influence of hardness. The hardness of targets is related to crater depth and the equation of expected crater depth D is given by

$$D = 5.24 H^{-1/4} \left(\frac{\rho_p}{\rho_t}\right)^{1/2} \left(\frac{V_n}{C_t}\right)^{2/3} d^{19/18} \tag{4.2}$$

with H is Brinell hardness, ρ_p is density of projectile, ρ_t is density of target, V_n is impact velocity, C_t is sound velocity of target material, and d is diameter of projectile (Cour-Palais, 1985). Figure 4.21 shows expected crater depth depending on hardness of targets. In the experiments, the pure aluminum, 6061 aluminum alloy, 7075 aluminum alloy targets were selected. The Brinell hardness of each material and parameters of crater are shown in Tab. 4.3. Also, photos of craters created on the surface of each target are shown in Fig. 4.22. It can be confirmed that hardness of target materials affects the crater depth and volume.

Figure 4.23 shows microwave emissions after impacts on pure aluminum, 6061 aluminum alloy, and 7075 aluminum alloy targets. The 7 mm-diameter nylon projectile with a velocity of approximately 7 km/s was used for a projectile. The peak-to-peak volatge of pure aluminum, 6061 aluminum alloy, and 7075 aluminum alloy targets are 4.625 V, 6.005 V, and 6.137 V, respectively. It was found that the harder the target is, the smaller the crater volume is and the higher the intensity of microwave emission is. Thus, it was suggested that the intensity of microwave emission may depend on the hardness of the target material as a mechanism of microwave emission.

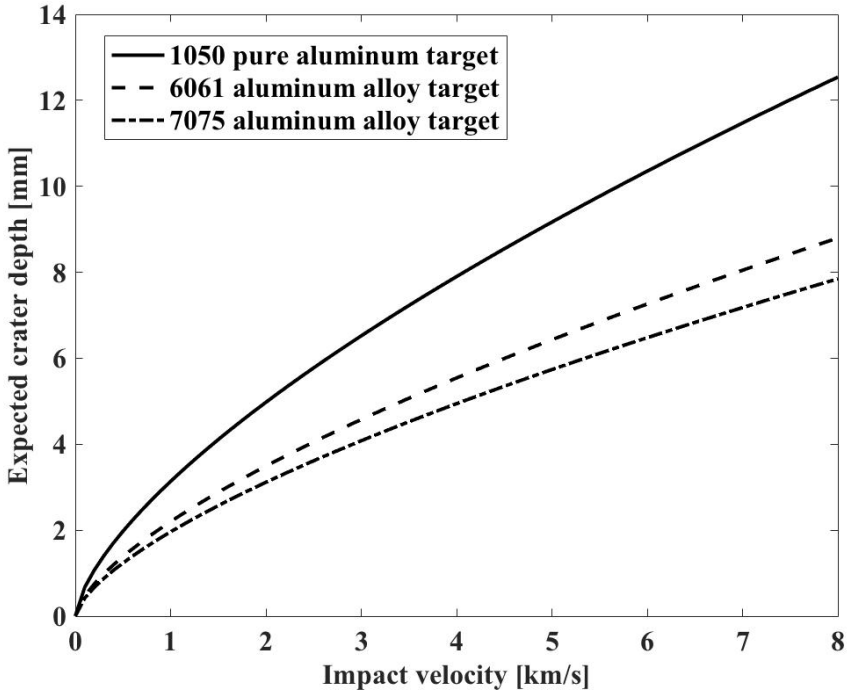

FIGURE 4.21: Expected crater depth depending on hardness of targets

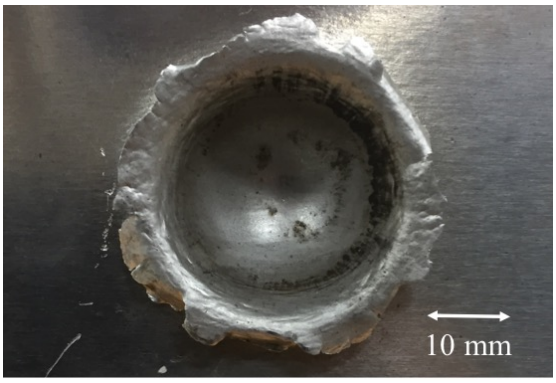

(A) A photo of the crater on the surface of 1050 pure aluminum target

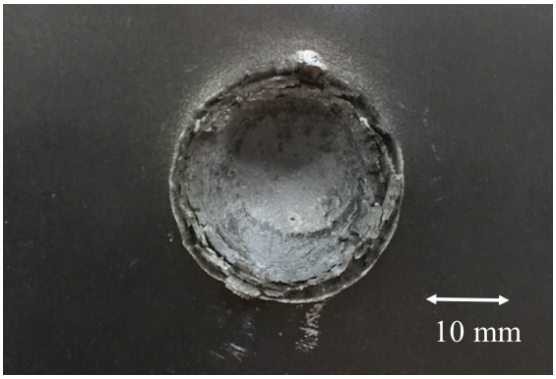

(B) A photo of the crater on the surface of 6061 aluminum alloy target

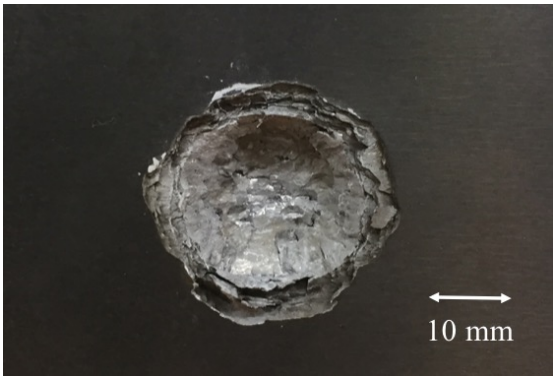

(C) A photo of the crater on the surface of 7075 aluminum alloy target

FIGURE 4.22: Photos of the surface of the targets after impacts.

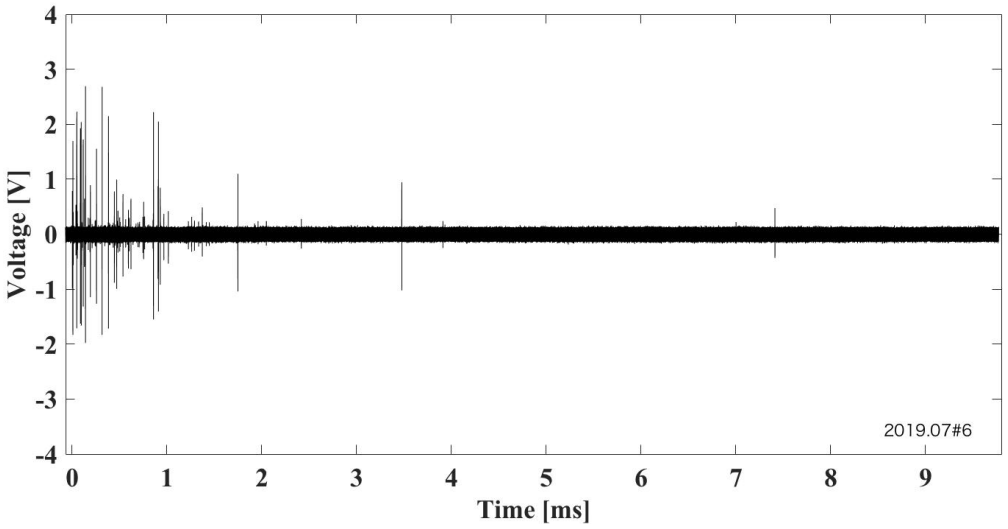

(A) Microwave emissions from the 1050 pure aluminum target (Full span)

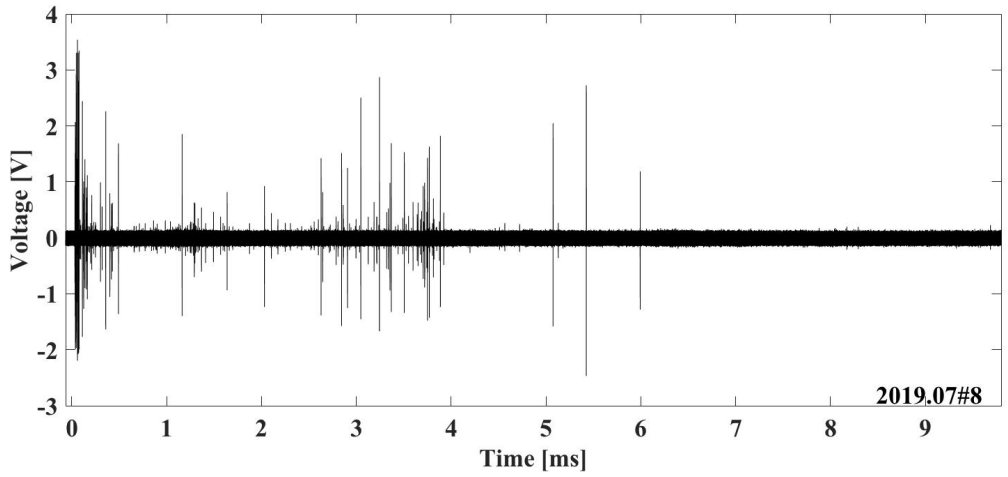

(B) Microwave emissions from the 6061 aluminum target (Full span)

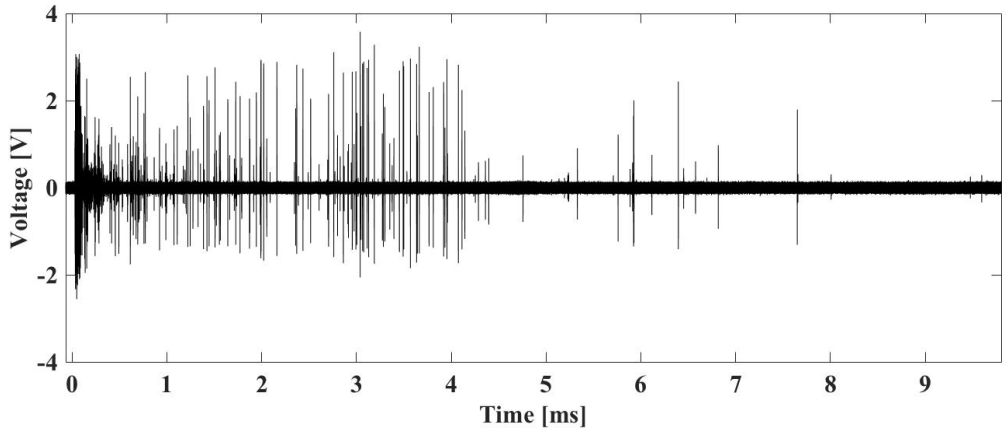

(C) Microwave emissions from the 7075 aluminum target (Full span)

FIGURE 4.23: Microwave emissions depending on aluminum targets.

4.8.2 Dependence of Microwave Emissions from Different Heat Treated Aluminum Alloy Targets

Different aluminum alloys differ not only in hardness but also in other properties slightly due to different proportions and materials of impurities. In this section, microwave emission was compared by selecting the target of three different heat treated 2017 aluminum alloy plates, which contains the same proportions of impurities.

Heat treating refers to any of the heating and cooling operations that are performed for the purpose of changing the mechanical properties such as hardness with few exceptions (Committee, 2013). The commercial heat-treatable aluminum alloys are based on ternary or quaternary systems with respect to the solutes involved in developing strength by precipitation. Commercial alloys whose strength and hardness can be significantly increased by heat treatment include 2xxx, 6xxx, and 7xxx series wrought alloys (except 7072). Heat treatment to increase strength of aluminum alloys is a three-step process: solution heat treatment, quenching, and age hardening.

Annealing treatments employed for aluminum alloys are of several types that differ in objective. The softest, most ductile, and most workable condition is produced by full annealing to the temper designated "O."

Alloys in T6-type tempers generally have the highest strengths practical without sacrifice of the minimum levels of other properties and characteristics found by experience to satisfactory and useful for engineering applications.

In the experiments, the 2017 aluminum alloys in O, T3, and T6-types tempers were used for targets. Before the experiments, Brinell hardness of each target was measured. Figure 4.24 shows the photos of the surface of the different thermal refining targets after impacts. By heat treatment, the craters seem to be different. The crater on the surface of 2017-O aluminum alloy target is the biggest volume in Fig. 4.24a, and the one on the surface of 2017-T6 aluminum alloy target is the biggest volume in Fig. 4.24c. The Vickers hardness of 2017-O, 2017-T3, and 2017-T6 is 56.93, 113.08, and 131.93, respectively.

Figure 4.25 shows the comparison of microwave emission received from the LP antenna with higher frequency bands. Microwave emission from the 2017-O aluminum alloy target was mainly confirmed during approximately 1.5 ms in Fig. 4.25a. Figure 4.25b shows microwave signals from the 2017-T3 aluminum alloy target. It can be seen that microwave signals from the 2017-T3 aluminum alloy target are much stronger than ones from 2017-O aluminum alloy target. In addition, microwave signals from the 2017-T6 aluminum alloy target are shown in Fig. 4.25c. It was found that microwave signals from the 2017-T6 aluminum alloy target are the strongest of the three targets.

Therefore, it was found that the harder the target material, the stronger the microwave emissions. I clarified that hardness of target materials affects microwave emissions.

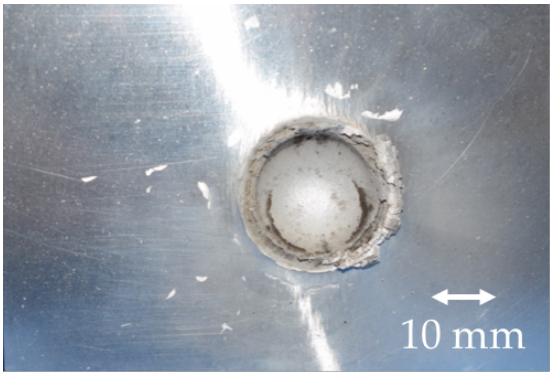

(A) A photo of the crater on the surface of 2017-O aluminum alloy target

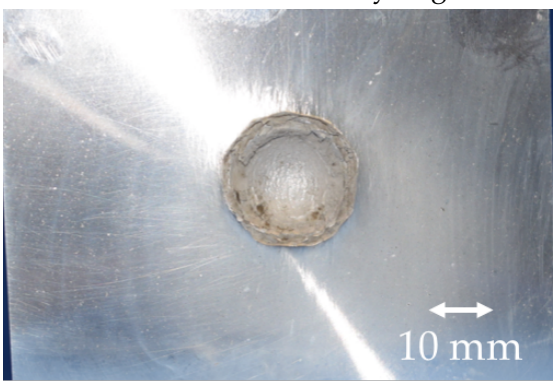

(B) A photo of the crater on the surface of 2017-T3 aluminum alloy target

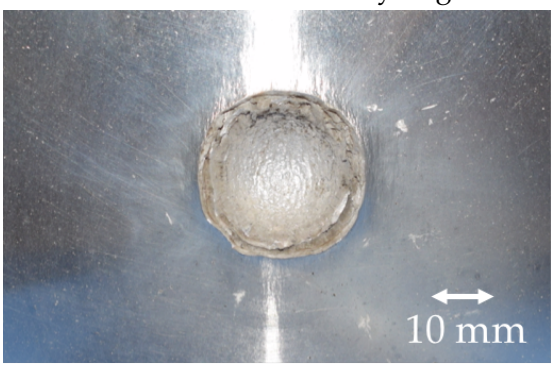

(C) A photo of the crater on the surface of 2017-T6 aluminum alloy target

FIGURE 4.24: Photos of the surface of the different thermal refining targets after impacts.

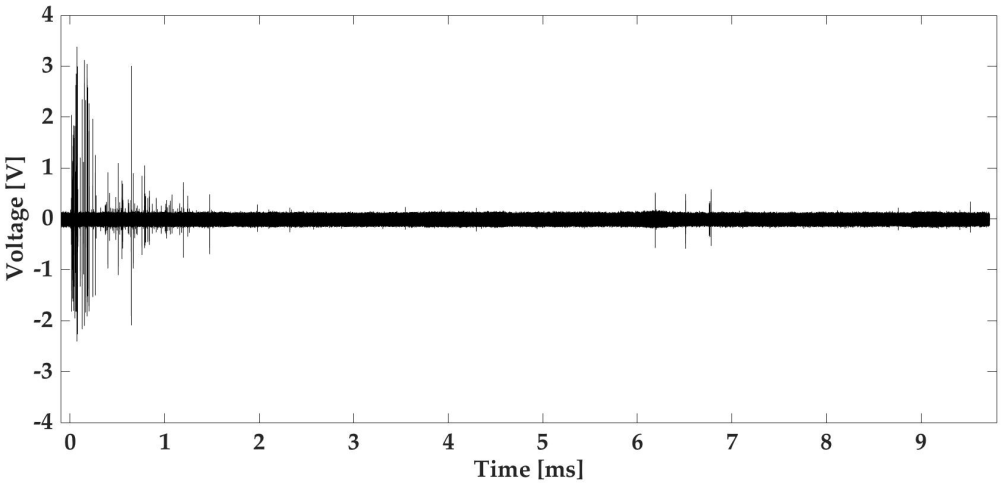

(A) Microwave emissions from 2017-O aluminum alloy target

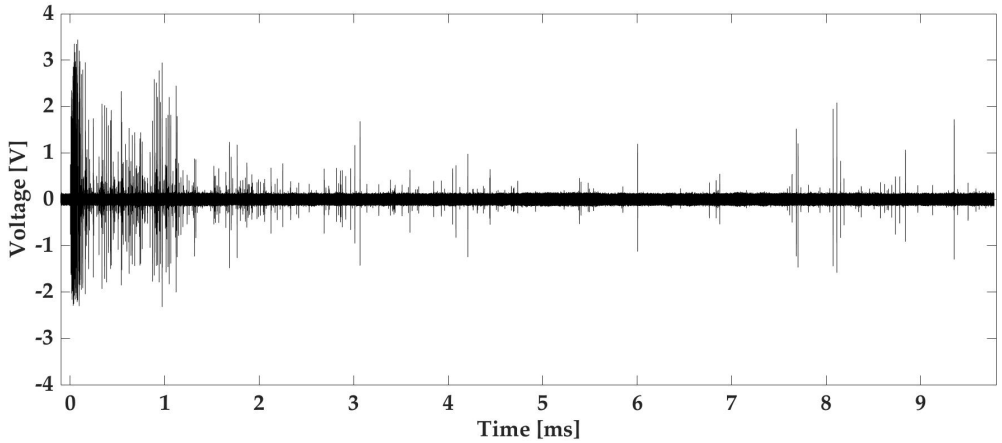

(B) Microwave emissions from 2017-T3 aluminum alloy target

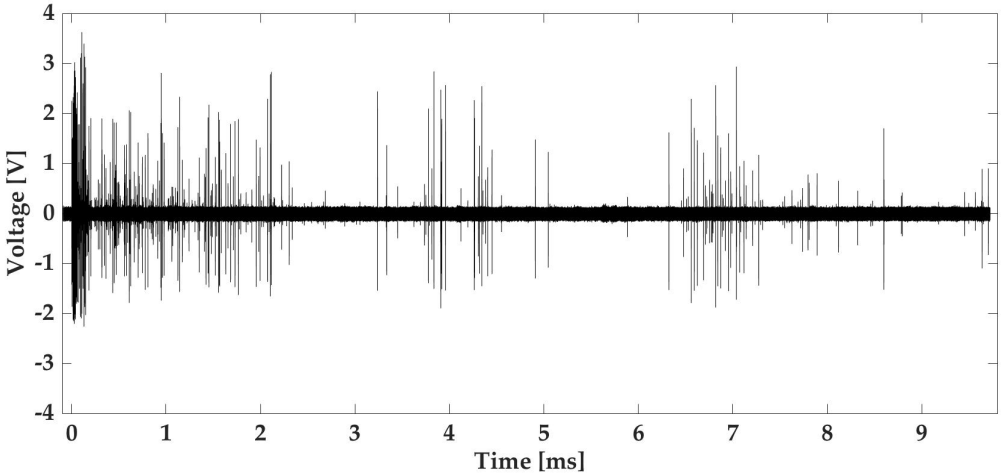

(C) Microwave emissions from 2017-T6 aluminum alloy target

FIGURE 4.25: Comparison of microwave emissions from 2017 aluminum alloy plates received from the LP antenna with higher frequency bands

4.8.3 Analysis of Numerical Simulation

In the previous section, I clarified that hardness of target materials affects microwave emission. Next, the fracture in the target was simulated by using a numerical simulation in order to investigate the relationship between material hardness and the effect of fracture in the target.

When solids generally collide with each other at a speed above 1 km/s, the collision pressure exceeds giga pascal order and exceeds the elastic limit of most substances (M. S. Cowler and Obata, 1987; Mechanical Engineers, 2007). Therefore, a complicated phenomenon mixed with solids and fluids happens. I used the numerical simulation of ANSYS AUTODYN-3D, which can be applied for impact analysis of complex physical systems including fluid and solid materials. In particular, the elastic wave which is propagated in the target was focused on.

As in almost all hydrocodes, the material model consists of three parts: 1) the equation of state (E.O.S.) descriing the relationship among pressure, density, and internal energy, 2) the material strength model with the constitutive relation of solid materials, and 3) the failure or fracture model mainly for solid materials. The projectile and targets are modeled on the Lagrange solver.

The projectile was assumed spherical and to have the properties of nylon with 7 mm in diameter and 7 km/s in velocity. Targets are pure aluminum, 6061 aluminum alloy, and 7075 aluminum alloy targets. The subgrid mesh is applied to save computing resorces. The mesh size of the impact point neighborhood is about 1 mm and the mesh size increases with distance from the impact point. The three-dimentional analytical model is shown in Fig. 4.26. The material properties of nylon (66 nylon) are described by the material library of AUTODYN. The equation of state is used with shock.

The material strength is von Mises. The erosion function is set to prevent the calculation meshes from being crushed and the calculation from stopping. The material properties of aluminum are described by the material library of AUTODYN. The equation of state used with shock. The constitutive law is applied to the Steinberg-Guinan strength model (D. J. Steinberg, 1980). It's effective mainly in the model with the ductile material and it's assumed that the yield stress and the transverse elastic modulus change depending on the state quantity.

The constitutive relations for shear modulus G and yield stress Y for high strain rates are:

$$Y = Y_0 \left\{1 + \beta_{SG} \left(\bar{\varepsilon}_p + \varepsilon_j\right)\right\}^n \cdot \left\{1 + \left(\frac{Y'_P}{Y_0}\right) \frac{P}{\eta^{1/3}} + \left(\frac{G'_T}{G_0}\right) \left(T - T_{\text{room}}\right)\right\} \quad (4.3)$$

$$G = G_0 \left\{1 + \left(\frac{G'_P}{G_0}\right) \frac{P}{\eta^{1/3}} + \left(\frac{G'_T}{G_0}\right) \left(T - T_{\text{room}}\right)\right\} \quad (4.4)$$

where density ρ is used in $\eta = \rho/\rho_{ref}$, where ρ_{ref} is the reference density. However, the maximum yield strength value Y_{max} does not exceed a value that is shown

$$Y_0 \left\{1 + \beta_{S-G} \left(\bar{\varepsilon}_p + \varepsilon_i\right)\right\}^n \leq Y_{\max}. \tag{4.5}$$

where $\epsilon_j = 0$ is the initial plastic distortion and usually $\epsilon_j = 0$. T_{room} is room temperature. Y_0 and G_0 are the yield strength and elastic modulus values, respectively, at standardized conditions ($T = 300K$, $P = 0$, $\epsilon_p = 0$). Y' and G', which are variables with subscripts, are partial differential quantities at standardized conditions. $Y_0, G_0, Y'_p/Y_0, G'_T/G_0, \beta_{SG}, n$, and Y_{max} are determined by each experiment. In addition, $Y'_p/Y_0 \approx G'_p/G_0$ is known by a number of past experimental results.

The fracture condition is applied to the fracture model by hydro. The erosion function is set to prevent the calculation meshes from being crushed and the calculation from stopping.

Figure 4.27 shows the crater created by the hypervelocity impact. The depth and the diameter of crater is almost corresponded to ones of crater in the experimental results.

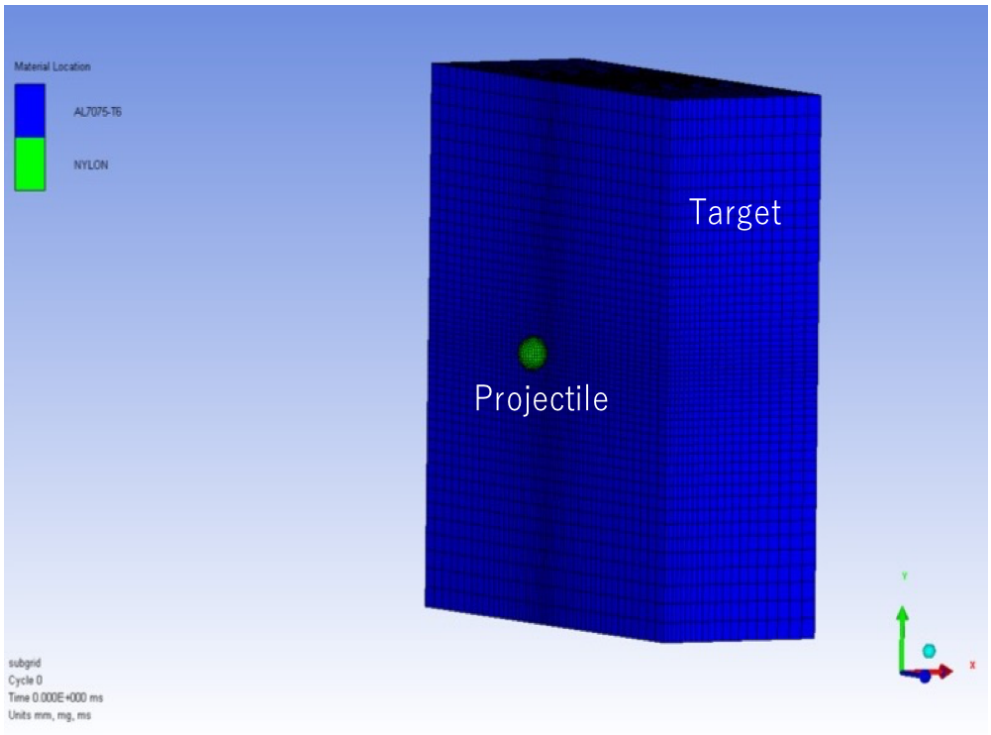

FIGURE 4.26: The analysis model

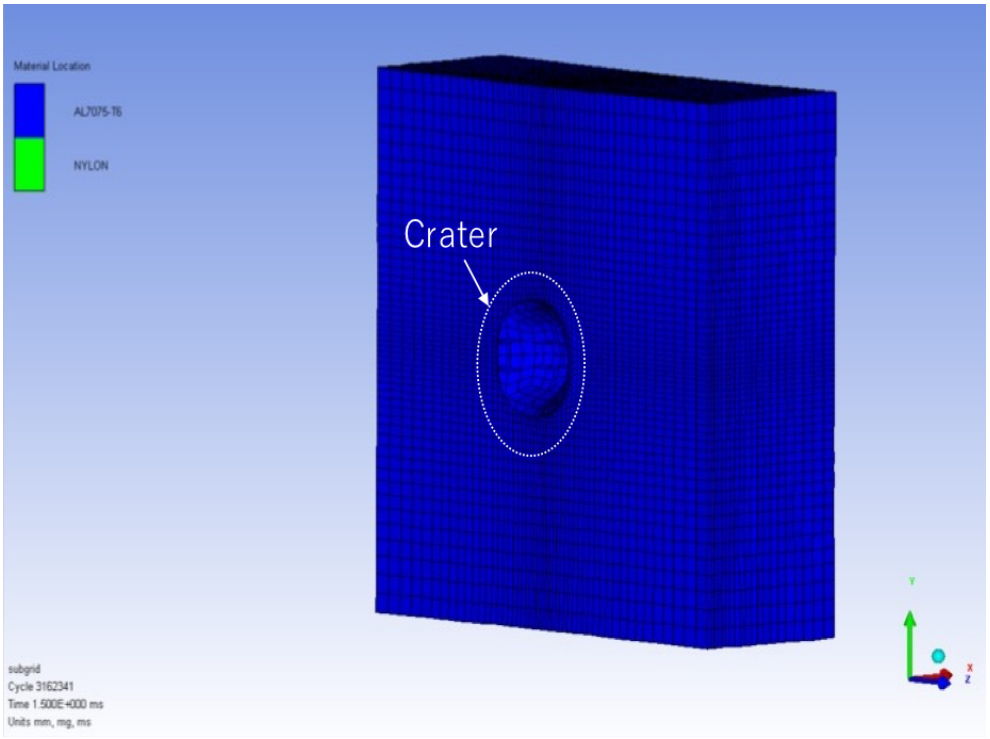

FIGURE 4.27: The crater created by the hypervelocity impact

4.8.4 Relationship between Target Destruction and Microwave Emission

Figure 4.28 shows the pressure distribution inside the target. To compare with amplitude of pressure distribution of each aluminum target, the range of pressure was alighed.

The pressure distriution inside the pure aluminum target is shown in Fig. 4.28a. The site near the crater is strongly pressurized between 49 μs and 51 μs, and then the pressure gets weaker between 53 μs and 55 μs, but the pressure gets stronger again between 57 μs and 61 μs. It is found that the amplitude of pressure is repeatedly changed every several microseconds, because the elastic wave propagates and reflects repeatedly inside the target.

Figure 4.28b shows the pressure distribution inside the 7075 aluminum alloy target. It is also found that the amplitude of pressure is repeatedly changed every several microseconds. In the figure, it should be noted that amplitude of pressure in the 7075 aluminum alloy target is much stronger than one in the pure aluminum target. In Figure 4.29a, the pressure near the impact site was monitored as shown in Fig. 4.28a. Comparing with waveforms inside the pure and 7075 aluminum targets, the amplitude of pressure is obviously different. It is suggested that the pressure of the elastic wave in the pure aluminum target was smaller, because the impact energy of projectile was consumed to form the crater. It is found that hardness of the target affects the amplitude of pressure of the elastic wave.

Figure 4.30 shows the comparison with microwave emissions and the pressure distribution inside the target. The time zones surrounded in the red and blue dotted line at 49 μs and 55 μs are strongly pressurized near the crater site inside the yellow dotted line. Yet, time zones surrounded in the black dotted lines at 52 μs and 53 μs are slightly pressurized. In the field of meterial enginnering, RF emission was confirmed when fracture of rock and other brittle materials are fractued (G. Martelli, 1985; Steven G. O'Keefe, 1995). Therefore, it is supposed that microwave intermittently emits when the crater site is highly pressurized repeatedly and then the materials are fractured.

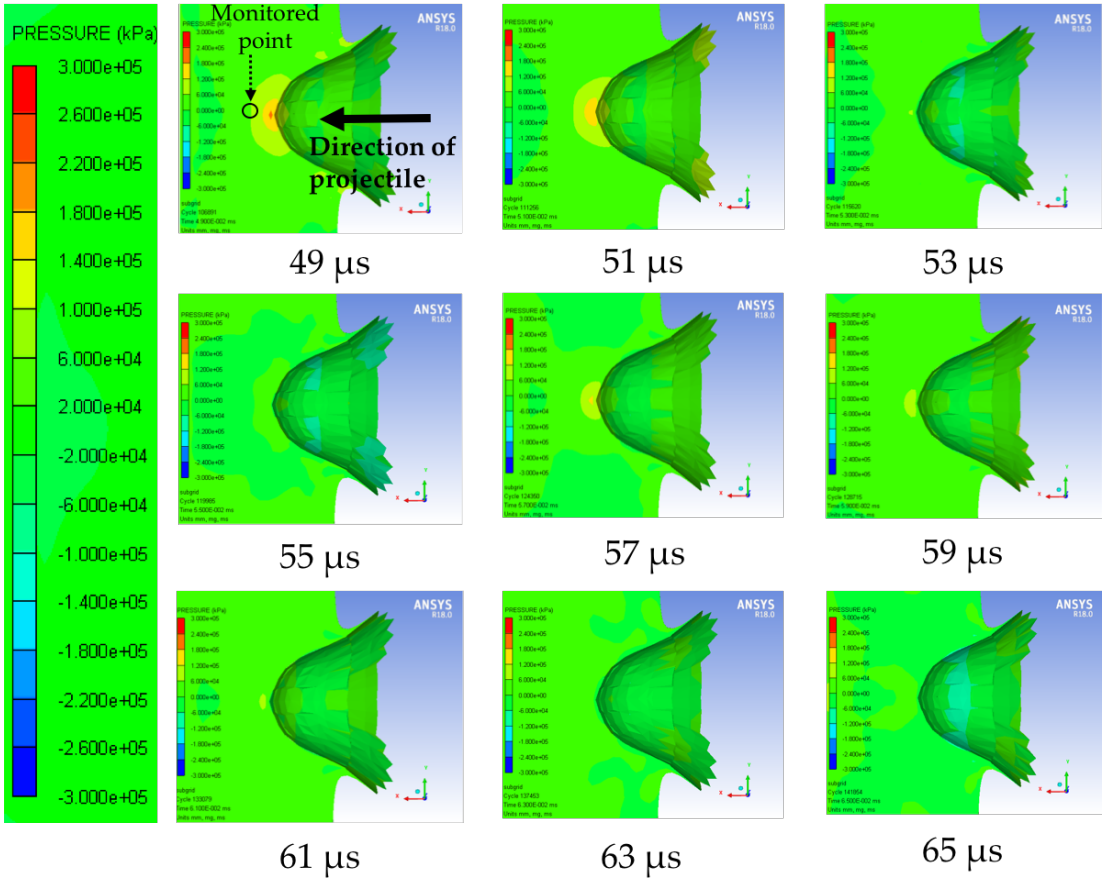

(A) Pressure distribution inside the pure aluminum target

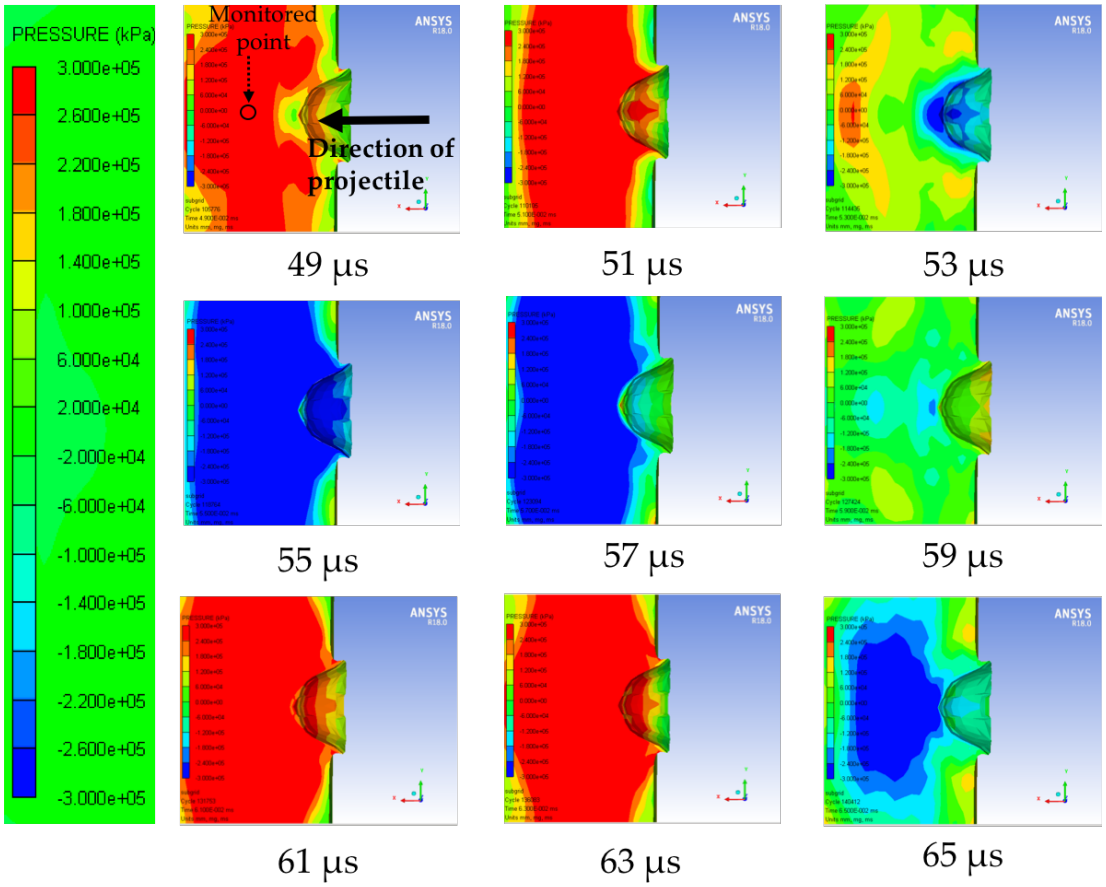

(B) Pressure distribution inside the 7075 aluminum alloy target

FIGURE 4.28: Comparison of pressure distribution inside the targets.

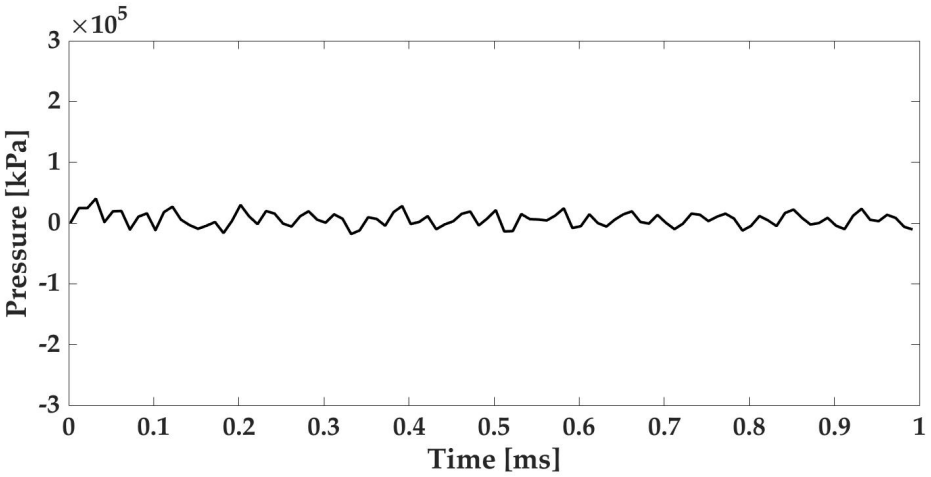

(A) The waveform of pressure inside the pure aluminum target

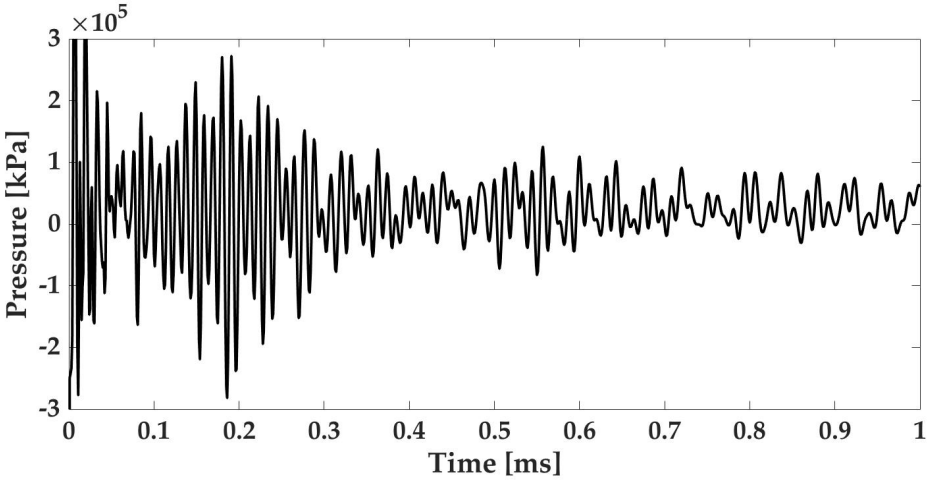

(B) The waveform of pressure inside the 7075 aluminum alloy target

FIGURE 4.29: Comparison of pressure change at the monitored point.

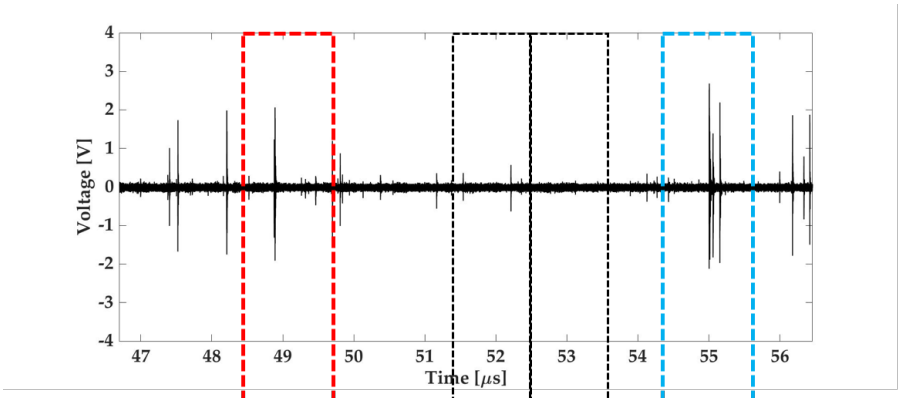

(A) Microwave emission received at the LP antenna with higher frequency bands

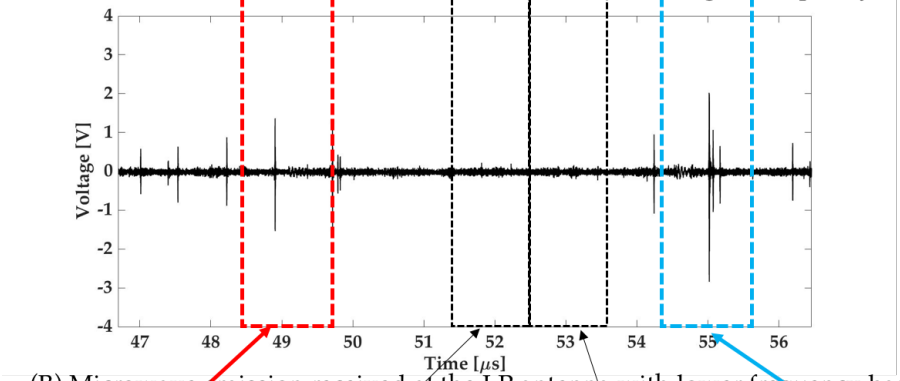

(B) Microwave emission received at the LP antenna with lower frequency bands

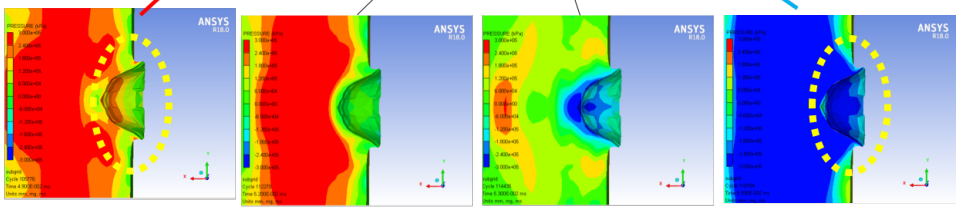

(C) Pressure distribution inside the target

FIGURE 4.30: Comparison with the microwave emissions and the pressure inside the target

4.9 Application for Detecting Debris Impact Using Microwave Emission

4.9.1 Various Kinds of Debris Senser Systems

I investigated and clarified microwave emission phenomenon. When MMOD impact to spacecraft, the tremendous damage may happen. In particular, spacecraft with astronauts such as the ISS or the future moon orbiting spacecraft called Gateway is very crucial to detect the damage caused by MMOD impacts as soon as possible and fix the damage. Also, spacecraft with the large-scale structure such as SPS cannot ignore the damage of impacts.

Therefore, detecting impacts on spacecraft is important and the debris sensors have been considered (IADC-08-03, 2013). There are some sensor systems such as acoustic emission, a resistor-based detection, a calorimetric impact detection, a surface inspection cameras, and microwave emission.

Acoustic emission is detected by an elastic wave in the range of ultrasound usually between 20 kHz and 1 MHz. The elastic wave propagates through the solid to the surface, where it can be recorded by one or more sensors. Yet, the disadvantage of acoustic emission is difficult to distinguish to the signals because the service environments are generally noisy and the signals are very weak.

The resistor-based detector can detect a perforation hole generated by debris impact in a manned space structure using a resistance film, which is attached to a pressurized wall with an insulator (S. Fukushige, 2006). The resistance value of a resistance film with a conductive condition is dependent on the distance between a measurement point and the perforation hole. The resistance value is measured by the direct current potential drop and then the perforation hole can be detected. Also, calorimetric impact detection is based on the fact that a substantial part of the particle's kinetic energy is converted into heat when impacting the target. The temperature of the target is measured by a contacted temperature sensor. However, their ways which are required to the attachment are not suitable for a large-scale structure and solar panels, because the detection area has been limited.

The surface inspection cameras operate by taking a series of digital images of a surface over a period of time and transmitting the images to Earth for analysis. By comparing the images, the impact sites can be detected. However, this is at the expense of an increase in the mass and power of the system and it takes time to detection.

4.9.2 Possiblity of Debris Sonser System Using Microwave Emission

Microwave emission has a potential to be a sensor. The possibility of debris impact detection using microwave is considered (K. Maki, 2004). Unlike the optical sensors, microwave emission can be easily detected even in sunny places. Also, microwave emission can be detected by discriminating the signal level automatically and quickly. By placing multiple antennas, impact site can be

detected using microwave (E. Soma, 2006; E. Soma, 2008). Although the detection using cross-correlation method was confirmed on the indoor experiments, they assumed that microwave is emitted spatially-uniform or homogeneously from the impact site. Yet, the disadvantage is that microwave emission is not yet well understood theoretically.

From my experimental results, it was clarified that microwave emits in the impact site with broad-band frequencies and the microwave emission intermittently radiates much longer than flash and plasma phenomena. By selecting the frequency bands of antennas, signal-to-noise ratio can be improved by avoiding noise level of external communication noise in service environment. Also, I found that microwave emission correlates with the hardness of the target. By my achievements, the possibility of debris sensors using microwave emission has been improved.

4.10 Summary

In Chapter 4, microwave emission phenomenon was investigated. By measuring the emission and plasma phenomena simultaneously, the microwave radiation phenomenon could be clarified. The experimental results have shown that the time scales between impact plasma (during dozens of microseconds) including light emission and microwave phenomena (during several milliseconds) are significantly different by simultaneous measurement.

In microwave measurement, it was possible to investigate the frequency characteristics of microwaves for the first time by measuring using two kinds of broadband LP antennas. Microwave signals radiate in a wide band, but I discovered that the effect of shielding the microwaves by the high-dense plasma of the impact plasma generated immediately after the impact. This suggests that the source of microwave signals is generated near the crater site inside the plume of impact plasma.

Furthermore, in order to investigate the microwave radiation mechanism, hypervelcity experiments focused on various kinds of aluminum materials were conducted. The experimental results showed that the harder the target is, the higher the intensity of microwave signals are. By using the numerical simulation, the target hardness has a correlation with the elastic wave repeatedly propagating in the target material, and it is considered that the intermittent radiation of the microwave is related to the propagation of the elastic wave.

From the above, it was concluded that microwave emission phenomenon could be clarified. The achievements can contribute to detect debris impact using microwave emissions.

Chapter 5

Conclusions

In my dissertation, I studied the electrical phenomena caused by hypervelocity impacts and their effects on spacecraft. The structure of each chapter is shown in Fig. 5.1. There are five chapters in my dissertation.

In Chapter 1, as the number of debris is huge, the collision between debris and spacecraft is inevitable and the situation is getting worse and worse. Although the mechanical phenomena (or damage) from hypervelocity impacts have been gained attention, the electrical phenomena (or damage) are also important to operate spacecraft safety even in the debris environment. I explained the importance of my research field there. In my dissertation, electrical phenomena, including impact plasma and microwave emissions, caused by hypervelocity impacts were investigated. In each chapter, I conducted the hypervelocity impact experiments to clarify the electrical phenomena and their effects on spacecraft by using the LGG.

In Chapter 2, the research to accurately estimate plasma density was done. The plasma density and propagation of impact plasma are important to estimate the risk of discharge to spacecraft. There are some plasma diagnosis methods, but plasma probe method can examine plasma parameters locally by placing multiple probes. Of three kinds of plasma probe methods, the double probe method was applied in my experiments. Also, the plasma temperature to calculate plasma density was estimated by using the spectroscopic method. In the conventional spectroscopic method, intensities at specific several wavelengths were measured and the temperature was derived under an assumption of the black-body radiation. However, it was clarified that the method cannot estimate the temperature when the line emission spectrum derived from projectile and target materials are included within the observed wavelengths. Therefore, I proposed the method to estimate temperature precisely by using the streak camera spectroscopy. The proposed method has some advantages: (1) temperature can be calculated with wider wavelength bands and higher sampling points and (2) the wavelengths of the profiled emission line spectrum are identified and the temperature can be precisely calculated by excluding intensities at the wavelengths.

In addition, the temporal change of emission line spectra was analyzed from impacts between different combinations of target and the projectile materials. By comparing the time change of emission line derived of projectile and target materials, it was clarified that the target and the projectile material both made a phase transition at the collision interface and a mixed gas derived from the target and the projectile material was generated. Thereby, it was achieved that the plasma density of impact plasma was able to be calculated precisely.

By accurately obtaining plasma parameters of impact plasma, it will be able to contribute to accurately estimate the impact on solar cells and power harnesses mounted on spacecraft.

In Chapter 3, electrical damage leading PSD may occur when hypervelocity impacts on the power harness. Using the double probe method based on Chapter 2, the relationship between impact plasma and discharge was investigated. Also, there was a deviation between the probability of actual accidents and collision frequency calculated by the debris simulation. There were two causes: absence of the internal circuit simulated to the satellite, and the effects of impact plasma due to multiple particle impacts. The effects of impact plasma was not unknown. Therefore, I clarified that the effects of PSD were investigated by re-examining the causes. Also, the relationship between impact plasma and discharge was investigated by using the double probe method.

It was found that impact plasma may trigger the primary discharge and even a single particle impact easily results in PSD occurrence in the conventional configuration without a load circuit. The surface of the power harness was melted and carbonized near impact sites. However, a single impact does not result in PSD occurrence in the configuration with a load circuit with a resistance and a capacitance. Also, PSD never occurred even when the impacts of multiple particles. Therefore, it was clarified that the load circuit heavily relies on the PSD occurrence by comparing the previous studies. Previous studies have yielded an important achievement that may have overestimated risk assessment.

In Chapter 4, the mechanism of microwave emission was still unveiled. By measuring the emission and plasma phenomena simultaneously, the microwave radiation phenomenon could be clarified. The experimental results have shown that the time scales between impact plasma (during dozens of microseconds) including light emission and microwave phenomena (during several milliseconds) are significantly different by simultaneous measurement.

In microwave measurement, it was possible to investigate the frequency characteristics of microwaves for the first time by measuring using two kinds of broadband LP antennas. Microwaves radiate in a wide band, but I discovered that the effect of shielding the microwaves by the high-dense plasma of the impact plasma generated immediately after the impact. This suggests that the source of microwave emissions is generated near the crater site inside the plume of impact plasma.

Furthermore, in order to investigate the microwave radiation mechanism, hypervelcity experiments focused on various kinds of aluminum materials were conducted. The experimental results showed that the harder the target, the higher the microwave radiation intensity. By using the numerical simulation, the target hardness has a correlation with the elastic wave repeatedly propagating in the target material, and it is considered that the intermittent radiation of the microwave is related to the propagation of the elastic wave.

In my conclusions, I investigated electrical phenomena of impact plasma and microwave emissions caused by hypervelocity impact. By accurately obtaining plasma parameters of impact plasma, it will be able to contribute to accurately estimate the impact on solar cells and power harnesses mounted on spacecraft. Based on my proposed method to obtain plasma parameters, I

also contributed to the reliability of the satellite power system due to debris impacts by re-examining hypervelocity experiments on power harnesses. The microwave emission phenomenon is expected to be applied to estimate the scale, position, and frequency of debris collisions in the future. It is concluded that I was able to contribute not only to basic knowledge but also to applied knowledge in the field of space engineering regarding electrical phenomena generated by hypervelocity impacts.

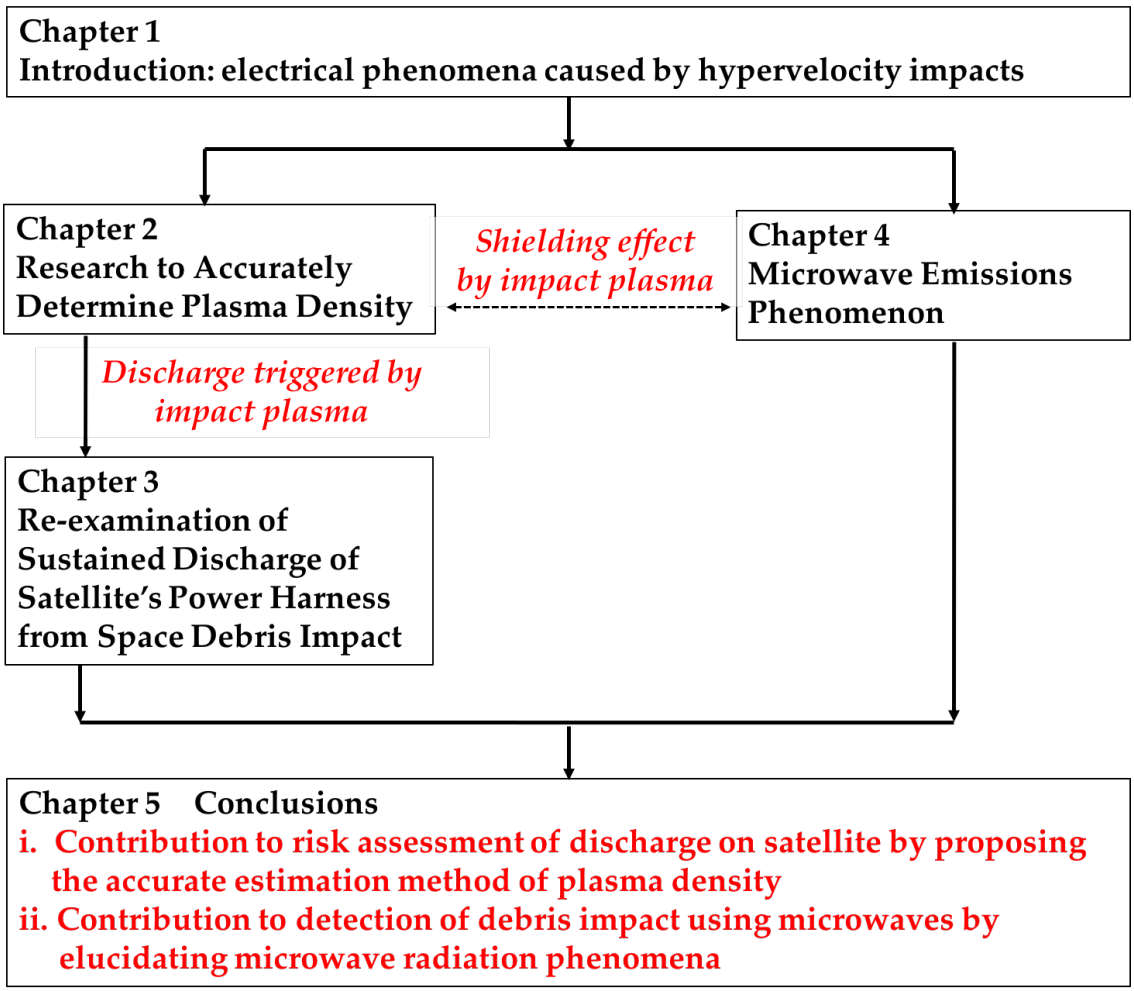

FIGURE 5.1: The overview of my dissertation

Appendix A

Specification of The Experimental Devices

In Appendix A, the specifications of the experimental devices is described in this experiments. Table A.2 and A.3 show specifications of experimental devices described in Chapter 2 and Chapter 3, respectivity. I measured phenomena of luminous vapor cloud and plasma in Chapter 2 and microwave emission phenomenon. Table A.1 shows specifications of experimental devices described in Chapter 4.

TABLE A.1: Specifications of main experimental devices in Chapter 4.

Experimental devices	**Company & Type**	**Specifications**
LNA (high frequency)	R&K LA150-0S	Gain: 45dB (typ.) Frequency range: 1500MHz - 6500MHz
LNA (low frequency)	R&K LA111-0S	Gain: 46dB (typ.) Frequency range: 9kHz-1000MHz
LP antenna (high frequency)		
LP antenna (low frequency)		
Network analyzer	Keysight N5222B	Frequency range: 10 MHz - 28.5 GHz
Oscilloscope	Tektronix MSO64	DC-8GHz, 25 GSa/s
Oscilloscope	Keysight DSOS254A	DC-2.5GHz, 400Mpts, 10GSa/s
RF cable	HUBER & SUHNER SUCOFLEX® 100	SMA-female
Signal analyzer	Agilent Technologies N9010A	Frequency range: 10 Hz - 26.5 GHz
Signal generator	Keysight PSG Analog Signal Generator E8257D	Frequency range: 250kHz-13GHz

TABLE A.2: Specifications of experimental devices in Chapter 2.

Experimental devices	Purpose	Company & Type	Specifications	Others
Data logger	Plasma	Yokogawa SL1000	isolated 8ch. 100MSa/s, 1Mohm	
Digital CCD camera	Luminous gas	Hamamatsu Photonics C10600-10B	1344(H) x 1024(V) pixels	
High speed video camera	Luminous gas	Shimadzu Hyper Vision HPV-X	128 frames, 400(H) x 250(V) pixels	
Photodetector	Luminous gas	Hamamatsu Photonics		
Plasma probe	Plasma	handmade		
Spectroscopy	Luminous gas	Hamamatsu Photonics C11119-02	focal length 300mm	
Streak camera	Luminous gas	Hamamatsu Photonics C7700-01S	wavelength:200 - 850nm, gain:15 - 45dB, grading: 150g/mm	

TABLE A.3: Specifications of experimental devices in Chapter 3.

Experimental devices	Purpose	Company & Type	Specifications	Others
Oscilliscope	Power harness	Teledyne LeCroy WaveSurfer 24MXs	DC-200MHz, 2.5GSa/s	
Oscilliscope	Plasma	Graphtec DM3300	DC-10MHz, 20MSa/s	
Power harness	Power harness	TE connectivity SPEC 55	single wall, AWG22	cross-linked ETFE polymer, silver plated copper conductor
Power supply (SAS1)	Power harness	Agilent Technologies E4362 solar array simulator	120V, 5A, 600W	
Power supply (SAS2)	Power harness	Agilent Technologies E4350B solar array simulator	80V, 6A, 480W	

Appendix B

Temperature Estimation Using The Conventional Method

In Appendix B, I explain the significance of my proposed method to estimate the temperature of luminous vapor cloud. To compare with the conventional method, the streak camera spectroscopy measurements were performed in two different wavelength regions from 342 nm to 650 nm, in addition to from 547 nm to 872 nm. The specification of the streak camera spectroscopy is the same as I described in Chapter 2. Here, in the past research, the intensities were calculated, when it was assumed that photodiodes with band pass filters of a bandwidth of 40 nm in three central wavelength of 500, 700, and 850 nm, because the same setup cannot be prepared.

When the aluminum projectile impacts on nylon projectile, the intensities transition at three wavelength bands of 500, 700, and 850 nm is shown in Fig. B.1. Assuming the blackbody radiation from the intensity ratio at 4 μs when the intensities are at the maximum, the fitting was performed. The fitting was performed in the same way with reference to past research that was fitting every 1000K. Figure B.2 shows the temperature estimation using the conventional method. The error bars on the horizontal axis indicate the bands of wavelength. The fitting was performed every 1000 K, but no temperature passing through three points was found. That is because intensities at 500 nm include the line emission originated by aluminum in addition to continous emission.

Therefore, it is difficult to find temperature passing through three points in the conventional method when the line emissions spectrum includes within the observed wavelength because the observed wavelngth is narrow bands and it is not able to identify the line emission spectrum originated target or projectile materials.

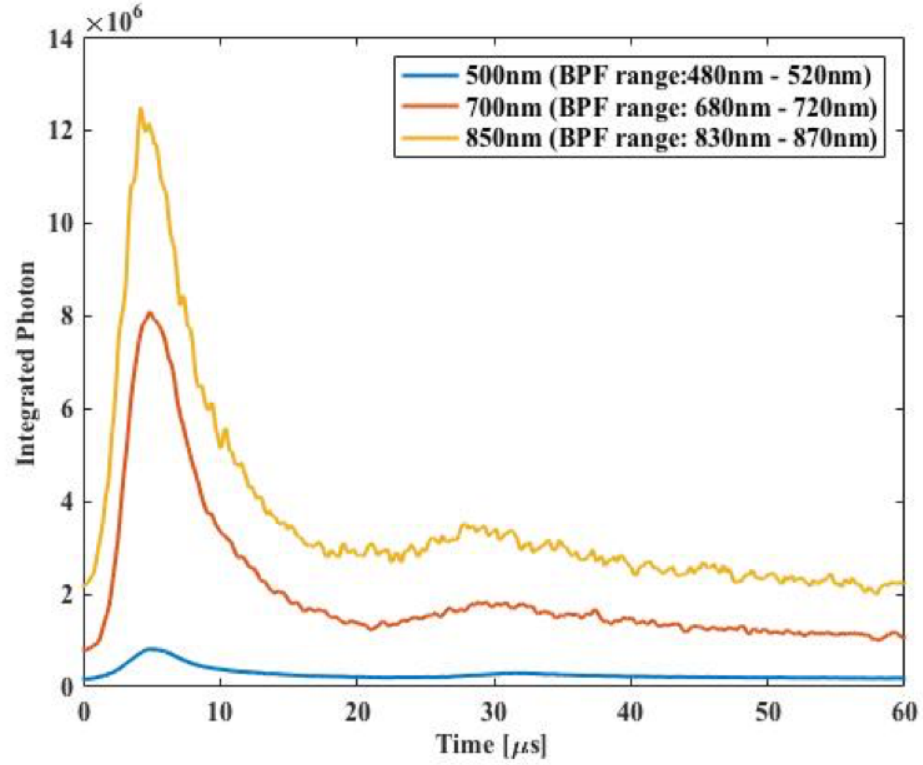

FIGURE B.1: The intensities transition at three wavelength bands of 500, 700, and 850 nm

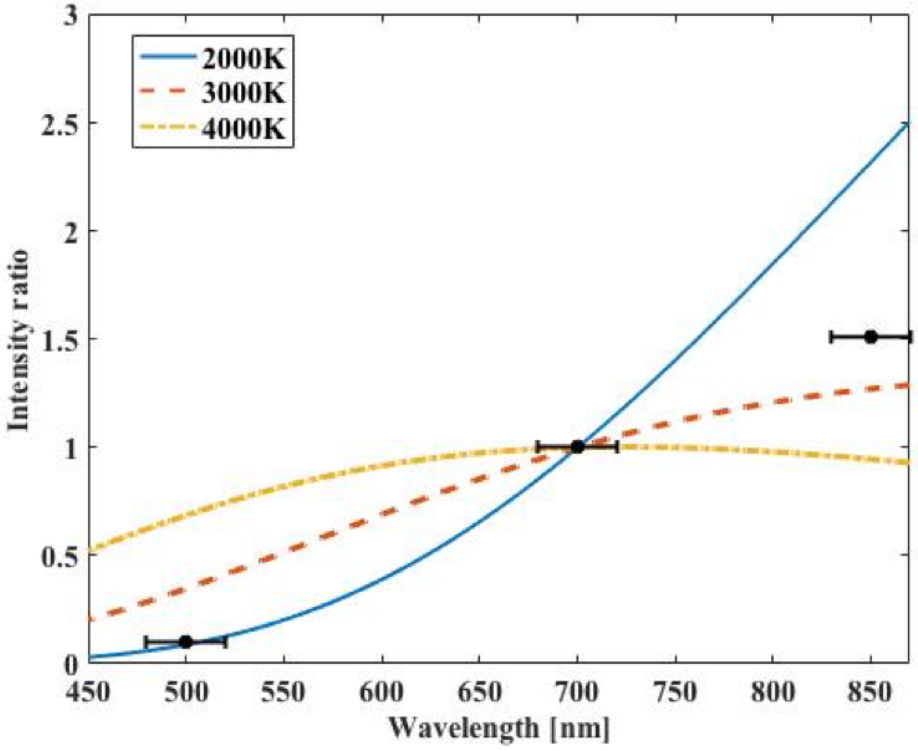

FIGURE B.2: The temperature estimation using the conventional method

Appendix C

Experiments for Antenna Pattern Measurements in An Anechoic Chamber

In Appendix B, the specifications of the experimental devices is described. It is also important to evaluate the characteristics of the antenna. Frequency bands of antennas are evaluated by S-parameters. S-parameters describe the input-output relationship between ports in an electrical sysytem (**AntennaTheory**). The numbering convention for S-parameters is that the first number following the 'S' is the port where the signal emerges, and the second number is the port where the signal is applied. Hence, when the numbers are the same such as S_{11}, it indicates a reflection measurement because the input and output ports are the same. The reflection coefficient S_{11} parameters of antennas are measured to evaluate the frequency bands of antennas. The S_{11} parameter of the log-periodic antenna are shown in Fig. C.1. Also, the antenna pattern is shown in C.4. Antenna patterns with three frequencies were measured because the log-periodic antenna has a wide frequency band. As the frequency band of the antenna increases, the antenna pattern tends to approach omnidirectionality. The maximum gain of patch antennas is typically 5 dBi.

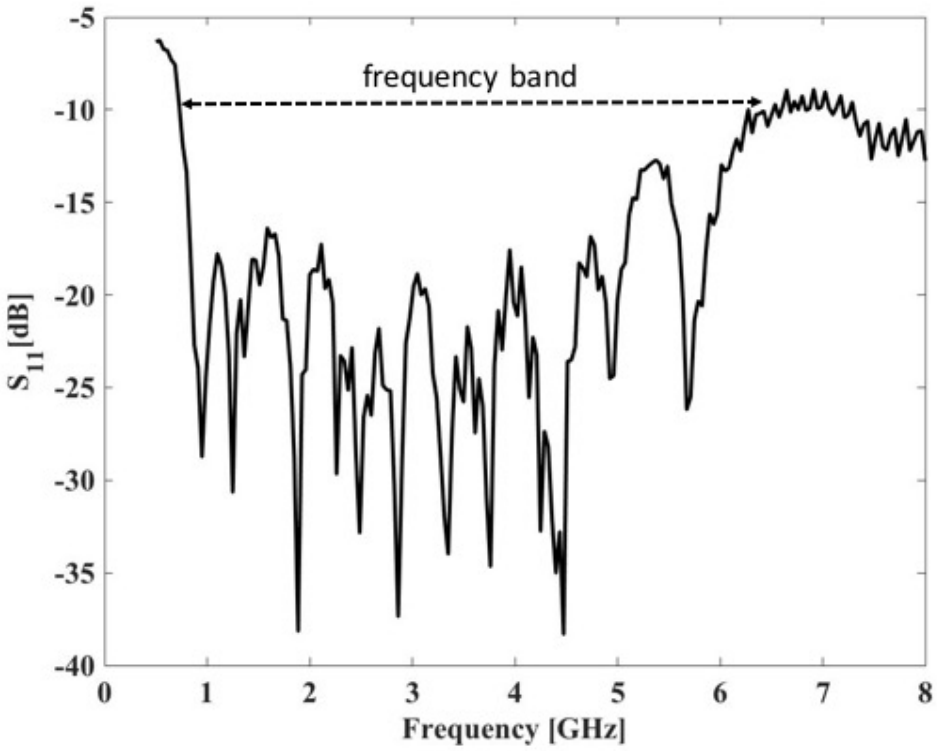

FIGURE C.1: S_{11} parameter of the log-periodic antenna

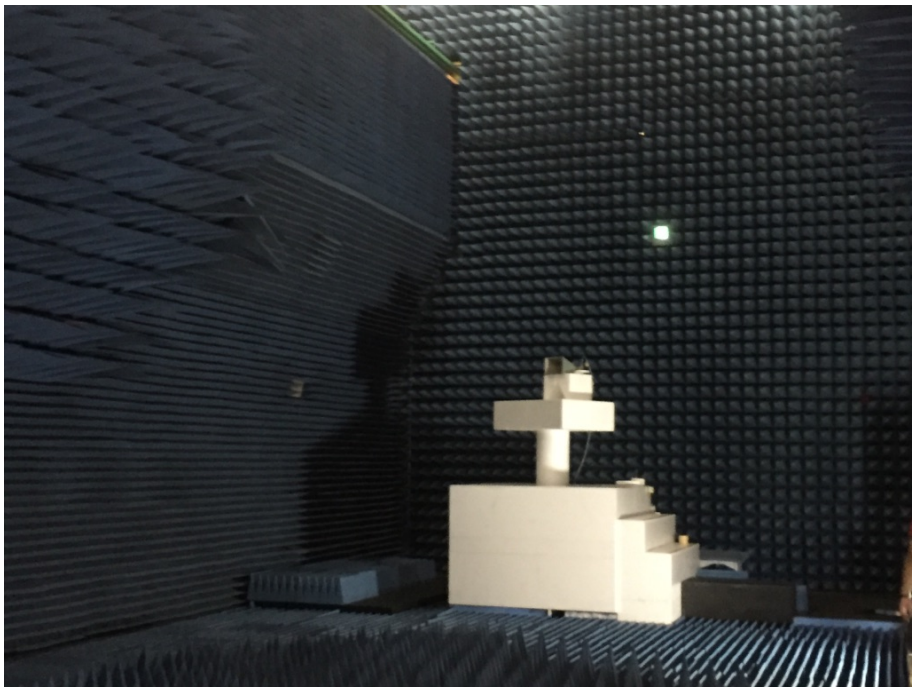

FIGURE C.2: The photograph of antenna pattern measurements in the anechoic chamber at ISAS/JAXA

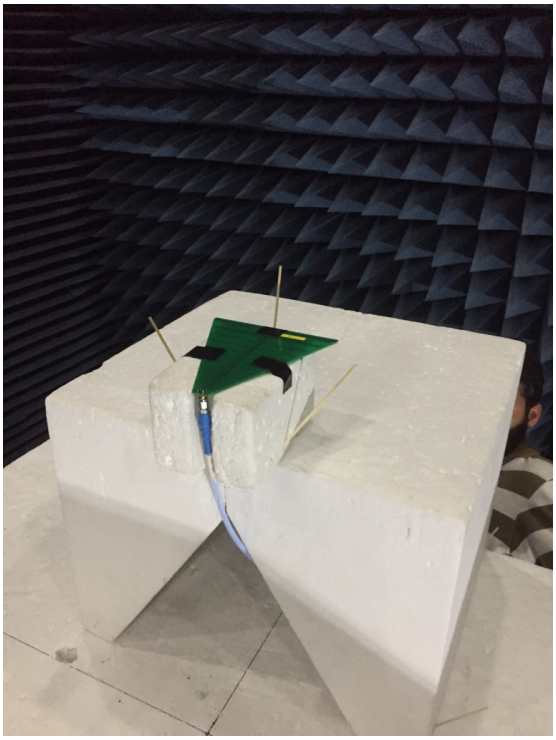

(A) A photo of antenna settting at E plane

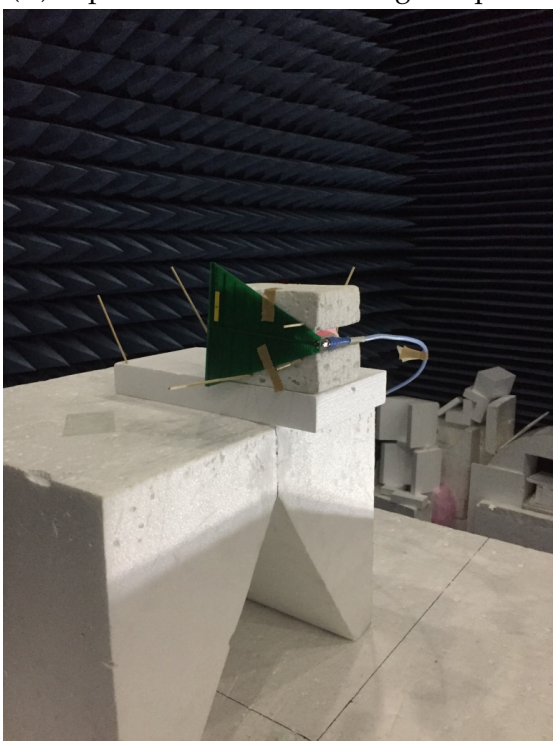

(B) A photo of antenna settting at H plane

FIGURE C.3: Setups for antenna pattern measurements

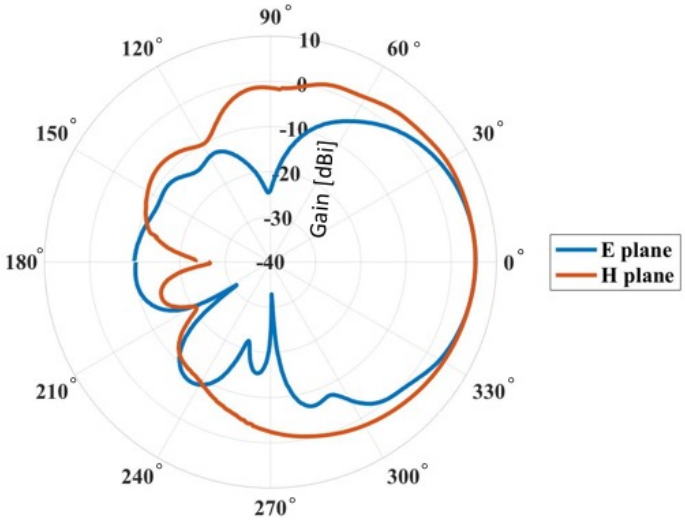

(A) Antenna pattern of the log-periodic antenna at 1500MHz

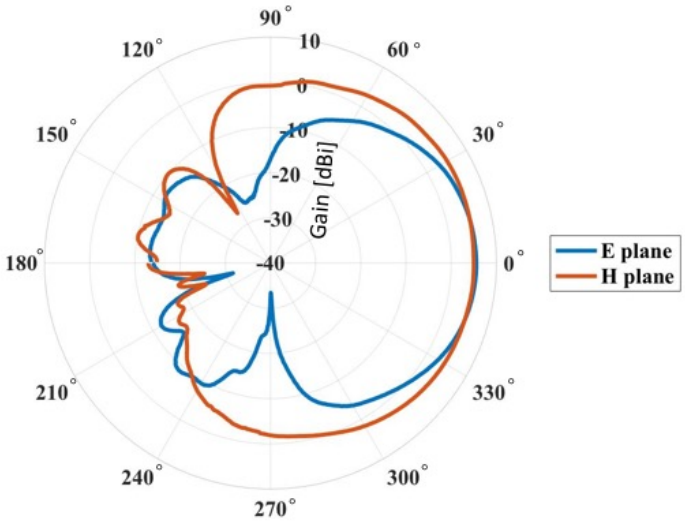

(B) Antenna pattern of the log-periodic antenna at 3000MHz

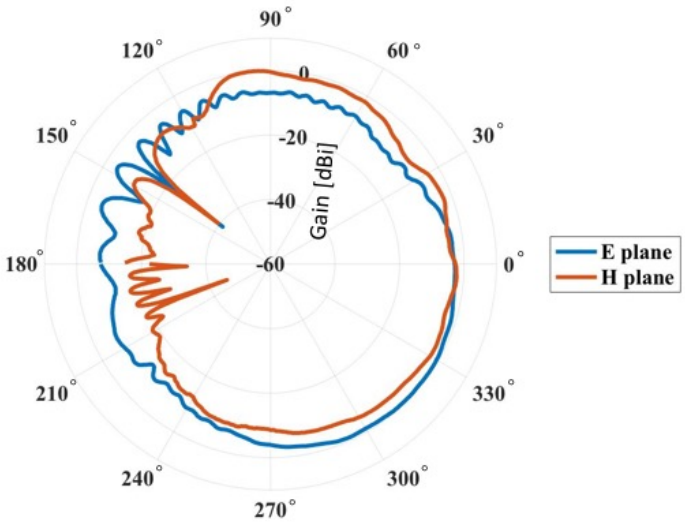

(C) Antenna pattern of the log-periodic antenna at 6000MHz

FIGURE C.4: Antenna Pattern of the receiver with the log-periodic antenna

Bibliography

A. Moussi G. Drolshagen, J.A.M. McDonnel J. C. Mandeville A. T. Kearsley H. Ludwig (2005). "Hypervelocity impacts on HST solar arrays and the debris and meteoroid population". In: *Advanced in Space Research* 35, pp. 1243 – 1253.

Akahoshi, Y. et al. (2008). "Influence of space debris impact on solar array under power generation". In: *International Journal of Impact Engeering* 35, pp. 1678–1682.

Bedingfield, K. L., R. D. Leach, and M. B. Alexander (1996). "Spacecraft System Failure and Anomalies Attributed to the Natural Space Environment". In: *NASA Reference Publication 1390*.

Bianchi, R. et al. (1984). "Radiofrequency emissions observed during macroscopic hypervelocity impact experiments". In: *Nature* 308, pp. 830–832.

Bonnal, C., J-M Ruault, and M-C Desjean (2013). "Active debris removal: Recent progress and current trends". In: *Acta Astronautica* 85, pp. 51–60.

Burchell, M. J. and N. G. Mackay (1998). "Crater ellipticity in hypervelocity impacts on metals". In: *Journal of Geophysical Research* 103, pp. 22,761–22,774.

Caswell, R.D., N. McBride, and A. Taylor (1995). "Olympus end of life anomaly - a Perseid meteoroid impact event?" In: *International Journal of Impact Engineering* 17, pp. 139 –150.

Committee, ASM International Handbook (2013). *ASM Handbook Heat Treating*. Vol. 4. ASM International, pp. –.

Cour-Palais, B. G. (1985). "Hypervelocity Impact Investigations and Meteoroid Shielding Experience Related to Apollo and Skylab". In: *NASA Conference Publication*, pp. 247–275.

D. A. Crawfield, P. H. Schultz (1991). "Laboratory Investigations of Impact-generated Plasma". In: *Journal of Geophysical Research* 96, pp. 18807 –18817.

D. J. Steinberg S. G. Cochran, M. W. Guinan (1980). "A Constitutive Model for Metals Applicable at High-Strain Rates". In: *Journal of Applied Physics* 51, pp. 1498 –1504.

David A. Crawford, Peter H. Schultz (1993). "The production and evolution of impact-generated magnetic fields". In: *International Journal of Impact Engineering* 14, pp. 205 –216.

— (1999). "Electromagnetic properties of impact-generated plasma, vapor and debris". In: *International Journal of Impact Engineering* 23, pp. 169 –180.

E. Soma K. Ishii, S. Chiba S. Hasegawa T. Takano M. Sano (2006). "Study on Position Determination of Space Debris Impact via Microwave". In: *International Symposium on Antennas and Propagation*, pp. 1–4.

E. Soma K. Maki, T. Takano M. Sano (2008). "Study on Impact Detection of Space Debris via Microwave". In: *The Japan Society for Aeronautical and Space Sciences (in Japanese)* 56, pp. 105–109.

E. Tang L. Zhao, M. Liu Y. Han (2018). "Research on discharge effect of solar array with power supply subjected to hypervelocity impact". In: *AIP Advances* 8, pp. 105206–1 –105206–10.

Eichhorn, G. (1976). "Analysis of the hypervelocity impact process from impact flash measurements". In: *Planetary and Space Science* 24, pp. 2434–2439.

Friichtenicht, J. F. (1962). "Two-million-volt electrostatic accelerator for hypervelocity research". In: *Review of Scientific Instruments* 33, pp. 209 –212.

Friichtenicht, J. F. and J. C. Slattery (1963). "Ionization Associated With Hypervelocity Impact". In: *NASA Technical Note* NASA TN D-2091, pp. 2434–2439.

Fukushige, S. et al. (2008). "Solar-Array Arcing Due to Plasma Created by Space-Debris Impact". In: *IEEE Transactions on Plasma Science* 36, pp. 2434–2439.

G. Martelli, P. Cerroni (1985). "On the theory of radio frequency emission from macroscopic hypervelocity impacts and rock fracturing". In: *Physics of the Earth and Planetary Interiors* 40, pp. 316 –319.

Glaser, P. E. (1968). "Power from the sun: its future". In: *Science* 162.

H. Dietzel G. Eichhorn, H. Fechtig E. Grun H.-J Hoffmann J. Kissel (1973). "The HEOS 2 and HELIOS Micrometeoroid Experiments". In: *Journal of Physics E. Scientific Instruments* 6, pp. 209 –217.

H. Iglseder, E. Igenbergs (1987). "Measured Charge Generation by Small Mass Impact at Velocities between 1 and 45 km/s". In: *International Journal of Impact Engineering* 5, pp. 381 –388.

H. Ohnishi S. Chiba, E. Soma K. Ishii K. Maki T. Takano S. Hasegawa (2007). "Study on microwave emission mechanisms on the basis of hypervelocity impact experiments on various target plates". In: *Journal of Applied Physics* 101, pp. 1 –8.

H. Ohnishi K. Maki, E. Soma K. Ishii S. Chiba T. Takano A. Yamori (2005). "Study on Microwave Emission Due to Hypervelocity Impact Destruction". In: *UNION RADIO-SCIENTIFIQUE INTERNATIONALE (URSI)* A01, pp. 1 –6.

Higashide, M. et al. (2009). "Ballistic limit of thin CFRP plates". In: *5th European Conference on Space Debris* 5, pp. 1–7.

Higashide, M. et al. (2010). "Debris Impact on CFRP-AL Honeycomb Sandwich Structure". In: *Trans. JSASS Aerospace Tech. Japan* 8, pp. 1–5.

— (2015). "Comparison of Aluminum Alloy and CFRP Bumpers for Space Debris Protection". In: *Procedia Engineering* 103, pp. 189–196.

IADC-08-03 (2007). *IADC Space Debris Mitigation Guidelines*. Tech. rep. Inter-Agency Space Debris Coordination Committee.

— (2013). *SENSOR SYSTEMS TO DETECT IMPACTS ON SPACECRAFT*. Tech. rep. Inter-Agency Space Debris Coordination Committee.

J. W. Cooley, J. W. Turkey (1965). "An Algorithm for the Machine Calculation of Complex Fourier Series". In: *Mathematics of Computation*, pp. 297 –301.

Japan, Aluminum Association (2001). *Aluminum Handbook 6th Edition*. Shoueisya Press, pp.15 –16.

Joel E. Willianmsen, Steven W. Evans (2015). "Orbital Debris Wire Harness Failure Assessment for the Joint Power Satellite System". In: *Procedia Engineering* 103, pp. 650 –656.

Johnson, E. O. and L. Malter (1950). "A Floating Double Probe Method for Measurements in Gas Discharges". In: *Phys. Rev.* 80, pp. 58–68.

K. Maki T. Takano, A. Fujiwara A. Yamori (2004). "Radio-wave emission due to hypervelocity impacts in relation to optical observation and projectile speed". In: *Advanced in Space Research* 34, pp. 1085–1089.

K. Maki E. Soma, T. Takano A. Fujiwara A. Yamori (2005). "Dependence of microwave emissions from hypervelocity impacts on the target material". In: *Journal of Applied Physics* 97, pp. 1 –6.

K. Zhang R. Long, Q. Zhang Y. Xue and Y. Ju (2016). "Flash characteristics of plasma induced by hypervelocity impact". In: *Physics of Plasmas* 23, pp. 14–1 –14–17.

Kadono, T. (1996). "Observation of Expanding Vapor Cloud Generated by Hypervelocity Impact". In: *Ph.D. dissertation at Kyoto University* 36, pp. 2434–2439.

Kawai, N. et al. (2010). "Single microparticle launching method using two-stage light-gas gun for simulating hypervelocity impacts of micrometeoroids and space debris". In: *Review of Scientific Instruments* 81.4, pp. 1–12.

Kawakita, S. et al. (2004). "Sustained Arc between Primary Power Cables of a Satellite". In: *2nd International Energy Conversion Engineering Conference* 7, pp. 1678–1682.

Kawakita, S. et al. (2009). "Discharge of Spacecraft Solar Panels by Hypervelocity Impact". In: *Trans. of JSASS Space Tech. Japan* 7, pp. 53–56.

Kawamoto, S. et al. (2018). "Performance of Electrodynamic Tether System for Debris Deorbiting: Re-evaluation Based on the Results of KITE Experiments". In: *Proceedings of 69th International Astronautical Congress* IAC-18-A6.6.5.4, pp. 1–12.

Kessler, D. J. and B. G. Cour-Palais (1978). "Collision frequency of artificial satellites: The creation of a debris belt". In: *Journal of Geophysical Research* 83.4, pp. 2637–2646.

Kessler, D. J., R. C. Reynolds, and P.D. Anz-Meador (1994). "Space Station Program Natural Environment Definition for Design, International Space Station Alpha". In: *NASA Space Station Program Office* 18.4, pp. 1–12.

Kim, J. et al. (2013). "Expansion of Tactical Utilities for Rapid ANalysis of Debris on Orbit Terrestrial". In: vol. 18. 4, pp. 290–300.

Ley, W., K. Wittmann, and W. Hallmann (2009). *Handbook of Space Technology*. Wiley, pp. 1–14.

Liou, J.-C. (2011). "An active debris removal parametric study for LEO environment remediation". In: *Advances in Space Research* 47.11, pp. 1–12.

Liou, J-Ch (2002). "The New NASA Orbital Debris Engineering Model ORDEM2000". In: *NASA/TP-2002-210780*.

M. S. Cowler N. K. Birnbaum, M. Itoh M. Katayama and H. Obata (1987). "AUTODYN - An interactive non-linear analysis program for microcomputers through supercomputers". In: *Proceedings of 9th International Conference on Structural Mechanics in Reactor Technology* B, pp. 401–406.

McKnight, Darren S. (2016). "Orbital debris hazard insights from spacecraft anomalies studies". In: *Acta Astronautica* 103, pp. 27–34.

Mechanical Engineers, The Japan Society of (2007). *JSME Computational Mechanics Handbook*. Asakura, pp. 443–460.

Mott-Smith, H. M. and Irving Langmuir (1926). "The Theory of Collectors in Gaseous Discharges". In: *Physical Review* 28, pp. –.

N. McBride, J. A. M. McDonell (1999). "Meteoroid impacts on spacecraft: sporadics, streams, and the 1999 Leonids". In: *Planetary and Space Science* 47, pp. 1005 –1013.

Nagaoka, Y. (2013). "Study on Electrical Phenomena from Hypervelocity Impact on Thin Film of Spacecraft". In: *Ph.D. dissertation at The Graduate University for Advanced Studies* 36, pp. 2434–2439.

Nagaoka, Y., K. Tanaka, and S. Sasaki (2012). "Propagation of Plasma Generated by Hyper-Velocity Impact on Thin Plate Structure". In: *The Japan Society for Aeronautical and Space Sciences* 60, pp. 89–95.

Nahra, Henry K. (1989). *Effect of Micrometeoroid and Space Debris Impacts on the Space Station Freedom Solar Array Surfaces*. Tech. rep. NASA Technical Memorandum.

NASA. *Historic Landsat 5 Mission Ends*. NASA. URL: https://landsat.gsfc.nasa.gov/historic-landsat-5-mission-ends/.

Nitta, K. et al. (2013). "Response of a Aluminum Honeycomb Subjected to Hypervelocity Impacts". In: *Procedia Engineering* 58, pp. 709–714.

Office, Orbital Debris Program (2008). *Orbital Debris Quarterly News*. Tech. rep. NASA.

— (2012). *Orbital Debris Quarterly News*. Tech. rep. NASA.

— (2015). *Orbital Debris Quarterly News*. Tech. rep. NASA.

— (2019). *Orbital Debris Quarterly News*. Tech. rep. NASA.

Oswald, M. (2005). "The MASTER 2005 Model". In: vol. 18. 4, pp. 1–12.

Paul, Clayton. R. (2006). *Introduction to Electromagnetic Compatibility*. A John Wiley and Sons.

Photonics, Hamamatsu. *Streak Camera Handbook*. Hamamatsu Photonics. URL: https://www.hamamatsu.com/resources/pdf/sys/SHSS0006E_STREAK.pdf.

Piekutowski, A. J. (1993). "CHARACTERISTCS OF DEBRIS CLOUDS PRODUCED BY HYPERVELOCITY IMPACTS OF ALUMINUM SPHERES WITH THIN ALUMINUM PLATES". In: *International Journal of Impact Engineering* 14, pp. 573–586.

— (1995). "FRAGMENTATION OF A SPHERE INITIATED BY HYPERVELOCITY IMPACT WITH A THIN SHEET". In: *International Journal of Impact Engineering* 17, pp. 627–638.

R. Putzar F. Schaefer, M. Lambert (2008). "Vulnerability of spacecraft harnesses to hypervelocity impacts". In: *International Journal of Impact Engineering* 35, pp. 1728 –1734.

Requirement, Engineering (2014). *Space debris protection guideline*. JERG-2-144-HB001, pp. –.

S. Chen, T. Sekiguchi (1965). "Instantaneous Direct-Display System of Plasma Parameters by Means of Triple Probe". In: *Journal of Applied Physics* 36, pp. 2363 –2375.

S. Close P. Colestock, L. Cox M. Kelley N. Lee (2010). "Electromagnetic pulses generated by meteoroid impacts on spacecraft". In: *Journal of Geophysical Research* 115, pp. 1–7.

S. Close I. Linscott, N. Lee T. Johnson D. Strauss A. Goel A. Fletcher D. Lauben R. Srama A. Mocker S. Bugiel (2013). "Detection of electromagnetic pulses produced by hypervelocity micro particle impact plasmas". In: *Physics of Plasmas* 20, pp. 092102–1–092102–8.

S. Fukushige Y. Akahoshi, T. Koura S. Harada (2006). "Development of perforation hole detection system for space debris impact". In: *International Journal of Impact Engineering* 33, pp. 273–284.

S. Hosoda J. Kim, M. Cho K. Toyoda S. Kawakita M. Kusawake M. Takahashi H. Maejima (2006). "Ground Investigation of Sustained Arc Phenomena in Power Cables on ADEOS-II Satellite". In: *Transactions of the Japan Society for Aeronautical and Space Sciences (in Japanese)* 54, pp. 427 –433.

S. Sasaki K. Tanaka, K. Maki (2013a). "Maintenance Scenario for Solar Power Satellite to Prevent Space Junk". In: *Proceedings of the 64th International Astronautical Congress* C3.1.5, pp. 1–5.

— (2013b). "Microwave Power Transmission Technologies for Solar Power Satelites". In: *Proceedings of The IEEE* 101.6, pp. 1438–1447.

S. Sugita, P. H. Schultz and S. Hasegawa (2003). "Intensities of atomic lines and molecular bands observed in impact-induced luminescence". In: *Journal of Geophysical Research* 108, pp. 14–1 –14–17.

S. Tagami M. R. Quesada, T. Koura Y. Akahoshi (2017). "Discharge On Solar Array Coupon By Debris Impact". In: *Procedia Engineering* 204, pp. 323 – 328.

Science Technology Policy, Office of (1995). *Interagency Report on Orbital Debris*. Tech. rep. Executive Office of the President of the United States, pp. 3–10.

Sibeaud, J.-M, L. Thamie, and C. Puillet (2008). "Hypervelocity impact on honeycomb target structures: Experiments and modeling". In: *Procedia Engineering* 35, pp. 1799–1807.

Standard Technology (NIST), National Institution of. *National Institution of Standard Technology (NIST)*. National Institution of Standard Technology (NIST). URL: https://physics.nist.gov/PhysRefData/ASD/lines_form.html.

Steven G. O'Keefe, David V. Thiel (1995). "A mechanism for the production of electromagnetic radiation during fracture of brittle materials". In: *Physics of the Earth and Planetary Interiors* 89, pp. 127 –135.

Stevens, N. J. (1986). "Summary of PIX-2 Flight Results over the First Orbit". In: *AIAA Aerospace Sciences Meeting* 4.

Takano, T. et al. (2002). "Microwave emission due to hypervelocity impacts and its correlation with mechanical destruction". In: *Journal of Applied Physics* 92, pp. 830–832.

Thomas W. Kerslake, Eric D. Gustafson (2003). "On-Orbit Performance Degradation of the International Space Station P6 Photovoltaic Arrays". In: *American Institute of Aeronautics and Astronautics* AIAA-2003-5999, pp. 1 –6.

Tonks, Lewi and Irving Langmuir (1929). "Oscillation in Ionized Gases". In: *Physical Review* 33, pp. 195 –211.

Tribble, Alan C. (2003). *The Space Environment Implications for Spacecraft Design Revised and Expanded Edition*. Princeton University Press, pp.115 –152.

Whipple, Fred L. (1947). "Meteorites and Space Travel". In: *The Astronomical Journal* 1161, p. 131.

Achievement Lists

Publications

[1] **Y. Mando**, K. Tanaka, T. Hirai, S. Kawakita, M. Higashide, H. Kurosaki, S. Hasegawa, and K. Nitta, "Investigation on Sustained Discharge of Satellite's Power Harness Due to Plasma from Space Debris Impact," The American Society of Mechanical Engineers. (in press)

[2] **万戸 雄輝**, 塩田 一路, 田中 孝治, 長谷川 直, "超高速衝突によるイジェクタの時間分解発光スペクトルの解析," 日本航空宇宙学会誌. (査読中)

[3] T. Hirai, M. Higashide, H. Kurosaki, S. Hasegawa, **Y. Mando**, S. Yamaguchi and K. Tanaka, "Re-Examination of Electrical Failure Risk on Satellite's Power Harness Caused by Space Debris Impacts: Simultaneous Measurements of Sustained Discharge and Plasma Density," Procedia Engineering, Vol. 204, pp. 45-51, 2017.

[4] **Y. Mando**, I. Shiota, E. Soma, T. Yamagami, T. Nakamura, N. Sekiya, T. Ohta, S. Hasegawa, and K. Tanaka, "Wide-band Measurements of Microwave Emissions from Hypervelocity Impact on Aluminum Plates," IEEE Transactions on Plasma Science. (in preparation)

Awards

[1] **Y. Mando**, and K. Tanaka, "Outstanding Paper Award of IEEE Asia-Pacific Conference on Plasma and Terahertz Science", August 2018.

[2] **Y. Mando**, and K. Tanaka, "Best Young Research Form Award of International Conference on Applied Physics", October 2018.

International Conferences

[1] **Y. Mando**, "Review of Electrical Phenomena Caused by Hypervelocity Impacts of Space Debris", International Workshop on Solar Power Satellite, Kanagawa, Japan, November 2019.

[2] **Y. Mando**, K. Tanaka, T. Hirai, S. Kawakita, M. Higashide, H. Kurosaki, S. Hasegawa, and K. Nitta, "Investigation on Sustained Discharge of Satellite's Power Harness Due to Plasma from Space Debris Impact," Hypervelocity Impact Symposium, Florida, U.S, March 2019.

[3] **Y. Mando**, and K. Tanaka, "Basic Study on Plasma Generation Excited by Hypervelocity Impact of Space Debris," International Conference on Applied Physics, Chiba, Japan, October 2018.

[4] **Y. Mando**, K. Tanaka, E. Soma, I. Shiota, T. Yamagami, S. Haseba, S. Katano, and M. Yoneyama, "Characteristics of Microwave Emissions from Hypervelocity Impacts on Pure Aluminum and Various Aluminum Alloy Plates," The 69th International Astronautical Congress, Bremen, Germany, October 2018.

[5] **Y. Mando**, and K. Tanaka, "Study on Propagation of Plasma Induced by Hypervelocity Impact on Aluminum Plates," IEEE Asia-Pacific Conference on Plasma and Terahertz Science, Xi'an, China, August 2018.

[6] **Y. Mando**, R. Sakamoto, E. Soma, I. Shiota, T. Hirai, H. Kurita, M. Kawada, and K. Tanaka, "Microwave Emission from Hypervelocity Impacts Using Aluminum and Nylon for Target and Projectile Materials", 68th International Astronautical Congress, Adelaide, Australia, 2017.

[7] **Y. Mando**, R. Sakamoto, E. Soma, I. Shiota, T. Hirai, H. Kurita, M. Kawada, and K. Tanaka, "Measuring 5.8GHz-band Microwave Emission from Hypervelocity Impacts of Different Combinations of Projectile and Target Materials", 31st International Space and Technology Science, Ehime, Japan, 2017.

[8] T. Hirai, M. Higashide, H. Kurosaki, S. Hasegawa, **Y. Mando**, S. Yamaguchi and K. Tanaka, "Re-Examination of Electrical Failure Risk on Satellite's Power Harness Caused by Space Debris Impacts: Simultaneous Measurements of Sustained Discharge and Plasma Density," Hypervelocity Impact Symposium, Canterbury, U.K, March 2017.

[9] T. Hirai, M. Higashide, H. Kurosaki, S. Kawakita, S. Hasegawa, **Y. Mando**, S. Yamaguchi, and K. Tanaka, "Possibility of sustained discharge on satellite's power harness behind the solar array paddle caused by hypervelocity impacts," 31st International Space and Technology Science, Ehime, Japan, 2017.

[10] T. Hirai, M. Higashide, H. Kurosaki, S. Kawakita, **Y. Mando**, S. Yamaguchi, and K. Tanaka, "Electrical failure on satellite's power harness caused by hypervelocity impacts," The 31st International Congress on High-speed Imaging and Photonics, Osaka, Japan, 2016.

Domestic Conferences

[1] **万戸 雄輝**, 相馬 央令子, 塩田 一路, 山神 達也, 中村 剛也, 関谷 直樹, 太田 大智, 阿久津 壮希, 長谷川 直, 田中 孝治, “異種材料の超高速衝突における発光温度計測,” 2019 年度宇宙科学に関する室内実験シンポジウム, 相模原市, 神奈川県, 2020 年 3 月 (書面発表).

[2] **万戸 雄輝**, 相馬 央令子, 山神 達也, 長谷波 秀一, 田中 孝治, “スペースデブリ衝突により生成されるイジェクタの伝搬に関する研究,”第 38 回宇宙エネルギーシンポジウム,相模原市, 神奈川県, 2019 年 3 月.

[3] **万戸 雄輝**, 相馬 央令子, 塩田 一路, 山神 達也, 長谷波 秀一, 田中 孝治, “超高速衝突により生じるイジェクタの分光計測,”平成 30 年度宇宙科学に関する室内実験シンポジウム,相模原市, 神奈川県, 2019 年 2 月.

[4] **Y. Mando**, E. Soma, I. Shiota, S. Haseba, T. Yamagami, N. Sekiya, T. Nakamura, T. Ota, and K. Tanaka, “Simultaneous Measurement of Electrical Phenomena Induced by Space Debris Impact,” The 8th Space Debris Workshop, Chofu, Tokyo, December 2018.

[5] **万戸 雄輝**, 田中 孝治, 山神 達也, 長谷波 秀一, 相馬 央令子, 塩田 一路, “アルミニウム板への超高速衝突により生じるマイクロ波に関する基礎研究,” 平成 29 年度衝撃波シンポジウム, 仙台, 宮城, 2018 年 2 月.

[6] **Y. Mando**, K. Tanaka, I. Shiota, E. Soma, T. Yamagami, S. Haseba, and T. Hirai, “Preliminary Study on Microwave Emission from Space Debris Impacts,” 2018 Symposium on Laboratory Experiment for Space Science, Sagamihara, Kanagawa, February 2018.

[7] **Y. Mando**, S. Sakamoto, E. Soma, I. Shiota, T. Hirai, H. Kurita, K. Tanaka, and M. Kawada, “Polarization Analysis of Microwave Generated by Hypervelocity Impacts”, 2017 Symposium on Laboratory Experiment for Space Science, Sagamihara, Kanagawa, February 2017.

[8] **万戸 雄輝**, 相馬 央令子, 塩田 一路, 平井 隆之, 栗田 大樹, 田中 孝治, “超高速衝突時の標的厚さにより生じる電気的現象の研究,” 第 61 回宇宙科学技術連合講演会, 新潟, 2017 年

[9] **Y. Mando**, S. Koyama, S. Yamaguchi, K. Tanaka, and M. Kawada, “Preliminary Experiments on Interactions between Microwave and Plasma,” 2016 Symposium on Laboratory Experiment for Space Science, Sagamihara, Kanagawa, February 2016.

[10] 東出 真澄, 平井 隆之, 川北 史郎, 仁田 工美, 黒崎 裕之, 長谷川 直, **万戸 雄輝**,

田中 孝治, “微小粒子衝突による衛星電力ハーネス短絡故障リスクの実験的評価,” 第62回宇宙科学技術連合講演会, 福岡, 2018年.

[11] 平井 隆之, 川北 史郎, **万戸 雄輝**, 東出 真澄, 黒崎 裕之, 仁田 工美, 長谷川 直, 田中 孝治, “微小粒子衝突による衛星電力ハーネスの恒久的持続放電リスク,” 平成29年度 宇宙科学に関する室内実験シンポジウム, 相模原, 2018年.

[12] 平井 隆之, 東出 真澄, 黒崎 裕之, 川北 史郎, 長谷川 直, **万戸 雄輝**, 山口 翔太, 田中 孝治, “微小デブリ衝突による衛星電力ハーネスの電気的損傷リスク,” 平成 28 年度 宇宙科学に関する室内実験シンポジウム, 相模原, 2017年.

[13] 坂本 凌平, **万戸 雄輝**, 田中 孝治, “プローブ法によるパルス状プラズマ温度・密度計測のための較正実験,” 平成28年度 宇宙科学に関する室内実験シンポジウム, 相模原, 2017年.

[14] 平井 隆之, 東出 真澄, 黒崎 裕之, 川北 史郎, **万戸 雄輝**, 山口 翔太, 田中 孝治, “微小デブリ衝突による電力ハーネスの電気的損傷 : 太陽電池パドル裏側の単線ハーネス,” 第13回宇宙環境シンポジウム, 東京, 2016年11月

[15] T. Hirai, M. Higashide, H. Kurosaki, S. Kawakita, **Y. Mando**, S. Yamaguchi, and K. Tanaka, “Electrical failure on satellite’s power harnesses due to small debris impacts,” The 7th Space Debris Workshop, Chofu, Tokyo, October 2016.

[16] 平井 隆之, 東出 真澄, 黒崎 裕之, 川北 史郎, **万戸 雄輝**, 山口 翔太, 田中 孝治, “微小デブリ衝突による電気的損傷の研究 : 放電計測とダブルプローブ法によるプラズマ計測,” 平成27年度 宇宙科学に関する室内実験シンポジウム, 相模原, 2016年.

[17] 長谷波 秀一, 田中 孝治, 黒田 圭司, **万戸 雄輝**, “大電力マイクロ波照射時のプラズマ測定実験,” 第62回宇宙科学技術連合講演会, 福岡, 2018年

[18] 長谷波 秀一, 田中 孝治, 黒田 圭司, **万戸 雄輝**, “電離層プラズマ計測のための高速掃引シングルプローブ法とトリプルプローブ法の比較,” 平成 29 年度 宇宙科学に関する室内実験シンポジウム, 相模原, 2018年.

[19] **万戸 雄輝**, 山神 達也, 長谷波 秀一, 片野 将太郎, 中村 剛也, 関谷 直樹, ラザ ムダシール, 太田 大智, 相馬 央令子, 牧 謙一郎, 田中 孝治, “宇宙太陽光発電に関する宇宙教育活動,” 平成30年度 宇宙教育シンポジウム, 相模原, 2019年.